

Flexible and Privacy Conserving Optimal Parameter Tuning for Large Scale Power Systems

Dissertation

zur Erlangung des akademischen Grades
Doktoringenieur (Dr.-Ing.)

von

Amer Mešanović

geboren am 24. November 1991 in Kakanj

genehmigt durch die Fakultät für Elektrotechnik und Informationstechnik der
Otto-von-Guericke-Universität Magdeburg

Gutachter:

Prof. Dr.-Ing. Rolf Findeisen

Prof. Dr. Ian Hiskens

Dr. Ulrich Münz

eingereicht am 6. November 2019

Promotionskolloquium am 23. Oktober 2020

“An expert is a person who has made all the mistakes that can be made in a very narrow field.”

Niels Bohr,
(1885 - 1962)

Contents

List of symbols and abbreviations	IX
Abstract	XI
Deutsche Kurzfassung	XIII
1 Introduction and motivation	1
1.1 Contributions	7
1.2 Related works	8
1.3 Outline	9
2 The controller synthesis problem	12
2.1 Control oriented power system modeling	12
2.1.1 Power grid	13
2.1.2 Dynamic prosumers and tunable parameters	14
2.1.3 Overall model	17
2.2 Performance outputs	18
2.3 \mathcal{H}_∞ parameter optimization	19
2.4 Overall problem setup	19
2.5 Problem complexity	20
2.6 Summary	21
3 Structured controller tuning with stability guarantees	22
3.1 Structured controller synthesis based on the Bounded real Lemma	22
3.2 Controller tuning with frequency sampling	25
3.2.1 Semi-infinite \mathcal{H}_∞ controller tuning problem	26
3.2.2 Finite \mathcal{H}_∞ controller tuning problem	30
3.2.3 Solution algorithm	33
3.3 Frequency weighting in the optimization problem	34
3.4 Summary	35
4 Numerical evaluation	36
4.1 IEEE 39 bus system	36
4.2 AC/DC integration	38
4.3 European 53 power plant system	40

4.4	Summary	43
5	Experimental validation	45
5.1	Initial parameterization	46
5.2	Manual tuning	48
5.3	Automatic tuning	49
5.3.1	Parameter tuning for inverters 1 and 6	50
5.3.2	Parameter tuning for all inverters	51
5.4	Summary	51
6	Performance comparison	54
6.1	Synthesis methods for distributed controllers	54
6.1.1	Sparsity-promoting \mathcal{H}_2 controller synthesis (SPH2)	55
6.1.2	Sparsity-promoting \mathcal{H}_∞ controller synthesis (SPHinf)	56
6.1.3	Simulation comparison	59
6.2	Computational complexity of structured \mathcal{H}_∞ synthesis methods	68
6.2.1	Path-following (homotopy) method	68
6.2.2	Linearized convex-concave decomposition	69
6.2.3	Non-smooth optimization	70
6.2.4	Projection onto the cone of positive definite matrices	70
6.2.5	Comparison of computation times	71
6.3	Summary	73
7	Multi-scenario structured controller synthesis	75
7.1	Modeling of contingencies	76
7.1.1	Modeling dynamic prosumer dropouts	76
7.1.2	Modeling branch dropouts	77
7.1.3	Modeling of dropouts of several components	78
7.2	Multi-scenario structured \mathcal{H}_∞ synthesis	79
7.2.1	Extension of the Bounded real lemma method	79
7.2.2	Extension of the frequency-sampling method	80
7.3	Improvement of the dynamic security for the IEEE 39 bus power system	81
7.4	Summary	83
8	Scalable and Data Privacy Conserving Controller Tuning for Large-Scale Networks	84
8.1	Controller tuning problem for large power systems	85
8.1.1	Outline of the proposed hierarchical controller tuning approach	85
8.1.2	Modeling of the subsystems	86
8.1.3	Coupled power system model	89
8.2	Hierarchical parameter tuning	90
8.2.1	Structured \mathcal{H}_∞ parameter tuning of the reduced system	91

8.2.2	Model matching step	91
8.2.3	Model reduction step	92
8.2.4	Condition for the improvement of the system \mathcal{H}_∞ norm	93
8.2.5	Evaluation of the improvement of the system \mathcal{H}_∞ norm	94
8.2.6	Detailed algorithm for the proposed approach	95
8.3	Application to the IEEE 68 bus example	96
8.3.1	Centralized tuning and the impact of renewables	97
8.3.2	Hierarchical data privacy conserving \mathcal{H}_∞ parameter tuning	100
8.3.3	Structured model reduction	100
8.3.4	Structured \mathcal{H}_∞ optimization for the overall reduced system	102
8.3.5	Model matching	103
8.3.6	Results of hierarchical \mathcal{H}_∞ controller tuning	104
8.4	Tuning for an artificial large scale power system	105
8.5	Summary	108
9	Conclusions and outlook	110
9.1	Outlook	111
A	Oscillation damping in linear systems	113
A.1	Modal analysis of linear systems	113
A.2	Relation between the \mathcal{H}_∞ norm and oscillation damping	114
B	Modeling of coupled AC-DC power systems	117
B.1	DC power grid model	117
B.2	AC-DC converter models	117
B.3	Coupled AC-DC power system model	119
C	Power system models	120
C.1	IEEE 39 bus power system	120
C.2	Extended IEEE 39 bus AC/DC power system	120
C.3	Reduced European power system with 53 power plants	122
C.4	IEEE 68 bus power system	122
C.5	Four power plant system from [51]	122
	Bibliography	125

List of symbols and abbreviations

AC	alternating current
DC	direct current
HVDC	high-voltage direct current
LMI	linear matrix inequality
LTI	linear time-invariant
MIMO	multi-input multi-output
POD	power oscillation damping
PSS	power system stabilizer
SO	subsystem operator
SC	system coordinator
$\ G(s)\ _\infty$	\mathcal{H}_∞ norm of $G(s)$
\mathcal{P}_i	i -th dynamic prosumer, i.e. a producer or consumer of electric power
\mathcal{S}_i	i -th subsystem
$\bar{\sigma}(M)$	largest singular value of matrix M
$\bar{\lambda}(M)$	largest eigenvalue of matrix M
$(M)^*$	conjugate transpose of matrix M
$\succ (\succeq)$	positive (semi)definiteness of a matrix
$\prec (\preceq)$	negative (semi)definiteness of a matrix
j	imaginary unit
$\mathbb{R}_{\geq 0}$	set of non-negative real numbers
\mathbb{C}	set of complex numbers
$\mathbb{C}_{>0}$	set of complex numbers with a positive real part
$j\mathbb{R}_{\geq 0}$	set of complex numbers s with $\text{Re}(s) = 0$ and $\text{Im}(s) \in \mathbb{R}_{\geq 0}$
\mathcal{RH}_∞	set of proper, real rational and stable transfer matrices

Vectors are denoted with boldface symbols. We use the notation $\text{vec}_i(\mathbf{x}_i)$ to denote the vector obtained by stacking the vectors \mathbf{x}_i for all i , where the set of i is previously defined or is clear from the context, and $\text{bd}_i(A_i)$ to construct a block-diagonal matrix consisting of matrices A_i , for all i , where the set of i is previously defined or is clear from context. The operators $< (\leq)$, $> (\geq)$ and $|\cdot|$ are defined element-wise for vectors.

Abstract

Reliable and secure operation of power systems becomes increasingly challenging as the share of volatile generation rises, leading to largely changing dynamics of the system. Typically, the architecture and structure of controllers in power systems, such as voltage controllers of power generators, are fixed during the design and buildup of the network. Replacing existing controllers is often undesired, challenging, or not possible at all. Setpoint adjustments, as well as tuning of the controller parameters, are possibilities to counteract large disturbances and changing dynamics which do not require changing the existing controllers. We consider approaches for fast, computationally efficient, and privacy conserving adaptation of parameters of structured controllers for large scale power systems based on \mathcal{H}_∞ optimization, also referred to as structured \mathcal{H}_∞ controller synthesis. The approach allows the dependency of the system model on the controller parameters to be nonlinear.

Two methods for structured \mathcal{H}_∞ controller synthesis are proposed, and conditions are established that guarantee that the approaches leads to stability of the closed loop system. The results are verified experimentally in a field test microgrid consisting of six inverters and a load bank, as well as multiple simulation studies. The proposed methods improve the system robustness, as well as the time-response to step disturbances and allow structured controller tuning even for large power networks. The results are compared to other methods for structured \mathcal{H}_∞ synthesis, focusing on computation time and the obtained \mathcal{H}_∞ norm, underlining the efficiency of the introduced methods. In addition, comparisons with approaches which introduce wide-area controllers to the system are made. It is shown that the proposed approach achieves an improved time-domain response, compared to existing wide-area control approaches.

Finally, we introduce a hierarchical approach for the controller tuning, which exploits model reduction. The approach increases data privacy and scalability of the tuning, compared to centralized methods. Thereby, we derive conditions for the success of the approach and introduce a tailored approach for distributed model reduction of power systems. We apply the proposed hierarchical tuning method on the IEEE 68 bus system to show its effectiveness. We show that a similar system performance can be obtained as with a centralized method. The scalability of the approach is underlined considering a large scale power system with more than 2500 states and 1500 controller parameters.

The approaches set the base for a series of future developments and can be expanded to other classes of systems, such as transport systems, water systems etc.

Deutsche Kurzfassung (German Abstract)

Einführung

Zuverlässige und sichere Stromversorgung ist unerlässlich für das moderne Leben. Stromsysteme müssen ohne Unterbrechungen, trotz unbekannter Störungen, Ausfällen, unbekannter Lastdynamiken, und Änderungen in der Stromerzeugung, operieren. Stromsysteme bestehen aus zahlreichen Komponenten, von Erzeugern und Lasten, wie Kraftwerke, Windturbinen und Verbrauchern, bis hin zu Energiewandlern und Speichern, die durch das Stromnetz verbunden sind, c.f. Abb. 1.

Der sichere Betrieb heutiger Stromnetze wird durch ein komplettes Automatisierungssystem, bestehend aus, z.B., PID Reglern und Bandstoppfiltern, "garantiert", dass das Gesamtsystem regelt und koordiniert. Diese Automatisierungssysteme entstanden durch Jahrzehnte lange praktische Erfahrung, Beobachtung und Betrieb.

Die Parametrierung der involvierten Regler ist für den zuverlässigen Betrieb unabdingbar. Heutzutage wird die Parametrierung der Regler während der Inbetriebnahme größerer Komponenten in einem zeitaufwändigen, mehrstufigen Prozess durchgeführt. Die resultierenden Regler werden typischerweise über Jahrzehnte nicht mehr umparametriert, außer es treten große Probleme im System auf. Diese manuelle Parametrierung zeigte sich als ausreichend solange die Stromnetz- und Kraftwerkparameter sich nicht signifikant ändern. Obwohl Variationen im Stromsystem wegen Lastvariationen oder Generatorausfälle stetig vorhanden sind, sind diese Variationen oft vorhersehbar und können im Rahmen einer manuellen Parametrierung berücksichtigt werden.

Der steigende Anteil erneuerbarer Erzeugung führt zu großen strukturellen Änderungen bei dem Betrieb von Stromnetzen und beeinflusst die resultierende Dynamik. Abhängig von Wetterbedingungen ändert sich die erneuerbare Erzeugung ständig und wird zusätzlich über große geographische Gebiete im Stromnetz verschoben. Erschwerend kommt hinzu, dass unter bestimmten Wetterbedingungen erneuerbare Energieerzeuger vollständig ausfallen können, was zu einer nahezu vollständigen konventionellen Erzeugung führt. Diese Einflüsse spielen im Augenblick insbesondere beim Inselnetzbetrieb eine große Rolle, da diese vielfach den größten Anteil erneuerbarer Erzeugung aufweisen. So gibt es Systeme, bei denen der Anteil erneuerbarer Erzeugung zwischen 0% und 100% variieren kann. Das verursacht einen intermittierenden Betrieb konventioneller Erzeugung, wie Dieselgeneratoren, was oft unerwünscht, aber vielfach unvermeidbar, ist.

Der stetig steigende Anteil erneuerbarer Erzeugung erschwert den sicheren und zuverlässigen Betrieb großer Stromnetze, wie zum Beispiel des Europäischen Energienet-

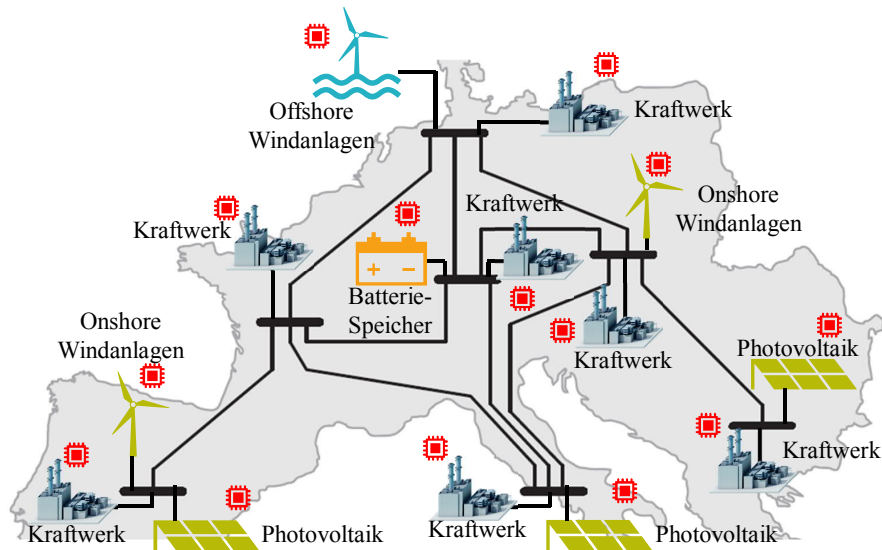


Abbildung 1: Zukünftiges Stromversorgungsnetz. Die Stromerzeugung erfolgt durch eine große Menge verteilter, volatiler Erzeuger. Dies führt zu einer sich ständig ändernden Systemdynamik, welche das Risiko eines Blackouts erhöht und zu einem suboptimalen Betrieb führen kann.

zes, stetig und führt zu bisher ungelösten Herausforderungen. So führt zum Beispiel, der ständig variierende Beitrag erneuerbarer und konventioneller Erzeugung zu starken, variablen Oszillationsmoden. Wird dies nicht berücksichtigt, steigt das Blackout-Risiko erheblich. Folglich, werden neue Regelungs- und Optimierungsmethoden benötigt, um die Robustheit und Flexibilität zukünftiger Stromnetze zu erhöhen. Dies führt zu zahlreichen Herausforderungen:

- Aufgrund der Komplexität des Gesamtsystems und der hohen Investitionskosten ist es praktisch nicht möglich, das existierende Automatisierungssystem vollständig durch neue Systeme zu ersetzen. Neue Konzepte müssen sich reibungslos in existierende Systeme integrieren lassen.
- Existierende Automatisierungssysteme haben das Vertrauen der Stromnetzbetreiber über Jahrzehnte langen Betrieb gewonnen. Bei einer Umstellung auf neue Automatisierungssysteme ist mit einem großen Widerstand zu rechnen, insbesondere aufgrund katastrophaler Folgen, wenn es zu Ausfällen und Fehlern kommen würde.
- Fast alle existierende Stromnetzregler operieren lokal: sie verwenden alleinige Messungen lokaler Größen, die sie auch regeln. Aufgrund der Sensibilität der Stromversorgung als zentrales Rückgrat der modernen Gesellschaft, sollte die Stabilität des Systems möglichst unabhängig von Kommunikationsnetzen sein.

Zur teilweisen Lösung dieser Herausforderungen, schlagen wir vor, “nur” die Parameter existierender, lokaler, strukturierter Reglern den sich ändernden Bedingungen im

Stromsystem anzupassen. Im vorgeschlagenen Konzept, überwacht und prognostiziert der Systembetreiber die variierende Dynamik. Stellt er fest, dass die Stabilität oder Performance des Systems gefährdet ist, löst er eine Parameteranpassung aus, und sendet die neuen Parameter an die Komponenten. Diese Herangehensweise berücksichtigt alle genannten Herausforderungen und führt zum nachfolgenden methodischen Problem, welches im Rahmen dieser Arbeit gelöst wird.

Problem 1 *Gegeben ein Stromsystem mit einstellbaren Reglerparametern, zum Beispiel der PID Regler und Filter, die sich innerhalb spezifizierter Grenzen einstellen lassen. Wie können diese Parameter schnell, auch für sehr große Stromsysteme, angepasst werden, um die Robustheit des Gesamtsystems zu erhöhen? Wie kann des weiteren der Parametrierungsprozess so durchgeführt werden, dass kein zentrales Gesamtmodell des Stromsystems benötigt wird und das nur ein beschränkter Austausch von Informationen zwischen den Teilsystemen benötigt wird?*

Gliederung und Forschungsbeiträge dieser Dissertation

Zur Lösung des genannten Problems werden in dieser Arbeit Methoden für die schnelle und effiziente Parametrierung strukturierter Regler basierend auf \mathcal{H}_∞ Optimierung, oft auch als strukturierte \mathcal{H}_∞ Reglersynthese bezeichnet, entwickelt.

Insbesondere werden zwei Methoden für die strukturierte \mathcal{H}_∞ Reglersynthese vorgeschlagen, und es werden Bedingungen, die die Systemstabilität für den geschlossenen Kreis für beide Ansätze garantieren, hergeleitet. Der erste Ansatz basiert auf dem Bounded-real Lemma, während der zweite Ansatz auf einer Frequenzabtastung basiert. Neben Simulationsstudien werden die Ansätze experimentell in einem Test-Inselnetz validiert, welches aus Wechselrichtern und einer Lastbank besteht. Hierbei wird nachgewiesen, dass die Ansätze sowohl die Robustheit, als auch das Verhalten auf eine Sprungstörung, des Systems verbessern, und sich auf große Systeme anwenden lassen. Die Ansätze werden mit anderen Verfahren für strukturierte \mathcal{H}_∞ Reglersynthese bezüglich Rechenzeit und Skalierbarkeit verglichen, um die Effizienz der vorgeschlagenen Ansätze nachzuweisen.

Im letzten Kapitel wird ein hierarchischer Ansatz für die Reglerparametrierung eingeführt, welches auf einer Modularisierung und Modellreduktion basiert. Dieser weist eine hohe Datensicherheit und Skalierbarkeit, verglichen mit zentralisierter Parameteranpassung, auf. Hierfür werden Bedingungen, die eine Gesamtkonvergenz des Ansatzes garantieren, aufgestellt und ein spezieller Ansatz für die verteilte Modellreduktion von Stromsystemen wird eingeführt. Die Methode wird am Beispiel des sogenannten IEEE 68-Knotensystem erprobt, und es wird nachgewiesen, dass sich gleiche Ergebnisse wie bei dem zentralisierten Ansatz errechnen lassen. Abschließend wird die Skalierbarkeit der Methode an einem großen Testsystem mit mehr als 2500 Zuständen und 1500 Reglerparametern nachgewiesen. Die einzelnen Forschungsbeiträge lassen sich wie folgt

zusammenfassen:

Formulierung des Syntheseproblems aus Regelungssicht (Kapitel 2). Eine mathematische Problemformulierung für die Reglerparametrierung in Stromnetzen wird hergeleitet. Für diesen Zweck wird ein Modellierungsansatz für Stromnetze mit expliziter Berücksichtigung von Parameterabhängigkeiten eingeführt. Basierend auf diesen Modellen werden geeignete Ausgänge-Gutefunktionen für die Beurteilung der Systemstabilität und Performance formuliert.

Neue \mathcal{H}_∞ Reglersynthesemethoden für die strukturierte Reglerparametrierung (Kapitel 3). Es werden schnelle und skalierbare Methoden für die Reglerparametrierung entwickelt. Hierfür werden zwei Ansätze für die \mathcal{H}_∞ Synthese eingeführt, welche auf dem Bounded Real Lemma und einer Frequenzabtastung basieren. Es wird nachgewiesen, dass beide Methoden eine stabilisierende Parametrisierung der Regler erlauben. Für die Frequenzabtastung wird ein Ansatz für die Frequenz-Gewichtung aufgezeigt, der die rechnerische Komplexität nicht erhöht und die einfacher zu spezifizieren ist im Vergleich zu Gewichtungsfunktionen.

Numerische Evaluierung der vorgeschlagenen Ansätze (Kapitel 4). Die vorgeschlagene Ansätze werden anhand dreier numerischen Beispielen erprobt. Die Erprobung erfolgt dabei mittels nichtlinearer Simulation unter Verwendung kommerzieller Stromnetzsimulationssoftware.

Experimentelle Validierung (Kapitel 5). Es wird die Effizienz der Ansätze an einem Test-Inselnetz experimentell aufgezeigt. Das Netz beinhaltet Wechselrichterbasierter Energieerzeugung, ohne Synchrongeneratoren. Es besteht aus sechs parallelgeschalteten Wechselrichtern, die auch isoliert vom globalen Verteilnetz betrieben werden können. Die Effizienz der Ansätze wird in Simulation und Messungen unter Berücksichtigung zwei und sechs Wechselrichtern validiert. Die Ansätze sind in der Lage, die Systemzuverlässigkeit in allen Fällen, im Vergleich zur manueller Einstellung, zu verbessern, und hierbei benötigen die Ansätze weniger Zeit und Aufwand.

Vergleich mit anderen Ansätzen (Kapitel 6). Es werden Vergleiche der vorgeschlagenen Ansätze mit anderen Methoden aus der Literatur durchgeführt. Da die meisten Ansätze aus der Literatur eine zusätzliche großflächige Kommunikation der Regler benötigen, ist ein direkter Vergleich nicht möglich. Deshalb erfolgt der Vergleich anhand von Zeit- und Frequenzbereichssimulationen. Die Methoden werden zusätzlich bezüglich der Rechenzeit, erzielten Ergebnissen und Skalierbarkeit verglichen. Dabei zeigt der vorgeschlagene Ansatz, basierend auf einer Frequenzabtastung, eine signifikante Verbesserung der Rechenzeit und Skalierbarkeit.

Multi-Szenario strukturierte \mathcal{H}_∞ Reglersynthese für Stromnetze (Kapitel 7). Die vorgeschlagene Ansätze werden für den Fall mehrerer zu parametrierenden Systemrealisierungen/Szenarien erweitert. Um diese Methoden auf Stromnetze anwenden zu können, wird zuerst ein Ansatz für die Modellierung von Fehlern in Stromsystemen eingeführt. Die Methoden werden mittels Simulationsbeispielen erprobt, welche nachweisen, dass die dynamische Sicherheit des Systems erhöht wird.

Skalierbare Reglerparametrierung für große Stromsysteme (Kapitel 8). Es wird ein hierarchischer Ansatz für die Reglerparametrierung eingeführt. Der Ansatz basiert auf einer Modularisierung und Modellreduktion. Dies erhöht die Datensicherheit und Skalierbarkeit. Es werden Konvergenzbedingungen für die Parametrierung vorgestellt, und es wird ein Ansatz für die verteilte strukturierte Modellreduktion in Stromnetzen eingeführt. Um die Effizienz des Ansatzes nachzuweisen, wird er auf das sogenannte IEEE 68 Bus System angewendet. Es wird gezeigt, dass eine ähnliche Güte wie für einen zentralen Ansatz errechnet werden kann. Die Skalierbarkeit des Ansatzes für ein großes System mit mehr als 2500 Zuständen und 1500 Reglerparametern wird beispielhaft nachgewiesen.

Zusammenfassung

Diese Dissertation umfasst mehrere, auf Stromnetze zugeschnittene, Ansätze zur Erhöhung der Robustheit linearer Systemen durch eine optimale Parametrierung von strukturierten Reglern. Die Methoden basieren auf linearen Matrixungleichungen und intelligenter Frequenzabtastungen. Sie werden mittels zahlreichen Simulationsstudien, wie auch experimentell an einem Inseltestsystem, validiert. Die vorgeschlagenen Methoden skalieren auf Systeme mit tausenden von Zuständen und Reglerparametern und lassen sich signifikant einfacher als ähnliche Methoden aus der Literatur berechnen.

Amer Mešanović

Magdeburg, den 14. Dezember 2020

1 Introduction and motivation

Reliable and secure electric power supply is vital for modern life. Power systems must operate without interruptions, despite constant outage of components, unknown load dynamics, changes in power generation, any many other disturbances. The reliable and safe operation of power systems is “guaranteed” today by a complex automation system, consisting of, e.g., PID controllers, notch filters, and lead-lag filters. It controls power system components spanning from power plants to inverters, flexible AC transmission system elements and loads [51, 80, 92]. This automation system is a result of years of practical experience and operation.

Tuning of the corresponding parameters of the used controllers is very important for reliable operation. Currently, this tuning is done during installation of the component in a time-consuming process. The controllers are typically not re-parameterized or changed until a large problem in the system occurs. Manual tuning has proven to be sufficient as long as the power system topology and power plant structure do not change significantly. Until recently, large traditional power plants were the main producers of electric energy. They operate permanently, leading to dynamic behavior of the system which remains mostly unchanged and known. While variations in the grid are unavoidably present due to load fluctuations or generator outages, these variations are foreseeable and can be taken into account during the manual tuning procedure. For example, the oscillatory modes of the European power system have known and quasi-constant frequencies and damping [36]. Figure 1.1 illustrates the situation in today’s European power system. The controllers of the power plants, representing the automation system, are marked red.

This “status-quo” is being challenged by the steadily rising amount of renewable generation [91]. The increased volatility of renewables leads to large changes in power system operation and the resulting dynamic behavior of power systems. Depending on the weather conditions, the power of renewable generation changes and can shift geographically across different areas of the power system. To counteract these effects, storage solutions or conventional generation are necessary to compensate for times when there is not enough renewable generation in the system. The resulting system structure is illustrated in Fig. 1.2. While there is hope, conventional fossil-fuel based generation will not be completely phased out of power systems. The expansion of storage solutions, such as batteries or hydrogen storage, which would allow to counteract for the volatility of renewables, is currently limited due to their price, geographical requirements, environmental impact, low efficiency etc. As long as the massive integration of storage solutions does not begin; conventional generation is will be required

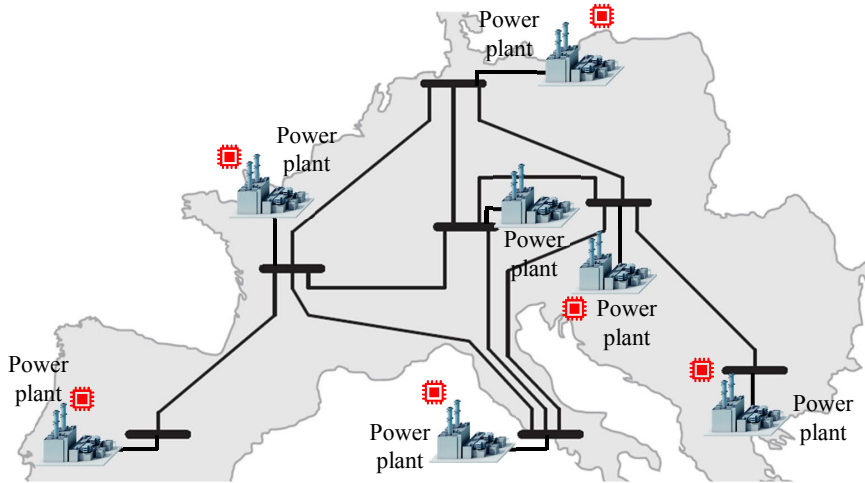


Figure 1.1: Today’s European power system: Power generation is dominated by large conventional generation. Controllers in the system, marked red, are manually tuned during installation.

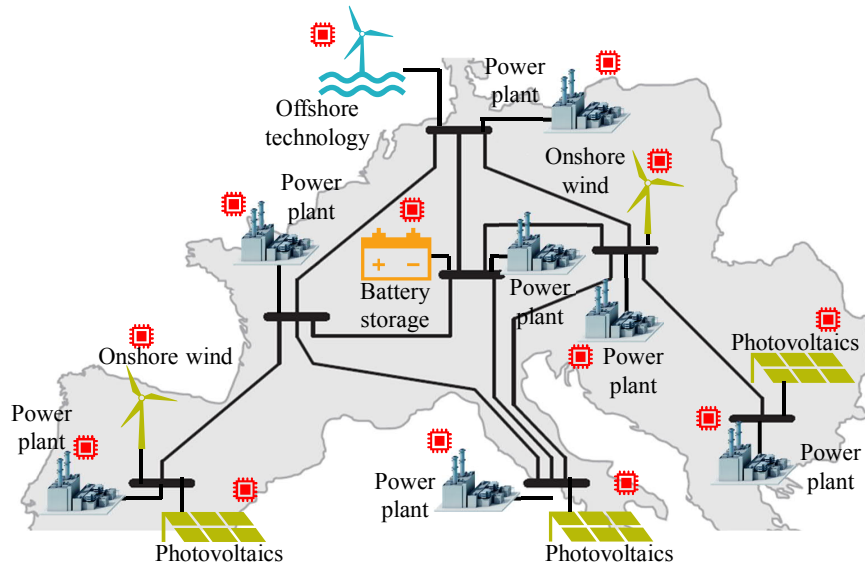


Figure 1.2: Future of power systems: Power generation is distributed among a large amount of distributed, volatile, generation. This causes changing eigenmodes in the system, increasing the risk of a blackout due to sub-optimally tuned controllers.

to compensate for periods when there is not enough renewable generation. Moreover, even if there is enough renewable generation in the European system to cover the load at any given moment, this power would need to be transported across large geographical distances, which is limited by the currently available transmission capacity of the power grid. Furthermore, reliance on remote generation (possibly coming from other countries) brings into question the security of supply in case of a, intentional or unintentional, failure in the transmission system. In conclusion, conventional generation will not be easily phased out of power systems.

The current impact of renewable generation is best visible for islanded microgrids

(off-grid systems), as they have a very large share of renewable generation [2, 102, 106]. For these systems, the percentage of instantaneous renewable generation varies from 0% to 100%. This causes intermittent and varying operation of conventional power generators, such as diesel generators, which is often undesired and largely impacts the dynamic behavior of the system.

As the share of renewable generation in large power systems, such as the European power grid or the Western interconnection in the USA, continues to increase, the operation of these systems also becomes increasingly challenging. For example, the constantly shifting mix of renewable and conventional generation can lead to time-varying oscillatory modes [4, 85]. If not handled, the controllers for large power systems become less effective, increasing the risk of blackouts.

New control and optimization methods, which are able to account for such changing dynamics, are necessary in order to improve robustness of future power systems. Designing such methods, however, is challenged, by several factors:

- It is practically impossible to completely replace the existing automation system with new solutions. New solutions need to be able to cope with existing equipment.
- The behavior of current automation systems has earned the trust of operators during decades of operation. A complete shift to a new automation system would meet large resistance, especially due to the possible catastrophic consequences if there are unforeseen design flaws.
- Almost all current controllers, which stabilize the system, are pure local controllers, i.e. they only require measurements from the component they are controlling. Due to its vital role and vulnerability, power system stability cannot depend on communication between components. Otherwise, communication outages and malicious attacks could compromise the power system. Power system and power plant operators are cautious to allow the power plant control to depend on external factors.

Following these requirements, we propose to **adapt parameters of existing, local, structured controllers** to the changing conditions, as illustrated in Fig. 1.3. For the proposed concept, the system operator monitors and forecasts the fluctuating power system dynamics. If the operator thereby notices that stability or performance of the system will be endangered, the operator tunes the parameters of local controllers and sends them to the various power system components via (slow) communication links, as illustrated with red dashed lines in Fig. 1.3.

The proposed approach addresses the previous challenges as follows:

- It is applicable even in the case that only a subset of running components can be reparameterized while old components remain intact, c.f. Fig. 1.3 by not connecting all controllers to the system operator via communication links.

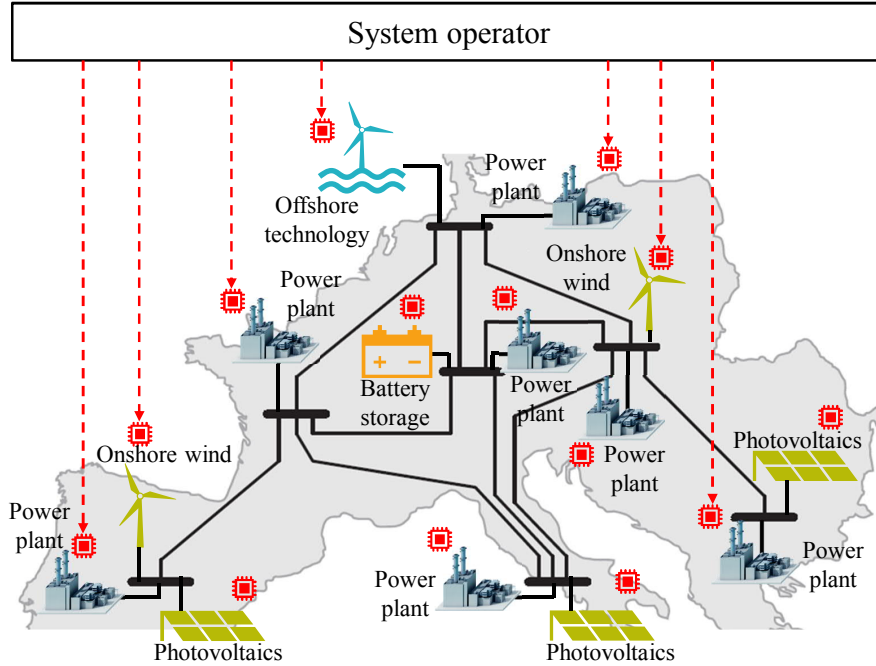


Figure 1.3: Proposed solution for the identified problem: the system operator tunes existing controllers in order to adapt them to the current system state. Dashed lines denote (slow) communication links for the parameter tuning.

- The current automation system will remain almost unchanged, it will only be reparameterized when necessary. New components can be added to the system as well, without restricting the applicability of the approach.
- With the proposed approach, controllers in the system still retain their local structure. Slow communication links need to be added, which periodically send parameters to the components. As long as the percentage of renewables is still below a critical threshold, and before the approach gains trust from power plant operators, the process of switching controller parameters to new values can even be done manually according to pre-calculated parameter tables. Even if the controller reparameterization is performed on-line, this can be done very slowly, e.g. by phone or e-mail. If a component cannot be reparameterized due to a communication outage or due to other failures, this can be taken into account during the parameter tuning procedure by switching to a “default” parameterization of the controller.

This basic concept, however, is challenged for large power systems that can have thousands of states and often consist of multiple coupled (sub)systems, belonging to different (sub)system operators, c.f. Fig. 1.4. The system operators are often not willing to fully exchange the parameters of their respective systems, as this would, e.g., expose vulnerabilities of their systems to others. Consequently, there is not a single entity which has access to all parameters of the power system. To address this issue, we introduce a hierarchical parameter tuning procedure, which does not require

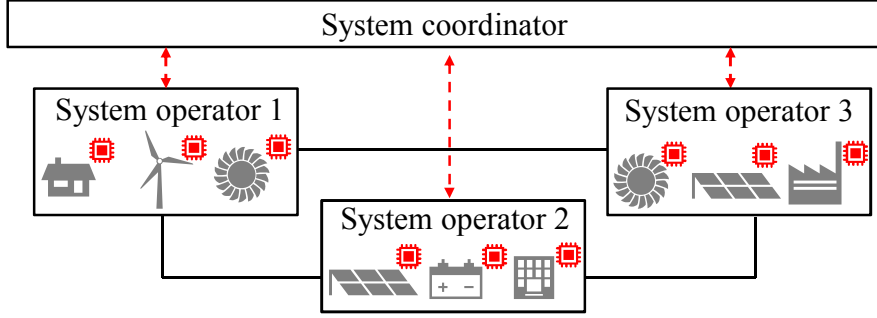


Figure 1.4: Structure of a power system coordinated by multiple (sub)system operators. Red dashed lines represent (slow) communication links, whereas solid lines represent physical connections. Each system operator tunes parameters of controllers in its respective system, as shown in Fig. 1.1.

that system operators exchange detailed parameters of their respective systems. The proposed approach is illustrated in Fig. 1.4. For this purpose, we introduce the concept of a system coordinator and the system operators exchange only the reduced models of their respective systems. Detailed models and parameters of the (sub)system models are hidden for the global decision, leading to increased data security and scalability of the approach.

Summarized, the proposed approach is adaptable to many practical requirements. However, the following research problem remains, which forms the main topic of this thesis:

Problem 1 *Given a power system with tunable parameters, such as parameters of PID controllers and filters, whose parameters can be adapted within pre-specified limits. How can one adapt parameters of these controllers fast, even for large power systems, to increase the optimality and robustness of the power system? Furthermore, how can the parameterization be performed such that a centralized detailed model of the large power system is not necessary?*

To clarify the main contributions and propositions, we briefly review possible control architectures for power systems. Power systems consist of elements which either produce or consume electric power, denoted as prosumers \mathcal{P}_i , which are interconnected through the power grid. Several approaches for distributed control of power systems have been proposed in the literature. They can be separated by their levels of decentralization, illustrated in Fig. 1.5 [115] for a system with three prosumers \mathcal{P}_1 , \mathcal{P}_2 and \mathcal{P}_3 . Almost all existing prosumers are controlled by local controllers, which use only measurements from the controlled prosumer, shown in Fig. 1.5(a). We denote the tunable parameters with \mathbf{K}_i , marked red.

Most works for controller synthesis introduce an additional control layer, the communication between the prosumers. In power systems, this is typically called wide-area control, due to the possibly large geographical distances between prosumers. We

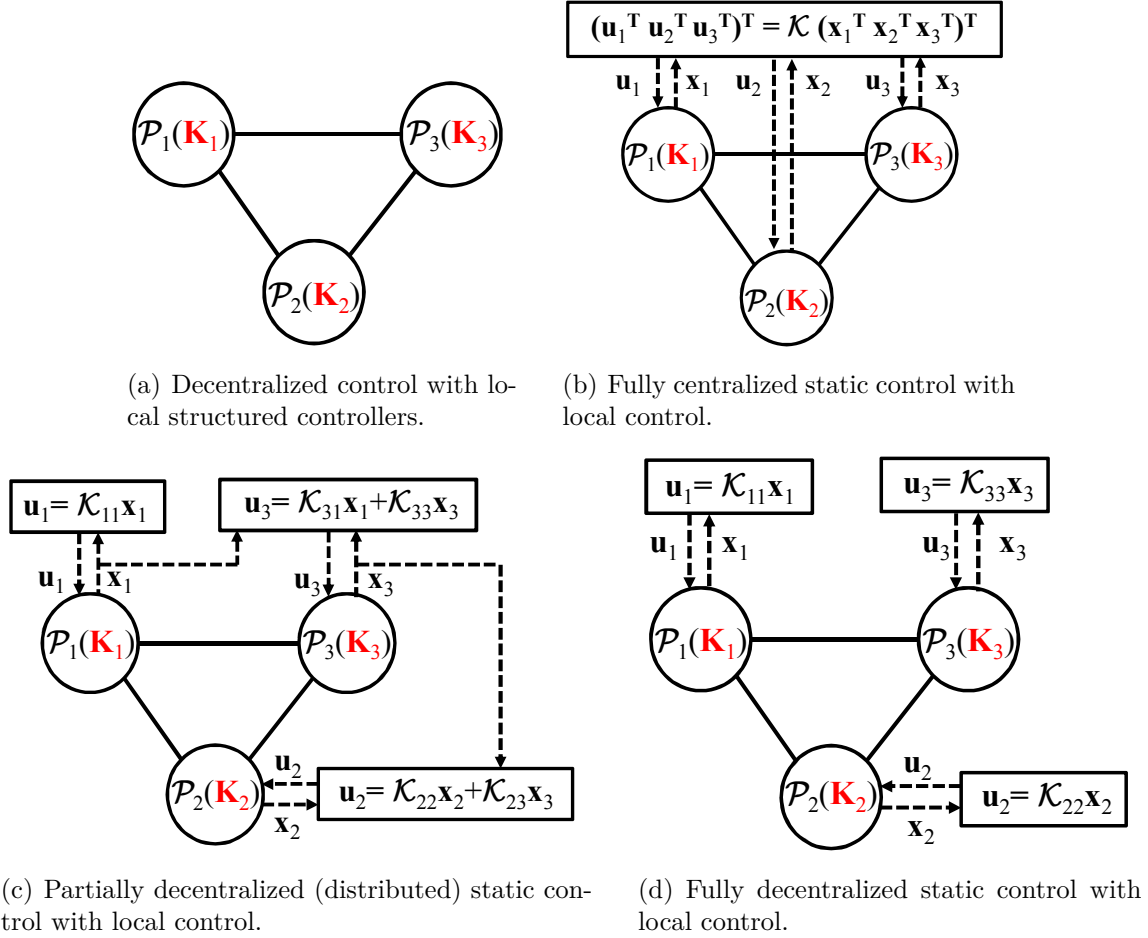


Figure 1.5: Control architectures with different levels of decentralization for three dynamic prosumers \mathcal{P}_i . Solid lines between the systems refer to physical links. Dashed lines are communication links. Red boldface \mathbf{K} s denote the vector of parameters of the local structured controllers, whereas a calligraphic \mathcal{K} denotes additional controllers with varying levels of decentralization.

explore different the levels of decentralization for static state-feedback controller synthesis. To do so, an additional wide-area control input \mathbf{u}_i is added for each prosumer. Note that state-feedback controllers do not have internal dynamic states. The controllers take as input the state vector \mathbf{x} , whereas the output of the controllers is the wide-area control input vector \mathbf{u} to the system, given by

$$\mathbf{u} = (\mathbf{u}_1^T \ \dots \ \mathbf{u}_{N_P}^T)^T = \mathcal{K} \cdot (\mathbf{x}_1^T \ \dots \ \mathbf{x}_{N_P}^T)^T = \mathcal{K} \cdot \mathbf{x}. \quad (1.1)$$

Here N_P is the number of prosumers, \mathbf{u}_i is the wide-area control input of \mathcal{P}_i , \mathbf{x}_i is the vector of states of \mathcal{P}_i , $\mathcal{K} \in \mathbb{R}^{n_u \times n_x}$ is the distributed controller gain matrix, n_u is the number of controller inputs and n_x is the total number of system states. We use the calligraphic \mathcal{K} to denote the gain matrix for additional controllers, and the boldface \mathbf{K}_i to denote the vector of tunable parameters of existing local controllers of \mathcal{P}_i . The term “static” originates from the fact that \mathcal{K} is a real-valued matrix, and not, e.g., a

transfer matrix with internal states.

A special case is a centralized controller, shown in Fig. 1.5(b). It requires the states of all prosumers \mathbf{x}_i to calculate the control input for all prosumers \mathbf{u}_i , i.e. $\mathbf{u}_i = \sum_{j=1}^{N_P} \mathcal{K}_{ij} \mathbf{x}_j$, where \mathcal{K}_{ij} is the appropriate sub-matrix of \mathcal{K} , corresponding to the control input of \mathcal{P}_i calculated from the states of \mathcal{P}_j . The drawback of this controller is that it requires fast communication from geographically remote prosumers, making it inherently vulnerable to communication failures. Furthermore, data security becomes an issue, as information from all prosumers is gathered in one place.

In order to reduce the number of necessary communication links between the subsystems, it is desirable to set some of the matrices \mathcal{K}_{ij} to zero. This way, the technical requirements for the realization of such a control law, in terms of required communication links, are lowered, c.f. Fig. 1.5(c). Such sparse and communication-based controllers are often referred to as distributed controllers. In the limit, all off-diagonal elements \mathcal{K}_{ij} , with $i \neq j$, become zero, and one obtains a fully decentralized control law, as illustrated in Fig. 1.5(d), parameterized through \mathbf{K}_i and \mathcal{K}_{ii} .

To summarize, a distributed system can have decentralization levels ranging from fully distributed control, as depicted in Figs. 1.5(a) and 1.5(d), various levels of partially distributed control, as shown in Fig. 1.5(c), to a fully centralized control solution, depicted in Fig. 1.5(b). We avoid introducing additional communication layers, and focus on directly tuning the parameter vectors \mathbf{K}_i .

1.1 Contributions

This thesis focuses on fast parameter tuning of fixed-structure controllers for large linear systems, often referred to as structured controller synthesis [6, 97]. The \mathcal{H}_∞ norm is thereby chosen as the optimization criterion, because it is, as it will be shown, a direct measure of the robustness towards unknown disturbances, as well as for the energy amplification of disturbances.

The main contributions of this thesis are:

1. A modeling framework for structured \mathcal{H}_∞ controller synthesis for power systems is developed and verified in simulation using commercial power system simulation software.
2. Two methods for structured \mathcal{H}_∞ controller synthesis are introduced. They are tailored towards power systems, however they are applicable to general linear systems. They allow for nonlinear parameter dependencies, making them applicable to almost all practically relevant linear systems. The first method is based on the Bounded-Real Lemma, whereas the second method is based on frequency sampling. Additionally, stability certificates are provided for both methods.

3. The proposed methods are evaluated on a range of numerical examples. The results of the controller tuning are verified in simulation using commercial power system simulation software, showing the practical applicability of the proposed approach.
4. An experimental validation of the approach is performed on a test microgrid consisting of six inverters. Automatic tuning practically eliminates all oscillations between the inverters. This demonstrates that the approach can be readily applied to existing control structures.
5. The proposed approach is compared to other approaches for the synthesis of distributed controllers, achieving a significantly better time-response and computation times in comparison to the other methods.
6. The modeling and parameter tuning framework is extended to multi-scenario tuning, which is applicable in cases when the exact state of the system is not known, or when multiple fault-scenarios need to be considered.
7. An approach for hierarchical controller synthesis is introduced, which can be applied to **larger systems** than centralized methods. Thereby, only reduced system models are exchanged, leading to increased data security. To do so, a method for distributed structured model reduction for power systems is developed and suitable conditions for the success of the optimization are derived. The hierarchical controller synthesis is successfully evaluated in two numerical examples.

In summary, this thesis presents methods for fast, data-privacy conserving, centralized and hierarchical structured \mathcal{H}_∞ controller synthesis in power systems. Thereby, we show the effectiveness of the proposed methods in simulations and experiments and show their advantages compared to other methods from the literature.

1.2 Related works

Controller synthesis for power systems typically exploits \mathcal{H}_∞ optimization, \mathcal{H}_2 optimization, and pole placement, c.f. [7, 64, 82, 86, 89, 100, 115, 120]. Other control design and analysis approaches are sensitivity analysis [10, 20, 66, 93], μ -synthesis [18], sliding mode controller design [58], the use of reference models [116], coordinated switching controllers [60], genetic algorithms and particle swarm based tuning [17, 34, 110, 117], model predictive control [31, 45], and time-discretization [54]. An overview of different methods for power oscillation damping can, for example, be found in [79]. However, most of the works either: consider simplified power system models [9, 10, 58, 64]; or add and design new controllers on top of the existing power systems [31, 45, 60, 82, 85, 86, 89, 100, 115, 120], see Figs. 1.5(b)-Fig. 1.5(d). The latter solutions require significant modification of existing control structures, which makes

practical application complex and expensive. Very few publications consider the optimization of existing controller parameters [7, 46, 65], as presented in Fig. 1.5(a). The approaches in these works employ heuristics [65], or assume a specific dependency on the parameters [7, 46].

Controller synthesis based on \mathcal{H}_∞ optimization has received significant attention. First approaches in the 1980s used algebraic Riccati equations for \mathcal{H}_∞ controller synthesis [26]. In the 90s, approaches based on linear matrix inequalities became popular, leading to convex solutions for unstructured state-feedback controller synthesis based on the Bounded-Real Lemma [32]. If the controller structure is fixed and only the parameters are tuned according to \mathcal{H}_∞ optimization, one refers to structured \mathcal{H}_∞ controller tuning [6, 97]. Structured controller synthesis, exploiting the bounded real lemma and additional improvements and refinements are, e.g., used in [8, 24, 38, 40, 43, 49, 99, 100]. Alternative tuning approaches exist, such as non-smooth optimization [5, 37], and bisection [48].

In recent years, the focus in structured \mathcal{H}_∞ optimization shifted towards more efficient methods to find local minima for large systems. These methods are often based on frequency sampling, leading to fast synthesis [6, 14, 46]. This, however, removes the guarantee that a stable controller is obtained after tuning. To solve this issue, [6, 46] introduce stability constraints based on the Nyquist criterion. In [14], the assumption is made that the controlled plant (without controllers) is asymptotically stable. In this case, the boundedness of the \mathcal{H}_∞ norm of the system sensitivity matrix is a necessary and sufficient condition for stability.

To the authors' knowledge, only previous work of the authors [73] considers distributed or hierarchical structured \mathcal{H}_∞ synthesis of controllers. Note that, even though many works consider the synthesis of distributed controllers, e.g. [53, 99], the synthesis procedure itself is centralized. Works which consider distributed controller synthesis usually assume a specific system structure and design unstructured controllers, see e.g. [23] and references therein. Recently, hierarchical approaches for steady-state optimization of power systems emerged [101].

1.3 Outline

The work is structured in the following chapters:

Chapter 2: The controller synthesis problem. In this chapter, a mathematical formulation for the proposed controller tuning for power system is introduced. For this purpose, a model of the power system with explicit parameter dependencies is first shown. Then, appropriate outputs to measure the system resiliency and performance are introduced. Finally, the overall mathematical problem is formulated.

Chapter 3: Structured controller tuning with stability guarantees. In this chapter, we focus on finding a fast and scalable centralized method to solve the

parameter tuning problem. For this purpose, two methods for \mathcal{H}_∞ synthesis are introduced, based on the bounded real lemma and frequency sampling. It is shown that both methods will produce a stabilizing parameterization, thereby minimizing the system \mathcal{H}_∞ norm. We show a frequency-weighting approach for the frequency sampling method, which does not increase computational complexity and can be used in case of weighting functions.

Chapter 4: Numerical evaluation. The efficiency of the proposed methods are outlined for three numerical examples. The results are validated using nonlinear simulations in commercial simulation software to do a practically relevant evaluation.

Chapter 5: Experimental validation. We demonstrate the applicability of the proposed approach by tuning controller parameters of a real islanded microgrid running without synchronous generation. The grid consists of six parallel grid-forming inverters, which provide islanding capability to the system, even without synchronous generation. We first show an unstable response to a load step of two parallel grid-forming inverters. To stabilize the system, manual tuning methods and iterative simulation are first employed. The results of the manual tuning, as well as the accuracy of the mathematical model, are verified against measurements. To decrease the engineering time and further improve the system performance, the proposed \mathcal{H}_∞ tuning method is applied to the system. The effectiveness of the method is validated in simulation and measurements in the grid with two, as well as with six inverters, and a load. Optimal controller tuning is able to improve the system reliability in all cases, compared to manual tuning, while requiring less time and engineering effort.

Chapter 6: Performance comparison. In this chapter, we compare the proposed methods for structured \mathcal{H}_∞ controller synthesis from Chapter 3 with other methods from the literature. The comparison is made first with regard to the considered application, i.e. controller synthesis in power systems. As most approaches introduce an additional wide-area control layer, c.f. Figs. 1.5(b)- 1.5(d), a direct comparison with the proposed approach is not possible. Thus, the focus of this comparison is on the achieved results in the time- and frequency domain, observed on a numerical example. In the second comparison, we focus on computational efficiency of methods which consider structured \mathcal{H}_∞ controller synthesis. For this purpose, we adapt four methods from literature to the considered application, and compare them on several numerical examples with respect to the computation time, achieved result, and scalability.

Chapter 7: Multi-scenario structured controller synthesis. We extend in this chapter the proposed methods to cases when one controller parameterization is needed for several system realizations/scenarios. To this end, we present a framework for modeling failures in power systems, such that they can be considered with the multi-scenario controller tuning. Finally, the approach is applied to increase dynamic security in a numerical example.

Chapter 8: Scalable and Data Privacy Conserving Controller Tuning for Large-Scale Networks. We introduce in this chapter a hierarchical approach

for the controller tuning, based on model reduction, which increases data security and scalability of the tuning, compared to centralized tuning. Thereby, we examine conditions for the success of the approach and introduce an approach for distributed model reduction of power systems. We apply the proposed hierarchical tuning method to the IEEE 68 bus system to show its effectiveness. Furthermore, we show that a similar system performance is obtained for this system as with a centralized method. Finally, we show the scalability of the approach on a large power system with more than 2500 states and about 1500 controller parameters.

2 The controller synthesis problem

To tackle the parameter tuning problem, we will first derive an appropriate control oriented modeling framework for power systems. This should be applicable to a wide class of power systems and should capture the parameter dependencies of the controllers. It should be sufficiently detailed such that it is trusted by experts, and should in the ideal case be usable in commercial power system simulation software. On the other side, it should be simple enough to enable fast parameter tuning. For this purpose, a tailored modeling framework is proposed in Section 2.1. Furthermore, appropriate performance outputs are defined in Section 2.2, which are used to assess the robustness and performance of the closed loop system. Finally, an appropriate cost function, i.e. tuning goal, is defined in Section 2.3. The overall mathematical problem formulation is presented in Section 2.4.

2.1 Control oriented power system modeling

Power systems consist of many components, c.f. 2.1, such as power plants, renewable power generation, storage systems and households. These components are referred to as prosumers, as they can either produce or consume electric power. We distinguish between dynamic and static prosumers.

Dynamic prosumers, e.g. power plants, are systems with internal dynamic states, denoted with \mathcal{P}_i , $i = 1 \dots N_D$. They might possess structured controllers, whose parameters \mathbf{K}_i can be tuned, marked with red in Fig. 2.1. We consider dynamic prosumers \mathcal{P}_i which control their voltage magnitude V_i and phase θ_i at the point of connection to the power grid, whereas their power infeed into the grid, P_{pi} and Q_{pi} , are the external inputs for the controllers. Examples are conventional power plants with synchronous generators [51], as depicted in Fig. 2.1, where V_i and θ_i are outputs of \mathcal{P}_i , and P_{pi} , Q_{pi} are the inputs. Note that dynamic prosumers which have P_{pi} and Q_{pi} as output can also be considered.

Static prosumers, such as loads and some renewable generation, have no internal states and are characterized through their active and reactive power infeed, denoted with P_{si} and Q_{si} , respectively. The example power system shown in Fig. 2.1 depicts four static prosumers, marked with blue. We collect infeeds of static prosumers into vectors \mathbf{P}_s and \mathbf{Q}_s , which are considered as external inputs. Renewable generation and loads are often modeled as static prosumers [83, 87]. The power infeed of these elements cannot be fully controlled, and we consider these infeeds as the disturbance inputs for the controller tuning. Static prosumers also model components with a slow

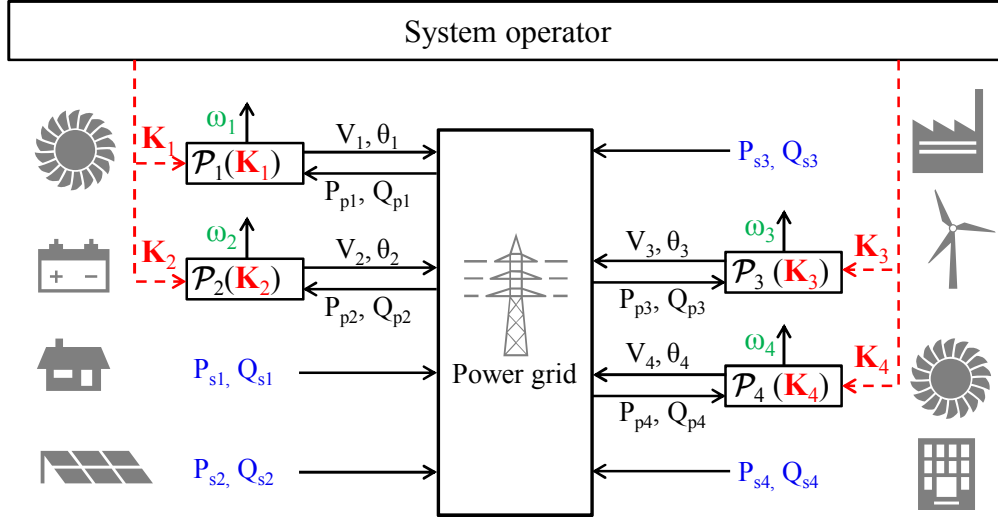


Figure 2.1: Exemplary power system consisting of four dynamic prosumers \mathcal{P}_i and four static prosumers P_{si}, Q_{si} connected through a power grid. The tunable controller parameters \mathbf{K}_i of dynamic prosumers are marked red. The static prosumers, marked with blue, are considered as disturbance inputs into the system. The frequencies ω_i of each \mathcal{P}_i are performance outputs, marked in green.

dynamic behavior, such as aggregated powers of small prosumers. For this reason, a subset of \mathbf{P}_s and \mathbf{Q}_s is chosen as the disturbance input \mathbf{w}_s . The voltage phasors of buses with static prosumers have a magnitude \mathbf{V}_s and angle $\boldsymbol{\theta}_s$. Static and dynamic prosumers are coupled through the power grid.

Depending on the infeed of renewable generation and load, the system dynamic behavior changes. The basic idea is that if the system operator notices that the resiliency of the system decreases, the controller parameters \mathbf{K}_i of the dynamic prosumers are retuned to increase the system resiliency. The reparameterization process is depicted with red dashed lines in Fig. 2.1.

In the following subsections, we outline the structure and dynamics of the power grid and prosumers and present possible models.

2.1.1 Power grid

The power grid consists of power lines, cables, transformers etc. which interconnect dynamic and static prosumers. In principle, power lines and cables are dynamic. However, their time constants are orders of magnitude smaller than the dynamics relevant for stability of the system, which are often slower than 10 Hz [51]. For this reason, the dynamics of the interconnection elements are neglected [51, 98]. Consequently, the grid, i.e. the power flow, is typically described by the algebraic power flow equations. Without loss of generality, we assume that all buses with no power infeed are

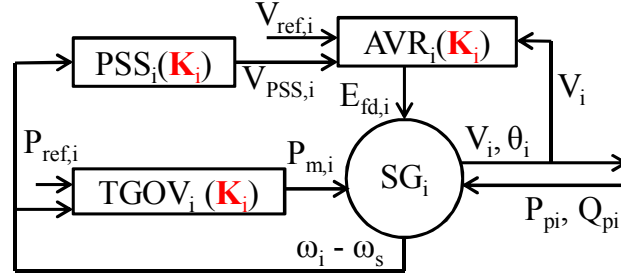


Figure 2.2: Simplified model of a dynamic prosumer \mathcal{P}_i , a power plant. It consists of a synchronous generator (SG_i), automatic voltage regulator and exciter (AVR_i), power system stabilizer (PSS_i), and of a turbine and governor model (TGOV_i).

eliminated beforehand by the so-called Kron reduction [25], which results in

$$P_i = \sum_{j=1}^{N_B} V_{Bi} V_{Bj} (G_{cij} \cos \Delta\theta_{Bij} + B_{sij} \sin \Delta\theta_{Bij}) \quad (2.1a)$$

$$Q_i = \sum_{j=1}^{N_B} V_{Bi} V_{Bj} (G_{cij} \sin \Delta\theta_{Bij} - B_{sij} \cos \Delta\theta_{Bij}), \quad (2.1b)$$

where N_B is the number of buses (nodes) in the power system and is equal to the total number of dynamic and static prosumers in the grid, P_i and Q_i , are the injected active and reactive powers into the i -th bus (node) in the grid by a dynamic prosumer (P_{pi} , Q_{pi}) or a static prosumer (P_{si} , Q_{si}), where $\mathbf{P} = \text{vec}_i(P_i) = (\text{vec}_i(P_{pi})^T \text{vec}_i(P_{si})^T)^T$, and $\mathbf{Q} = \text{vec}_i(Q_i) = (\text{vec}_i(Q_{pi})^T \text{vec}_i(Q_{si})^T)^T$, V_{Bi} and θ_{Bi} are the magnitude and angle of the voltage phasor at the i -th bus, where $\mathbf{V}_B = \text{vec}_i(V_{Bi}) = (\text{vec}_i(V_i)^T \text{vec}_i(V_{si})^T)^T$, $\mathbf{\theta}_B = \text{vec}_i(\theta_{Bi}) = (\text{vec}_i(\theta_i)^T \text{vec}_i(\theta_{si})^T)^T$, $\Delta\theta_{Bij} = \theta_{Bi} - \theta_{Bj}$, and G_{cij} and B_{sij} are the elements of the conductance and susceptance matrix of the grid [51]. Note that P_{pi} , Q_{pi} , V_i , and θ_i are used here in the same context as in Fig. 2.1.

2.1.2 Dynamic prosumers and tunable parameters

The proposed modeling framework allows for arbitrary dynamic prosumers to be included in the power system model. We outline two exemplary prosumers and their models. which cover many practical applications.

Power plants. Typical power plants consist of a synchronous generator with controllers and actuators, as shown in Fig. 2.2. We use a 6-th order model for the synchronous generator (SG_i). For details, we refer the interested readers to [51].

The governor and turbine (TGOV_i) control the generator frequency by adapting the mechanical power $P_{m,i}$ transferred to the synchronous generator. An exemplary TGOV_i is shown in Fig. 2.3, modeling the tandem-compound steam prime mover, including a speed governing system, a four-stage steam turbine, and a shaft with one mass [69]. The TGOV_i proportional gain $R_{p,i}$, marked red in Fig. 2.3, can be tuned.

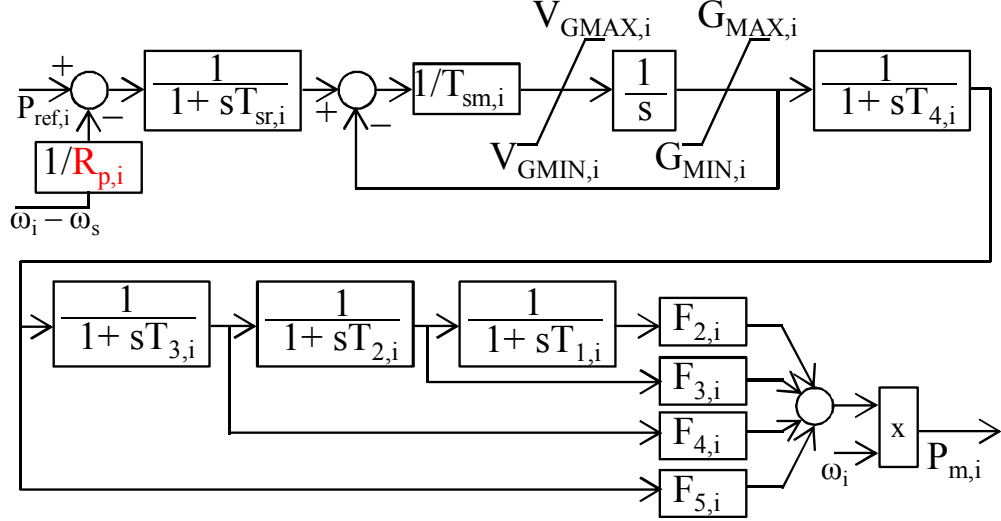


Figure 2.3: Dynamic model of the turbine and governor from [69]. The frequency droop gain of the governor $R_{p,i}$ is an optimization variable.

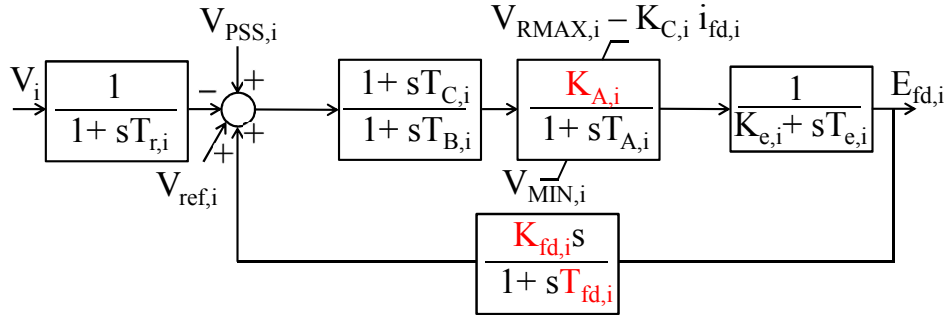


Figure 2.4: Dynamic model of AVR_{*i*} [67], where $T_{r,i}$ is the transducer time constant, $T_{C,i}$ and $T_{B,i}$ are lead-lag filter time constants, $K_{A,i}$ is the AVR gain, $T_{A,i}$ is the AVR lag time constant, $K_{e,i}$ and $T_{e,i}$ are the exciter parameters, and $K_{fd,i}$ and $T_{fd,i}$ additional damping coefficients of the AVR. We assume that $K_{A,i}$, $K_{fd,i}$, and $T_{fd,i}$, marked red, are tunable.

All other parameters are determined by the real physical characteristics of the system and cannot be tuned.

The generator automatic voltage regulator (AVR_{*i*}) controls the terminal voltage of the generator via the field winding voltage $E_{fd,i}$ from the exciter. An exemplary AVR_{*i*} model is shown in Fig. 2.4, based on the IEEE ST1 model [67]. The inputs to the exciter are the reference voltage $V_{ref,i}$, the power plant terminal voltage V_i , and the input from the power system stabilizer $V_{PSS,i}$. The output of the exciter is the field winding voltage $E_{fd,i}$. We assume that the exciter gain $K_{A,i}$, as well as the damping coefficients $K_{fd,i}$ and $T_{fd,i}$, marked red in Fig. 2.4, can be tuned.

The objective of AVR_{*i*} is a constant terminal voltage of the generator. It can reduce the damping properties of a synchronous generator [39, 51]. For this reason, power plants are sometimes equipped with a power system stabilizer (PSS_{*i*}), which couples

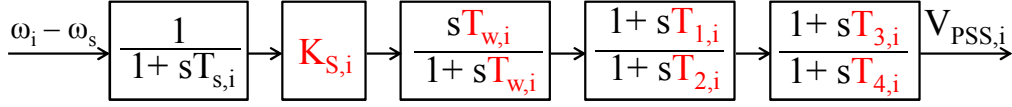


Figure 2.5: Dynamic model of the simple power system stabilizer (taken from [51, 77]), where $K_{S,i}$ is the PSS gain, $T_{w,i}$ is the washout time constant, $T_{1,i}$ - $T_{4,i}$ are the lead-lag filters time constants, and $T_{s,i}$ is the sensor time constant. All of the PSS parameters are tunable, except the sensor time constant.

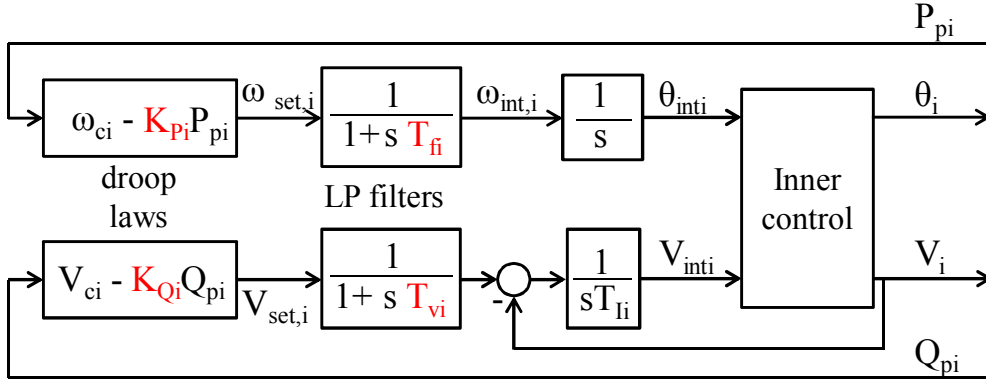


Figure 2.6: Simplified model of a dynamic prosumer \mathcal{P}_i , an inverter with so-called droop controls.

frequency and voltage control for power plants. PSSs are analogue or digital controllers, with the task to improve the system stability and increase the damping of oscillations in power systems. We consider that the PSS_i takes as input the deviation of the generator frequency ω_i from the nominal system frequency ω_s , while its output $V_{PSS,i}$ is an additional input of the AVR_i . An exemplary PSS model is shown in Fig. 2.5 [51, 89]. All of its parameters are assumed to be tunable, marked red in Fig. 2.5, except the sensor time constant.

In addition to exemplary controller models shown here, many different controllers are used in practice, see e.g. [44].

Inverters. We consider inverters which control the voltage and frequency at their terminals, called voltage-source inverters (VSI), or inverters in grid-forming mode. For dynamics below 10 Hz, modeling the high-frequency switching of power electronic elements in the inverters is often not necessary. Instead, the switching components in the inverters are approximated as ideal voltage sources with droop controllers for voltage amplitude and frequency, c.f. Fig. 2.6. The DC link capacitors of the inverters are not considered, as we assume that the internal control of the inverters is fast enough to compensate for the changes on the DC side. Such simplifications comply with measurements shown in [88], and with the experiments considered in Chapter 5. The outlined structure represents the behavior of a SINAMICS inverter [3].

In grid-forming mode, the i -th inverter controls the magnitude V_i and phase θ_i of the

voltage on its terminals, whereas the active and reactive power infeed of the inverter result from the power flow. The frequency setpoint of the inverter ω_{seti} is determined by the so-called droop equation

$$\omega_{seti} = \omega_{ci} - K_{P_i} P_{pi}. \quad (2.2)$$

Here ω_{ci} is the frequency setpoint for zero load, P_{pi} is the measured active power infeed of the i -th inverter, and K_{P_i} is the frequency droop gain. The setpoint ω_{seti} is filtered with a first-order low-pass filter with the time constant T_{fi} and integrated to obtain the internal voltage phase θ_{inti} . Analogously, the voltage setpoint V_{seti} is determined with the droop equation

$$V_{seti} = V_{ci} - K_{Q_i} Q_{pi}. \quad (2.3)$$

Here V_{ci} is the voltage setpoint with no reactive power generation, Q_{pi} is the measured reactive power infeed of the i -th inverter, and K_{Q_i} is the frequency droop gain. The setpoint V_{seti} is filtered with a time constant T_{vi} , and serves as the setpoint for the integral voltage controller. The output of the integral controller is the internal voltage V_{inti} .

The resulting θ_{inti} and V_{inti} are used as references to the internal control loops which run at a much higher frequency. As the internal control loops are not modeled due to their fast dynamics, we assume $\omega_i = \omega_{inti}$, $\theta_i = \theta_{inti}$ and $V_i = V_{inti}$.

The tunable inverter parameters are marked red in Fig. 2.6, they are: $\mathbf{K}_i = (K_{P_i}, K_{Q_i}, T_{fi}, T_{vi})^T$. For simplicity, we do not modify the voltage I-controller time constant, as it serves for slow steady-state error elimination, and we observe the transient response of the inverters in the time interval of several seconds.

2.1.3 Overall model

Combining the power grid equations (2.1) with the prosumer models leads to a set of differential-algebraic nonlinear equations of the form

$$\dot{\mathbf{x}} = f(\mathbf{x}, \mathbf{w}, \mathbf{K}) \quad (2.4a)$$

$$0 = h(\mathbf{x}, \mathbf{w}, \mathbf{K}). \quad (2.4b)$$

Here $\mathbf{x} \in \mathbb{R}^{N_x}$ combines all dynamic prosumer states, $\mathbf{w} \in \mathbb{R}^{n_w}$ is the vector of disturbance inputs, represented by a subset of \mathbf{P}_s and \mathbf{Q}_s , $\mathbf{K} \in \mathbb{R}^{N_t}$ is the vector of tunable controller parameters of all dynamic prosumers, where N_t denotes the total number of tunable parameters in the system, f describes the prosumer dynamics, and h represents the power flow equation (2.1).

As the problem is challenging, we linearize (2.4) around a known steady-state \mathbf{x}_0 with the known input \mathbf{w}_0 . While this is an approximation, it allows us to use linear

systems methods. It has furthermore been shown to be sufficient even for some large-scale disturbances, see Chapter 4, as well as [83].

Remark 1 (steady-states) *The steady state of the power grid depends on the voltages and power infeeds, which can be determined using commercial tools [35, 103]. This allows to calculate the steady-states of dynamic prosumers \mathbf{x}_0 .*

The linearized algebraic equation (2.4b) has full rank, and a linear-time invariant system is obtained after linearization of (2.4)

$$\Delta \dot{\mathbf{x}} = \tilde{A}(\mathbf{K})\Delta \mathbf{x} + \tilde{B}(\mathbf{K})\Delta \mathbf{w}. \quad (2.5)$$

Here $\Delta \mathbf{x} = \mathbf{x} - \mathbf{x}_0$, and $\Delta \mathbf{w} = \mathbf{w} - \mathbf{w}_0$. Subsequently, we skip Δ for notational convenience, i.e. we focus on deviations from the linearization point in the remainder of this work. Note that the system matrix $\tilde{A}(\mathbf{K})$ has an eigenvalue at zero, as the coupling power flow equation (2.1) is invariant under offsets $\tilde{\theta}_i = \theta_i + \delta\theta$, where $\delta\theta \in \mathbb{R}$ is identical for all i . Reducing this zero eigenmode [115], leads to

$$\dot{\mathbf{x}} = A(\mathbf{K})\mathbf{x} + B(\mathbf{K})\mathbf{w}. \quad (2.6)$$

We note that (2.6) is exponentially stable for a suitable choice of \mathbf{K} , as all practical power systems have controllers which stabilize the system.

2.2 Performance outputs

In power systems, the frequencies of the dynamic prosumers, defined with $\omega_i = \dot{\theta}_i$, where θ_i is the angle of the voltage phasor of \mathcal{P}_i are of key interest to assess the system performance [51]. Thus, we choose the vector of frequencies as the performance output

$$\mathbf{y} = (\omega_1 \quad \dots \quad \omega_{N_D})^T, \quad (2.7)$$

where N_D denotes the number of dynamic prosumers. The performance outputs are marked green in Fig. 2.1. These performance outputs also ensure detectability of the system states [51]. Note that ω_i is a dynamic state in (2.6). Hence, we can write $\mathbf{y} = C\mathbf{x}$, where the C matrix is not a function of the controller parameters and it contains ones to select the appropriate states from \mathbf{x} .

With this performance output, the full power system model is given by a linear time-invariant multi-input multi-output system

$$\dot{\mathbf{x}} = A(\mathbf{K})\mathbf{x} + B(\mathbf{K})\mathbf{w} \quad (2.8a)$$

$$\mathbf{y} = C\mathbf{x}. \quad (2.8b)$$

The corresponding frequency domain formulation becomes

$$G(\mathbf{K}, s) = C (sI - A(\mathbf{K}))^{-1} B(\mathbf{K}). \quad (2.9)$$

Note that the presented simple model formulation can be used for many other applications, such as optimization of AC/DC systems. Modeling extensions are presented in Appendix B, and numerical examples are considered in Chapter 4.

2.3 \mathcal{H}_∞ parameter optimization

Given the power system model (2.8) and (2.9), the focus of the parameter tuning procedures is to determine the parameters minimizing a cost function. The overall goal is to adapt the controller parameters of G to improve its robustness and stability margin with respect to disturbances. For this reason we choose the \mathcal{H}_∞ norm of $G(\mathbf{K}, s)$ for optimizations, denoted with $\|G(\mathbf{K}, s)\|_\infty$, and defined by [13]

$$\|G(\mathbf{K}, s)\|_\infty := \sup_{s \in \mathbb{C}_{>0}} \bar{\sigma}(G(\mathbf{K}, s)) \quad (2.10)$$

$$= \sup_{\omega \in \mathbb{R}} \bar{\sigma}(G(\mathbf{K}, j\omega)), \quad (2.11)$$

where $\bar{\sigma}(\cdot)$ denotes the largest singular value of a matrix. Note that (2.11) only holds for stable systems, i.e. when $G(\mathbf{K}, s) \in \mathcal{RH}_\infty$.

We chose the \mathcal{H}_∞ norm as the minimization of $\|G(\mathbf{K}, s)\|_\infty$ improves the system robustness to unknown disturbances (small-gain theorem) [119]. Secondly, the \mathcal{H}_∞ norm represents the maximal amplification of amplitude of any harmonic input signal in any output direction. Thus, minimizing the \mathcal{H}_∞ norm minimizes the worst-case amplification of oscillation frequencies after a disturbance. Finally, minimization of $\|G(\mathbf{K}, s)\|_\infty$ improves oscillation damping in the system as well, as outlined in Appendix A.

2.4 Overall problem setup

With a small abuse of notation, we subsequently generalize (2.9) to allow for parameter dependent $C(\mathbf{K})$ and $D(\mathbf{K})$ matrices. We do so as they may become parameter-dependent if we choose other performance outputs, such as the active powers of dynamic prosumers, or if other dynamic prosumer types are considered. Doing so, we ensure generality of the proposed approaches. Summarized, the following optimization problem is obtained

$$\min_{\mathbf{K}} \|G(\mathbf{K}, s)\|_\infty = \left\| C(\mathbf{K})(sI - A(\mathbf{K}))^{-1} B(\mathbf{K}) + D(\mathbf{K}) \right\|_\infty \quad (2.12a)$$

$$\text{s.t. } \underline{\mathbf{K}} \leq \mathbf{K} \leq \bar{\mathbf{K}}. \quad (2.12b)$$

Here (2.12b) represents box constraints on the controller parameters, e.g. due to physical limitations, and $\underline{\mathbf{K}}/\overline{\mathbf{K}}$ may be $\pm\infty$. Such constraints may result, e.g., from physical constraints [52], or from practical experience.

Note that $G(\mathbf{K}, s)$, with the matrices $A(\mathbf{K})$, $B(\mathbf{K})$, $C(\mathbf{K})$, and $D(\mathbf{K})$, nonlinearly depends on the pre-given controller parameter vector \mathbf{K} . One says that the controllers in G are structured, and only their parameters \mathbf{K} need to be tuned. Doing so is called structured \mathcal{H}_∞ controller synthesis [6, 97]. Additional constraints can also be added, such as steady-state constraints, equality constraints for parameters, stability constraints for subsystems etc.

2.5 Problem complexity

Problem (2.12) is a general structured \mathcal{H}_∞ controller synthesis problem for linear systems. A special case of structured controller synthesis is the so-called static output feedback \mathcal{H}_∞ controller synthesis problem, which considers controller parameter tuning of the following system

$$\dot{\mathbf{x}} = A'\mathbf{x} + B'\mathbf{w} + B_u\mathbf{u} \tag{2.13a}$$

$$\mathbf{z} = C_z\mathbf{x} + D_z\mathbf{w} \tag{2.13b}$$

$$\mathbf{y} = C'\mathbf{x} + D'\mathbf{w} + D_u\mathbf{u} \tag{2.13c}$$

$$\mathbf{u} = K\mathbf{z}. \tag{2.13d}$$

Here K represents a matrix of controller parameters. Note that the dependency of the system matrices on the controller parameters is linear. Still, the static output feedback synthesis problem is in general NP-hard [94], c.f. [94], for various algorithms for static output feedback synthesis and references therein. Compared to static output feedback \mathcal{H}_∞ synthesis, we consider nonlinear parameter dependencies of the system matrices, as well as box-constraints on the controller parameters. Consequently, (2.12) is in general NP-hard.

As the global optimum of NP-hard problems cannot be found in polynomial time, we focus on finding local minima of (2.12) efficiently, which is, as shown, practically feasible [14], but challenging for large scale systems. Considering the broad problem class, i.e. avoiding simplifications, we retain the generality of the proposed approaches. Furthermore, avoiding possible transformations of controller parameters, additional constraints can be easily specified, without having to make any changes to the solution procedure.

2.6 Summary

In this chapter, we presented an mathematical formulation of Problem 1, which is a structured \mathcal{H}_∞ controller synthesis problem. We first outlined a modeling framework for the considered power systems which includes nonlinear algebraic power flow models and dynamic prosumer models. We linearized the model, eliminating algebraic equations, while retaining the nonlinear dependency of the controller matrices on the vector of tunable parameters \mathbf{K} . The frequencies of dynamic prosumers are important for operation and are thus selected as performance outputs, which quantify the dynamic performance of the system. Finally, the overall problem is formulated as a structured \mathcal{H}_∞ tuning problem before the chapter is concluded with a discussion about the complexity of the obtained synthesis problem.

3 Structured controller tuning with stability guarantees

This chapter introduces fast and scalable methods to find a (sub)optimal solution of the parameter tuning Problem 1. As this problem is in general NP-hard, we focus on methods which find local minima.

Two methods for \mathcal{H}_∞ synthesis are presented in Sections 3.1 and 3.2. Suitable weighting schemes for both methods are proposed in Section 3.3, before the chapter is summarized.

3.1 Structured controller synthesis based on the Bounded real Lemma

The first method is based on the so-called Bounded Real Lemma. It allows us to reformulate the \mathcal{H}_∞ tuning problem, defined in the frequency domain, with the time-domain description of the problem by introducing an additional optimization variable: the Lyapunov matrix. The method uses the iterative coordinate descent, also known as P-K iteration, to find a (sub)optimal controller parameterization, where the parameter dependency is iteratively linearized such that a linear matrix inequality problem is obtained in each iteration.

The Bounded-real Lemma states the following:

Lemma 1 (Bounded-Real Lemma) [32] *Consider the continuous-time transfer function $G(s)$ with the realization $G(s) = D + C(sI - A)^{-1}B$. The following statements are equivalent*

- *The system $G(s)$ is asymptotically stable and $\|G(s)\|_\infty < \gamma$.*
- *There exists a symmetric positive definite solution $P \succ 0$ (Lyapunov matrix) to the matrix inequality*

$$\begin{pmatrix} A^T P + P A & P B & C^T \\ B^T P & -\gamma I & D^T \\ C & D & -\gamma I \end{pmatrix} \prec 0. \quad (3.1)$$

The Bounded-real lemma is widely used for \mathcal{H}_∞ optimization [8, 24, 38, 40, 43, 49, 99, 100] and forms the basis of our tuning approach.

Theorem 1 *Given the power system model (2.8) with the transfer function (2.9). Then, the following statements are equivalent:*

- $A(\mathbf{K})$ is asymptotically stable and $\|G(\mathbf{K}, s)\|_\infty < \gamma, \gamma \in \mathbb{R}$
- the following problem has a solution

$$\min_{P, \mathbf{K}, \gamma} \gamma \quad (3.2a)$$

$$\text{s.t. } M(\gamma, \mathbf{K}, P) := \begin{pmatrix} A(\mathbf{K})^T P + PA(\mathbf{K}) & PB(\mathbf{K}) & C(\mathbf{K})^T \\ B(\mathbf{K})^T P & -\gamma I & D(\mathbf{K})^T \\ C(\mathbf{K}) & D(\mathbf{K}) & -\gamma I \end{pmatrix} \prec 0 \quad (3.2b)$$

$$\underline{\mathbf{K}} \leq \mathbf{K} \leq \overline{\mathbf{K}} \quad (3.2c)$$

$$P = P^T \succ 0, \quad (3.2d)$$

where $P \in \mathbb{R}^{N_x \times N_x}$, and $\mathbf{K} \in \mathbb{R}^{N_t}$.

Proof. Using Lemma 1, we see that (3.2b) and (3.2d) are equivalent to $\|G(\mathbf{K}, s)\|_\infty < \gamma$ and the asymptotic stability of $A(\mathbf{K})$. \blacksquare

Note that weighting functions can be added to the performance output or input to focus on a specific frequency range.

Problem (3.2) is in general non-convex due to the nonlinear parameter dependency in the system matrices, and bilinear matrix products, e.g. between P and $A(\mathbf{K})$ in (3.2b) and NP-hard. We focus in the following on finding local minima of the problem.

In order to solve (3.2) with linear matrix inequality (LMI) solvers, which are more mature than bilinear matrix inequality solvers, we adapt the so called iterative coordinate descent approach, often called P-K iteration [94]. In each iteration, the Lyapunov matrix $P^{(\mu)}$ is obtained solving (3.2) with the constant controller parameter vector from the previous iteration $\mathbf{K}^{(\mu-1)}$. This leads to the following LMI optimization problem

$$\min_{P^{(\mu)}, \gamma} \gamma \quad (3.3a)$$

$$\text{s.t. } M(\gamma, \mathbf{K}^{(\mu-1)}, P^{(\mu)}) \prec 0 \quad (3.3b)$$

$$P^{(\mu)} = (P^{(\mu)})^T \succ 0. \quad (3.3c)$$

Here $M(\gamma, \mathbf{K}^{(\mu-1)}, P^{(\mu)})$ is an abbreviation for the left side of (3.2b). One obtains the Lyapunov matrix $P^{(\mu)}$ solving (3.3). Furthermore, solving (3.2) while keeping $P^{(\mu)}$ constant, one obtains $\mathbf{K}^{(\mu)}$. This problem remains non-convex due to the nonlinear parameter dependency of the matrices A, B, C and D from \mathbf{K} , implying that LMI solvers cannot be used. To do so, the system matrices are linearized in each iteration around the parameter vector from the previous iteration $\mathbf{K}^{(\mu-1)}$

$$A_L^{(\mu)}(\mathbf{K}) = A(\mathbf{K}^{(\mu-1)}) + \left. \frac{\partial A(\mathbf{K})}{\partial \mathbf{K}} \right|_{\mathbf{K}_{\mu-1}} (\mathbf{K} - \mathbf{K}^{(\mu-1)}), \quad (3.4)$$

Input: $A(\mathbf{K}), B(\mathbf{K}), C(\mathbf{K}), D(\mathbf{K}), \mathbf{K}^{(0)}$
 1 $\mu = 1$;
 2 **while** *stopping criteria not satisfied* **do**
 3 Obtain $(P^{(\mu)}, \gamma)$ as solution of (3.3);
 4 Obtain $A_L^{(\mu)}(\mathbf{K}), B_L^{(\mu)}(\mathbf{K}), C_L^{(\mu)}(\mathbf{K}), D_L^{(\mu)}(\mathbf{K})$ by linearizing $A(\mathbf{K}), B(\mathbf{K}),$
 $C(\mathbf{K}), D(\mathbf{K})$ around $\mathbf{K}^{(\mu-1)}$;
 5 $(\mathbf{K}^{(\mu)}, \gamma) =$ Solution of (3.5);
 6 $\mu \leftarrow \mu + 1$;
 7 **end**
 8 **return** $\mathbf{K}^{(\mu)}$;

Algorithm 1: Iterative descent method for solving (3.2).

and similarly for $B(\mathbf{K})$ to obtain $B_L^{(\mu)}(\mathbf{K})$, as well as $C(\mathbf{K})$ and $D(\mathbf{K})$. Based on this linearization, we solve the following convex optimization problem in each iteration

$$\min_{\mathbf{K}^{(\mu)}, \gamma} \gamma \quad (3.5a)$$

$$\text{s.t. } M_L^{(\mu)}(\gamma, \mathbf{K}^{(\mu)}, P^{(\mu)}) \prec 0 \quad (3.5b)$$

$$\underline{\mathbf{K}} \leq \mathbf{K}^{(\mu)} \leq \overline{\mathbf{K}} \quad (3.5c)$$

$$|\mathbf{K}^{(\mu)} - \mathbf{K}^{(\mu-1)}| \leq \Delta \mathbf{K}, \quad (3.5d)$$

where M_L is defined as

$$M_L(\gamma, \mathbf{K}^{(\mu)}, P^{(\mu)}) := \begin{pmatrix} A_L^{(\mu)}(\mathbf{K}^{(\mu)})^T P^{(\mu)} + P^{(\mu)} A_L^{(\mu)}(\mathbf{K}^{(\mu)}) & P^{(\mu)} B_L^{(\mu)}(\mathbf{K}^{(\mu)}) & C_L^{(\mu)}(\mathbf{K}^{(\mu)})^T \\ B_L^{(\mu)}(\mathbf{K}^{(\mu)})^T P^{(\mu)} & -\gamma I & D_L^{(\mu)}(\mathbf{K}^{(\mu)})^T \\ C_L^{(\mu)}(\mathbf{K}^{(\mu)}) & D_L^{(\mu)}(\mathbf{K}^{(\mu)}) & -\gamma I \end{pmatrix}. \quad (3.6)$$

Constraint (3.5d) is added to (3.5) to preserve the linearization accuracy by limiting how much one can move away from the linearization point in one iteration.

Algorithm 1 presents the resulting iterative algorithm denoted as the iterative coordinate descent method (ICDM). Starting variables are the linearized system matrices $A(\mathbf{K}), B(\mathbf{K}), C(\mathbf{K}), D(\mathbf{K})$, and the initial parameter vector \mathbf{K}_0 . The algorithm first solves (3.3). Then, it linearizes A, B, C and D around the parameter vector from the previous iteration $\mathbf{K}^{(\mu-1)}$, and solves (3.5). The iteration is repeated until a stopping criterion is satisfied, e.g. the number of iterations reaches the specified limit, or the improvement of the \mathcal{H}_∞ norm is smaller than the specified limit.

The outlined algorithm extends the classic P-K iteration algorithms as it considers nonlinear parameter dependency of the system matrices on the parameter vector \mathbf{K} , i.e. the A, B, C, and D matrices are nonlinear functions of the parameter vector \mathbf{K} .

The proposed method achieves good results in the considered numerical examples, as shown subsequently in Chapter 4. However, it has several drawbacks. The positive definite Lyapunov matrix \mathbf{P} is an optimization variable, thus the problem size scales quadratically with the system size. It leads to significant additional computational complexity and worsens the scaling of the optimization problem, without being used later. Basically, Problem (3.3) is solved in each iteration, without bringing any improvement of $\|G(\mathbf{K}, s)\|_\infty$. Regarding convergence, the iterative coordinate descent method, as many coordinate descent methods, does not necessarily converge to a (local) minimum, even without the linearization step.

The iterative coordinate descent method requires a stabilizing initial parameterization \mathbf{K}_0 . This can be avoided by introducing a “stabilization” step, which first determines a stabilizing parameterization \mathbf{K}_{stab} before the optimization. This can be obtained by [96]

$$\mathbf{K}_{stab} = \arg \min_{X, \mathbf{K}, \gamma, \zeta} \zeta \quad (3.7a)$$

$$\text{s.t. } A(\mathbf{K})^T X + X A(\mathbf{K}) \prec \zeta I \quad (3.7b)$$

$$P = P^T \succ 0. \quad (3.7c)$$

This problem can be solved using an analogous procedure as in Algorithm 1. The obtain parameterization \mathbf{K}_{stab} is stabilizing if and only if $\zeta \leq 0$ after optimization. Then, \mathbf{K}_{stab} can be used as the initial value for the iterative coordinate descent method. This approach is used in Chapter 7 for power system stabilization.

3.2 Controller tuning with frequency sampling

In the following we propose a tuning approach based on sampling the frequency range. The basis for the proposed method is the following theorem, see e.g. [15, 46] and references therein.

Theorem 2 (Semi-infinite \mathcal{H}_∞ constraint) *Given a detectable and asymptotically stable system $G(\mathbf{K}, s)$. The \mathcal{H}_∞ norm of $G(\mathbf{K}, s)$, i.e. $\|G(\mathbf{K}, s)\|_\infty$, is smaller than $\gamma \in \mathbb{R}_{>0}$ if and only if*

$$\begin{pmatrix} \gamma I & G(\mathbf{K}, j\omega) \\ G(\mathbf{K}, j\omega)^* & \gamma I \end{pmatrix} \succ 0, \quad \forall \omega \in \mathbb{R}_{\geq 0}. \quad (3.8)$$

Proof. Since $\bar{\sigma}(G(\mathbf{K}, j\omega))^2 = \bar{\lambda}(G(\mathbf{K}, j\omega)^*G(\mathbf{K}, j\omega))$, where $\bar{\lambda}(\cdot)$ denotes the largest singular value of a matrix, it follows

$$\|G(\mathbf{K}, j\omega)\|_\infty < \gamma \quad (3.9)$$

$$\Leftrightarrow \bar{\sigma}(G(\mathbf{K}, j\omega)) < \gamma, \quad \forall \omega \in \mathbb{R}_{\geq 0} \quad (3.10)$$

$$\Leftrightarrow \bar{\lambda}(G(\mathbf{K}, j\omega)^*G(\mathbf{K}, j\omega)) < \gamma^2, \quad \forall \omega \in \mathbb{R}_{\geq 0} \quad (3.11)$$

$$\Leftrightarrow G(\mathbf{K}, j\omega)^*G(\mathbf{K}, j\omega) - \gamma^2 I \prec 0, \quad \forall \omega \in \mathbb{R}_{\geq 0}. \quad (3.12)$$

Using the Schur complement on the last expression, one obtains (3.8). \blacksquare

For notational convenience, we drop writing the dependency on the tunable parameter vector \mathbf{K} explicitly for the rest of this section, and write only $G(s)$.

The basic idea for the second method is to use Theorem 2 for the controller tuning. However, it has two challenging properties. First, it is defined over a semi-infinite set of frequencies $\mathbb{R}_{\geq 0}$, which cannot be in general numerically handled. Second, Theorem 2 is only applicable to stable systems. It is not clear if a controller parameterization stabilizes a system only when (3.8) is satisfied. In the next sections, we propose a tuning method which considers both of these properties.

3.2.1 Semi-infinite \mathcal{H}_∞ controller tuning problem

Theorem 2 allows to formulate an alternative optimization problem for the \mathcal{H}_∞ minimization of $G(\mathbf{K}, j\omega)$

$$\min_{\gamma, \mathbf{K}} \gamma \quad (3.13a)$$

$$\text{s.t.} \quad \begin{pmatrix} \gamma I & G(\mathbf{K}, j\omega) \\ G(\mathbf{K}, j\omega)^* & \gamma I \end{pmatrix} \succ 0, \quad \forall \omega \in \mathbb{R}_{\geq 0} \quad (3.13b)$$

$$\underline{\mathbf{K}} \leq \mathbf{K} \leq \bar{\mathbf{K}}. \quad (3.13c)$$

As (3.13b) needs to be satisfied for every $\omega \in \mathbb{R}_{\geq 0}$, Problem (3.13) is semi-infinite.

Although boundedness of the system \mathcal{H}_∞ norm is a necessary and sufficient condition for system stability, a controller parameterization obtained as a solution of (3.13) does not necessarily stabilize the system. This is because Theorem 2 can be used if and only if $G(\mathbf{K}, s)$ is exponentially stable [13]. As stability of G depends on \mathbf{K} , it is possible that G becomes unstable during the optimization. To overcome this problem, one can introduce constraints which guarantee the closed-loop stability of G as a function of \mathbf{K} . Such constraints, based on frequency sampling and the Nyquist criterion, are, for example, proposed in [6, 46]. On the other hand, if the open-loop system is stable, then the boundedness of the \mathcal{H}_∞ norm of the system sensitivity matrix ensures the stability of the closed-loop system [12, 14]. Furthermore, an LMI constraint based on the Lyapunov matrix, i.e. (3.7), can also be introduced. This, however increases the number of optimization variables significantly, as the Lyapunov

matrix scales quadratically with the system size.

Thus, such approaches are not suitable for the considered purpose. Additional constraints make the optimization slower, and power systems are often not open-loop stable. Ideally, a stability certificate is needed which does not significantly increase the computational complexity of (3.13). Before introducing the stability certificate for Problem (3.13), we first review the definition of poles of MIMO functions and formulate several lemmas, as we use them subsequently.

Definition 1 (elementary poles) [63] *A complex number s_i is a pole of the transfer matrix function $G(s) : \mathbb{C} \rightarrow \mathbb{C}^{n_y \times n_w}$, when at least one element $G_{ij}(s)$ of $G(s)$ has a pole at s_i , where $G_{ij}(s)$ denotes the single-input-single-output (SISO) transfer function in the i -th row and j -th column of $G(s)$.*

Lemma 2 *Given a detectable system $G(s)$ with the finite set of poles \mathcal{S}_H . The largest singular value of $G(s)$, denoted with $\bar{\sigma}(G(s))$, approaches $+\infty$ as s approaches any pole $s_{pij} \in \mathcal{S}_H$, where s_{pij} denotes the p -th pole of the transfer function in the i -th row and j -th column of $G(s)$.*

Proof. Per definition of the singular value, we have [119]

$$\bar{\sigma}(G(s)) = \max_{\|\mathbf{z}\|_2=1} \|G(s)\mathbf{z}\|_2. \quad (3.14)$$

Thus, for all $s_{pij} \in \mathcal{S}_H$

$$\lim_{s \rightarrow s_{pij}} \bar{\sigma}(G(s)) = \lim_{s \rightarrow s_{pij}} \max_{\|\mathbf{z}\|_2=1} \|G(s)\mathbf{z}\|_2 \geq \lim_{s \rightarrow s_{pij}} \|G(s)e_j\|_2, \quad (3.15)$$

where e_j denotes a column vector where the j -th row is equal to one and all other elements are zero. The last expression can be reformulated to

$$\begin{aligned} \lim_{s \rightarrow s_{pij}} \|G(s)e_j\|_2 &= \lim_{s \rightarrow s_{pij}} \left\| \left(G_{1j}(s) \dots G_{ij}(s) \dots G_{Nj}(s) \right)^T \right\|_2 \\ &= \lim_{s \rightarrow s_{pij}} \sqrt{G_{1j}^2(s) + \dots + G_{ij}^2(s) + \dots + G_{Nj}^2(s)}, \end{aligned} \quad (3.16)$$

Since s_{pij} is a pole of $G_{ij}(s)$, it follows that $\lim_{s \rightarrow s_{pij}} G_{ij}(s)^2 = +\infty$ and that $\lim_{s \rightarrow s_{pij}} \|G(s)e_j\|_2 = +\infty$. From (3.15), it directly follows that $\lim_{s \rightarrow s_{pij}} \bar{\sigma}(G(s)) = +\infty$. ■

Assumption 1 *The coefficients of denominator polynomials in $G(\mathbf{K}, s)$ are continuous functions of the controller parameters \mathbf{K} .*

This assumption is satisfied for almost all practically relevant control elements, such as PID controllers, notch filters, lead-lag filters, washout filters etc. Thus, it does not introduce a significant restriction for the applicability of the subsequent theorems. This allows to state the following

Lemma 3 *Given the linear system $G(\mathbf{K}, s)$ that satisfies Assumption 1. The location of poles of $G(\mathbf{K}, s)$ are continuous functions of the controller parameters \mathbf{K} .*

Proof. According to Definition 1, the poles of $G(\mathbf{K}, s)$ are obtained as the roots of denominator polynomials of all elements $G_{ij}(\mathbf{K}, s)$ of $G(\mathbf{K}, s)$. The roots of a polynomial are continuous functions of the polynomial coefficients [111], whereas the denominator polynomial coefficients are continuous functions of the controller parameters (Assumption 1). It follows that poles of $G(\mathbf{K}, s)$ are continuous functions of \mathbf{K} . ■

The following assumption is necessary for the formulation of the stability certificate to Problem (3.19).

Assumption 2 *During variation of \mathbf{K} in (3.19), cancellations of poles and zeros, which depend on \mathbf{K} , of the SISO transfer functions $G_{ij}(\mathbf{K}, s)$ in $G(\mathbf{K}, s)$ do not occur on the imaginary axis.*

This assumption is mostly technical and seldom occurs for practically relevant systems. We can now formulate a stability certificate to validate that the closed-loop is stable.

Theorem 3 (Stability certificate) *Given an exponentially stabilizing parameterization \mathbf{K}_0 for a detectable system with the closed loop transfer function $G(\mathbf{K}, s)$. Under Assumption 1 and 2, with a sufficiently small step size during optimization, the solution of Problem (3.13), denoted with \mathbf{K}^* , leads to a stabilizing controller.*

Proof. We assume the opposite, i.e. that the parameterization \mathbf{K}^* results in an unstable system. This means that at least one pole s_{pij} of $G(\mathbf{K}, s)$ moved from the stable region, i.e. where $\text{Re}(s_{pij}) < 0, \forall s_{pij}$ to the unstable region, where $\exists s_{pij}, \text{Re}(s_{pij}) > 0$. Since s_{pij} is a continuous function of the controller parameters \mathbf{K} , see Lemma 3, this implies that, with a sufficiently small step size, during optimization we obtain at least one pole s_{pij} with $\text{Re}(s_{pij}) \rightarrow 0_-$. From Lemma 2, we obtain

$$\lim_{s \rightarrow s_{pij}} \lim_{\text{Re}(s_{pij}) \rightarrow 0_-} \max_{\omega \in \mathbb{R}} \bar{\sigma}(G(\mathbf{K}, j\omega)) = +\infty. \quad (3.17)$$

Consequently, when s_{pij} approaches the imaginary axis, the system \mathcal{H}_∞ norm, which is equal to $\max_{\omega \in \mathbb{R}} \bar{\sigma}(G(\mathbf{K}, j\omega))$, approaches $+\infty$. Thus, during optimization, the solver allowed the rise of the \mathcal{H}_∞ norm to very large values, depending on the step size and numerical accuracy. As the solver minimizes the system \mathcal{H}_∞ norm in each optimization step and does not allow the rise of the system norm, this leads to a contradiction. Consequently, s_{pij} will never get close enough to the imaginary axis and thus, due to the continuous dependence of s_{pij} on the controller parameters, will never cross into the unstable region. ■

Note that s_{pij} does not have to approach the imaginary axis infinitely close for the \mathcal{H}_∞ norm to increase to large values. When the poles are close enough, such that the maximum of $\bar{\sigma}(G(j\omega))$ is achieved in the frequency range around s_{pij} , the \mathcal{H}_∞

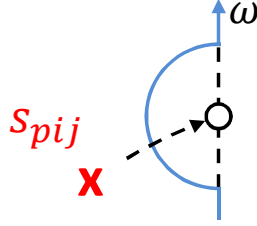


Figure 3.1: Modification of the imaginary axis, shown in blue, to prevent a pole zero cancellation on the imaginary axis.

norm minimization will lead to \mathbf{K} parameters that prevent s_{pij} to approach further the imaginary axis.

It is possible that a change of controller parameters causes a pole-zero cancellation (in one transfer function G_{ij}) in the region around the imaginary axis. We first consider the case when this happens in a point $\sigma_1 + j\omega_1$, $\sigma_1 < 0$. Then, given a sufficiently small step size, due to the continuity of system poles, there exists $\sigma_2 < 0$, $\sigma_2 \neq \sigma_1$, such that the system pole shifts to $\sigma_2 + j\omega_2$. If the system zero does not shift to the same point, causing another pole-zero cancellation, the largest singular value of $G(\mathbf{K}, s)$ will approach $+\infty$ in the environment of $\sigma_2 + j\omega_2$, and will not cross the imaginary axis. In the second case, we consider that the pole-zero cancellation occurs on the imaginary axis, on the point $j\omega_3$, contrary to Assumption 2. Consequently, the \mathcal{H}_∞ norm of the system in $j\omega_3$, and in its vicinity, will remain bounded. Thus, in this case it is possible that the system becomes unstable during the optimization, depending on the value of $\bar{\sigma}(G(\mathbf{K}, j\omega))$ in other frequencies, which is excluded by Assumption 2. This assumption can be avoided by introducing an additional step in the optimization. If a pole zero cancellation occurs on the imaginary axis, the optimization is repeated, but $\bar{\sigma}(G(s))$ is evaluated on a modified imaginary axis line, as shown in blue Fig. 3.1. In this way, the rise of $\bar{\sigma}(G(s))$ is captured before the cancellation occurs and thus the pole is kept away from the imaginary axis.

A direct consequence of the theorem is that Problem (3.13) cannot stabilize an unstable system, given Assumption 2; if the initial parameterization \mathbf{K}_0 is unstable, Problem (3.13) will not allow unstable system poles to cross the imaginary axis to the stable region. Note that the requirement for an initially stabilizing controller is in accordance to the results presented in [6, 46]. In comparison to [14], the stability guarantee in Theorem 3 is applicable to systems which are open-loop unstable.

To clarify the claim of Theorem 3, we consider the small example system

$$G'(s) = \begin{pmatrix} \frac{s+2}{(s+1)(s+3)} & \frac{s-3}{s^2+3s+3} \\ \frac{s^2+4s+10}{(s+3)(s^2+s+1)} & \frac{s+4}{(s+1)(s+2)} \end{pmatrix}. \quad (3.18)$$

This system has the pole set $\tilde{\mathcal{S}} = \{-1, -2, -3, -1.5 \pm j0.87, -0.5 \pm j0.87\}$, where the poles $s = -1$, and $s = -2$ have a multiplicity of 2. Figure 3.2 shows the largest

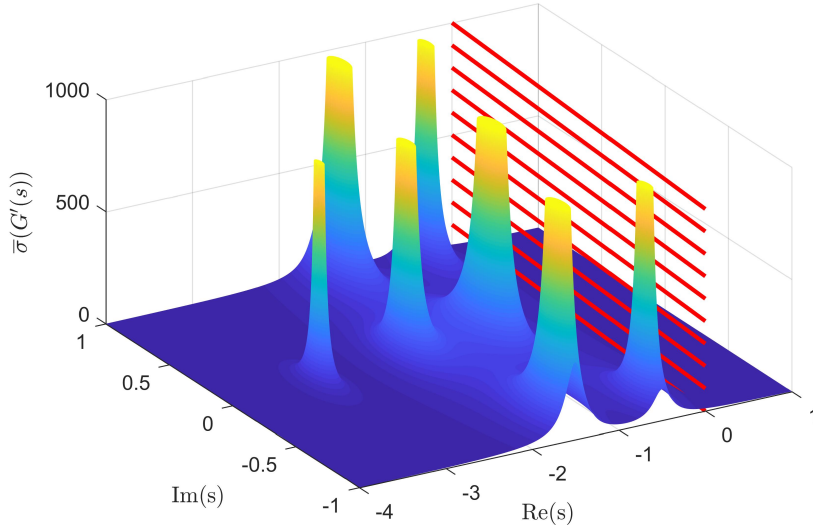


Figure 3.2: Graphical representation of $\bar{\sigma}(G'(s))$; $\bar{\sigma}(G'(s))$ approaches infinity in the surrounding of any $s_{pij} \in \tilde{\mathcal{S}}$. Red lines mark the imaginary axis, along which the system \mathcal{H}_∞ norm is minimized.

singular value of $\tilde{G}(s)$. It confirms that the system singular values approach infinity as s approaches one of the system poles, see Lemma 2. We minimize the \mathcal{H}_∞ norm of the system by minimizing the largest singular value of G' on the imaginary axis, i.e. $\bar{\sigma}(G'(j\omega))$. The plane with $\text{Re}(s) = 0$, along which $\bar{\sigma}(G'(j\omega))$ is minimized, is represented with red lines in Fig. 3.2. If the poles approach the imaginary axis, $\max_{\omega \in \mathbb{R}} \|\bar{\sigma}(G'(j\omega))\|_\infty$ rises to large values. Since the \mathcal{H}_∞ norm is minimized in every optimization step, the minimization of the \mathcal{H}_∞ norm will never lead to the system poles reaching, and crossing, the imaginary axis.

3.2.2 Finite \mathcal{H}_∞ controller tuning problem

Since (3.13) is semi-infinite, we use a finite-dimensional approximation to numerically solve it. One way to find an approximation is to use a finite, but large enough, number of frequency samples at which constraint (3.13b) is evaluated, i.e. to solve the following problem

$$\min_{\gamma, \mathbf{K}} \gamma \quad (3.19a)$$

$$\text{s.t. } \Phi(G(\mathbf{K}, j\omega_k), \gamma) := \begin{pmatrix} \gamma I & G(\mathbf{K}, j\omega_k) \\ G(\mathbf{K}, j\omega_k)^* & \gamma I \end{pmatrix} \succ 0, \quad \forall \omega_k \in \Omega \quad (3.19b)$$

$$\underline{\mathbf{K}} \leq \mathbf{K} \leq \bar{\mathbf{K}}. \quad (3.19c)$$

Here Ω is the discrete set of sampled frequencies with N_ω elements. Since the problem scales linearly with N_ω , a reasonably large number of elements in Ω can be chosen such

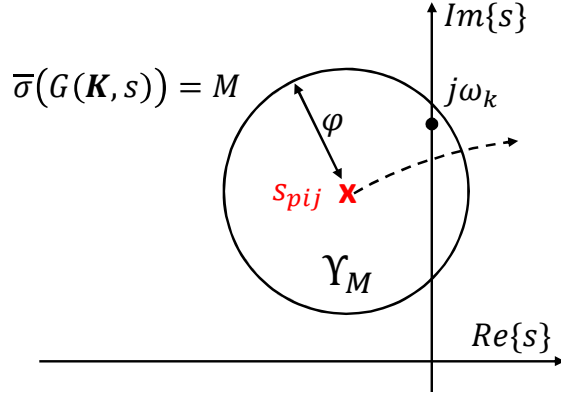


Figure 3.3: Illustration of the proof of Theorem 4. As s_{pij} approaches the imaginary axis, $\min_{j\omega \in \Upsilon_M} \bar{\sigma}(G(\mathbf{K}, j\omega))$ increases. If there exists $\omega_k \in \Omega$, such that $j\omega_k \in \Upsilon_M$, this rise is visible for the sampled frequencies as well.

that it covers the required frequency range with satisfactory density [14]. Note that the choice for Ω is problem specific and needs to be adapted to the considered frequency range. With a sufficiently large number of samples in Ω , the local optimum of (3.19) can be arbitrarily close to the optimum of (3.13). Additionally, only frequencies in the relevant frequency range need to be in Ω . In power systems, e.g., this range is normally up to 10 Hz.

With the following theorem, we extend the stability certificate from Theorem 3 to discrete sampling.

Theorem 4 (Stability-certificate for discrete sampling) *Given an exponentially stabilizing parameterization \mathbf{K}_0 for the detectable system with the transfer function $G(\mathbf{K}, s)$. Under Assumption 1 and 2, with a sufficiently small step size during optimization and sufficiently dense sampling in Ω , the solution of Problem (3.19), denoted with \mathbf{K}' , leads to a stabilizing controller.*

Proof. The proof is similar as for Theorem 3. We outline the proof for the case when one pole (pair) approaches the imaginary axis. The proof with multiple pole pairs approaching the imaginary axis can be obtained analogously. We show that there exists a sufficiently dense discrete sampling, such that $\|G(\mathbf{K}, s)\|_\infty$ reaches arbitrarily large values when a pole approaches the imaginary axis. For the proof, we assume the opposite, i.e. that the parameterization \mathbf{K}' results in an unstable system. This means that at least one pole s_{pij} of $G(\mathbf{K}', s)$ moved from the stable region, i.e. where $\text{Re}(s_{pij}) < 0, \forall s_{pij}$ to the unstable region, where $\exists s_{pij}, \text{Re}(s_{pij}) > 0$. As shown in Lemma 2, $\bar{\sigma}(G(\mathbf{K}, s^*))$ approaches $+\infty$ as s_{pij} approaches s^* . Since $\bar{\sigma}(G(\mathbf{K}, s))$ is a continuous function of s [22], it follows that for arbitrary $M \in \mathbb{R}$, there exists a non-empty environment of s_{pij} where $\bar{\sigma}(G(\mathbf{K}, j\omega))$ is greater than M , i.e.

$$\forall M \in \mathbb{R}, \exists \varphi \in \mathbb{R}, \text{ s.t. } |s - s_{pij}| \leq \varphi \Rightarrow \bar{\sigma}(G(\mathbf{K}, s)) \geq M. \quad (3.20)$$

As s_{pij} approaches the imaginary axis, the intersection of the set $\Upsilon_M = \{s : |s - s_{pij}| \leq \varphi, \bar{\sigma}(G(\mathbf{K}, s)) \geq M\}$ with the imaginary axis becomes non-empty, as illustrated in Fig. 3.3. Thereby $\min_{j\omega \in \Upsilon_M} \bar{\sigma}(G(\mathbf{K}, j\omega))$ increases, as s_{pij} approaches the imaginary axis. Since s_{pij} is a continuous function of \mathbf{K} , c.f. Lemma 3, under the assumption of sufficiently small step size, it follows that there must exist a parameterization $\mathbf{K}^{(\mu)}$ in the μ -th step, for which there exists an $M^*(\mathbf{K}^{(\mu)})$ and Υ_{M^*} such that $\bar{\sigma}(G(\mathbf{K}^{(\mu)}, j\omega))$ for any element of Υ_{M^*} is greater than $\bar{\sigma}(G(\mathbf{K}^{(\mu)}, j\omega))$ for any other $j\omega$ outside Υ_{M^*} . Additionally, with this parameterization, $\|G(\mathbf{K}^{(\mu)})\|_\infty$ increased compared to $\|G(\mathbf{K}^{(\mu-1)})\|_\infty$, i.e.

$$\min_{j\omega \in \Upsilon_{M^*}} \bar{\sigma}(G(\mathbf{K}^{(\mu)}, j\omega)) > \max_{j\omega \in j\mathbb{R}_{\geq 0} \setminus \Upsilon_{M^*}} \bar{\sigma}(G(\mathbf{K}^{(\mu)}, j\omega)) \quad (3.21)$$

$$\min_{j\omega \in \Upsilon_{M^*}} \bar{\sigma}(G(\mathbf{K}^{(\mu)}, j\omega)) > \max_{\omega \in \mathbb{R}_{\geq 0}} \bar{\sigma}(G(\mathbf{K}^{(\mu-1)}, j\omega)). \quad (3.22)$$

Under the assumption of sufficient sampling, there exists $\omega_k \in \Omega$, such that ω_k belongs to Υ_{M^*} . Consequently, we have

$$\exists \omega_k \in \Omega, \text{ s.t. } \bar{\sigma}(G(\mathbf{K}^{(\mu)}, j\omega_k)) > \max_{j\omega \in j\mathbb{R}_{\geq 0} \setminus \Upsilon_{M^*}} \bar{\sigma}(G(\mathbf{K}^{(\mu)}, j\omega)) \quad (3.23)$$

$$\exists \omega_k \in \Omega, \text{ s.t. } \bar{\sigma}(G(\mathbf{K}^{(\mu)}, j\omega_k)) > \max_{\omega \in \mathbb{R}_{\geq 0}} \bar{\sigma}(G(\mathbf{K}^{(\mu-1)}, j\omega)). \quad (3.24)$$

Thus, during optimization, the solver allowed the rise of the \mathcal{H}_∞ norm from the $(\mu - 1)$ -th step to the (μ) -th step. As the solver minimizes the system \mathcal{H}_∞ norm in each optimization step and does not allow the rise of the system norm, this leads to a contradiction. Consequently, s_{pij} will never get close enough to the imaginary axis and thus, due to the continuous dependence of s_{pij} on the controller parameters, will never cross into the unstable region. ■

Note that sufficiently fine sampling for stability does not require infinitely small sampling. Instead, there needs to be at least one frequency sample in the set Υ_{M^*} for all poles that eventually cross the imaginary axis, i.e. the density of the frequency grid in the crossover range needs to be satisfy

$$\omega_k - \omega_{k-1} < \max_{j\omega \in \Upsilon_{M^*}} \omega - \min_{j\omega \in \Upsilon_{M^*}} \omega \quad (3.25)$$

to always guarantee stability of G . This ensures that the rise of $\|G(\mathbf{K}, s)\|_\infty$ is captured with the discretization, and does not allow a pole to cross the imaginary axis. When solving (3.19), if an unstable parameterization is obtained, the density of the frequency grid can be increased around the crossover frequency and the optimization can be repeated.

Remark 2 *Constraint (3.19b) can also be used in other optimization problems to guarantee system stability. By setting γ in (3.19b) to a relatively large, but finite,*

value, this constraint will not allow $\|G(\mathbf{K}, s)\|_\infty$ to rise above γ , thus preventing system poles to cross to the unstable region.

3.2.3 Solution algorithm

Problem (3.19) is non-convex due to the nonlinear dependency on the controller parameters in $G(\mathbf{K}, s)$. In order to solve it with convex solvers, we transform the problem into a series of convex optimization problems by linearizing the parameter dependency of $G(\mathbf{K}, s)$. To obtain the linearized transfer matrix in the k -th iteration $G_L^{(k)}(\mathbf{K}, s)$, we linearize the parametric dependency of $G(\mathbf{K}, s)$ around the parameter vector obtained in the previous iteration $\mathbf{K}^{(k-1)}$. The following optimization problem is then solved in each iteration

$$\mathbf{K}^{(k)} = \arg \min_{\gamma, \mathbf{K}} \quad \gamma \quad (3.26a)$$

$$\text{s.t.} \quad \Phi(G_L^{(k)}(\mathbf{K}, j\omega_k), \gamma) \succ 0, \forall \omega_k \in \Omega \quad (3.26b)$$

$$\underline{\mathbf{K}} \leq \mathbf{K} \leq \overline{\mathbf{K}} \quad (3.26c)$$

$$|\mathbf{K} - \mathbf{K}^{(k-1)}| \leq \Delta \mathbf{K}, \quad (3.26d)$$

where Φ is defined in (3.19), and we define the absolute value element-wise for vectors. Compared to (3.19), this problem has an additional constraint, (3.26d), which has two purposes in the optimization algorithm. First, it defines a trust region in which the linearization accuracy of $G_L^{(k)}$ is preserved. Second, by reducing $\Delta \mathbf{K}$, it can be used to reduce the step size if we obtain an unstable system during optimization, so that the system poles cannot “jump” over the imaginary axis between the iterations.

The resulting iterative convex optimization algorithm is outlined in Algorithm 2. The algorithm takes as input a stabilizing initial parameterization \mathbf{K}_0 . In each iteration $G(\mathbf{K}, s)$ is first linearized around the parameter vector from the previous iteration, i.e. $\mathbf{K}^{(k-1)}$, and $G_L^{(k)}(\mathbf{K}, s)$ is obtained. Then, $G_L^{(k)}(\mathbf{K}, s)$ is used to solve (3.26) and obtain $\mathbf{K}^{(k)}$. However, if the linearization accuracy is not sufficient, or if the step size is too big, $\|G(\mathbf{K}^{(k)}, s)\|_\infty$ might increase, or $G(\mathbf{K}^{(k)}, s)$ might even be unstable. If this occurs, in Step 6, $\Delta \mathbf{K}$ is multiplied with $\alpha < 1$, e.g. $\alpha = 0.9$ to increase the linearization accuracy. If this measure does not help, then the density of the frequency grid needs to be increased and the algorithm should be started again. By choosing $\Delta \mathbf{K}$ small enough and with sufficient sampling, Theorem 4 guarantees that a stabilizing controller is obtained. Convergence to a local optimum of the finite optimization problem is guaranteed if the initial value is close enough to the (locally) optimal value [78].

The advantages of (3.19), compared to the approach based on the Bounded-Real Lemma from Section 3.1, with respect to scalability, are severalfold. Problem (3.2) introduces a positive-definite (Lyapunov) matrix \mathbf{P} as an optimization variable, which has the same size as the number of states of the closed loop system, causing the number

Input: $G, \mathbf{K}_0, \Delta\mathbf{K}, k_{max}$

```

1  $k = 1$ , choose  $0 < \alpha < 1$ ;
2 while  $k \leq k_{max}$  or not converged do
3    $G_L^{(k)}(\mathbf{K}, s)$  = linearization of the parametric dependency of  $G(\mathbf{K}, s)$  around
    $\mathbf{K}^{(k-1)}$ ;
4    $\mathbf{K}^{(k)}$  = solution of (3.26);
5   if  $\|G(\mathbf{K}^{(k)}, s)\|_\infty \geq \|G(\mathbf{K}^{(k-1)}, s)\|_\infty$  or  $G(\mathbf{K}^{(k)}, s)$  is unstable then
6      $\Delta\mathbf{K} = \Delta\mathbf{K} \times \alpha$ ;
7      $\mathbf{K}^{(k)} = \mathbf{K}^{(k-1)}$ ;
8   end
9    $k = k + 1$ 
10 end
11 return  $\mathbf{K}^{(k)}$ 

```

Algorithm 2: Proposed iterative frequency-sampling optimization algorithm.

of optimization variables to increase quadratically with the number of states in the closed-loop system. Additionally, the size of the matrix in (3.2b) increases in size with the number of states, as well as inputs and outputs of the system. On the other hand, Problem (3.19) does not have the Lyapunov matrix P as an optimization variable, and the size of the problem only depends on the number of inputs and outputs of the system, and on the size of the chosen frequency grid, making the controller synthesis generally faster.

Example. We consider a system with 20 states, 2 controller parameters, 2 disturbance inputs and 2 performance outputs as a small example to demonstrate the computational complexity. For this example, Problem (3.2) has, in addition to the 2 controller parameters, a total of 210 optimization variables for the Lyapunov matrix, and two definiteness constraints on matrices with the sizes 20×20 and 24×24 . On the other hand, (3.19), has only 2 optimization variables, and LMI constraints for a matrix with the size 4×4 , repeated for a frequency grid. Hence, if appropriate frequency grids are chosen, (3.19) achieves a much better computation time than (3.2).

3.3 Frequency weighting in the optimization problem

Before the \mathcal{H}_∞ optimization, the transfer function $G(s)$ often needs to be weighted in relevant frequency areas to achieve satisfying performance. This is usually done by multiplying the output with weighting functions representing low-pass, high-pass, or band-pass filters. This type of weighting can be done for both presented approaches as well. However, it increases the number of states in the system, thus increasing the computational complexity, and often worsens the conditioning of the system.

Problem (3.19) allows for a simpler weighting scheme. If, for example, optimization

in a frequency band is desired, it would usually require the introduction of a band-pass filter. However, with (3.19), a bandpass filter can be avoided by simply defining the frequency grid only on the desired interval. Other weighting schemes can also be easily considered in the problem formulation, without increasing the computational complexity of the optimization. To do this, we introduce the scalar scaling factor $\beta_s(\omega)$ such that

$$G_s(\mathbf{K}, j\omega) := G(\mathbf{K}, j\omega) \times \frac{1}{\beta_s(\omega)}, \quad (3.27)$$

which can be used for arbitrary scaling schemes of $\bar{\sigma}(G(\mathbf{K}, j\omega))$, as $\bar{\sigma}(G(\mathbf{K}, j\omega)) = \beta_s(\omega)\bar{\sigma}(G_s(\mathbf{K}, j\omega))$. After analogous reformulations as in Theorem 2, the following weighted optimization problem is obtained

$$\min_{\gamma, \mathbf{K}} \gamma \quad (3.28a)$$

$$\text{s.t.} \quad \begin{pmatrix} \gamma\beta_s(\omega_k) \times I & G(\mathbf{K}, j\omega_k) \\ G(\mathbf{K}, j\omega_k)^* & \gamma\beta_s(\omega_k) \times I \end{pmatrix} \succ 0, \quad \forall \omega_k \in \Omega \quad (3.28b)$$

$$\underline{\mathbf{K}} \leq \mathbf{K} \leq \bar{\mathbf{K}}. \quad (3.28c)$$

Here, $\beta_s(\omega_k)$ can take arbitrary nonzero values. This weighting scheme has several advantages compared to introducing weighting functions. First, it does not increase the computational burden of (3.28). Second, $\beta_s(\omega)$ can be easily specified, without special considerations about the properties of different filter types. Lastly, the specified weighting does not have to be a causal transfer function; a function with derivative behavior in the frequency-domain can easily be specified. A different way to interpret the proposed weighting scheme is that γ , and thus the cost function, is made frequency dependent.

3.4 Summary

We introduced two methods for structured \mathcal{H}_∞ controller synthesis in linear systems which consider nonlinear parameter dependencies. The first method, derived from the Bounded Real Lemma, adapts the so-called P-K iteration to nonlinear parameter dependencies in the system matrices. The second method uses frequency sampling to solve the synthesis problem by directly applying the definition of the \mathcal{H}_∞ norm. Thereby, guarantees are provided for both algorithms that the obtained controller parameterization stabilizes the system as well, in addition to minimizing the system \mathcal{H}_∞ norm. Finally, a weighting scheme for the second method is introduced, which is easier to implement than conventional methods using weighting functions, does not increase the computation time, and which does not need to represent a causal transfer function.

4 Numerical evaluation

In this chapter, we evaluate the proposed methods for structured \mathcal{H}_∞ controller tuning considering several simulation examples. The time-domain response, as well as the singular value plot of the considered systems before and after the optimization are compared. For the optimization, we use the Matlab toolbox YALMIP [61], together with the LMI solver SeDuMi [109]. The results are validated using nonlinear simulations with Simscape Power Systems and PSS[®]Netomac, to estimate the practical impact.

4.1 IEEE 39 bus system

The first example is a dynamic model of the IEEE 39 bus, and 10 power plant system, which is adopted from [77]. The topology of the power system is shown in Fig. 4.1. It consists of 10 power plants, for details see Appendix C.1. Static prosumers in the system are denoted with arrows, c.f. Fig. 4.1. We consider the active powers of constant-power elements in buses 2, 4, 9, 21, 23, 26, 29 as disturbance inputs, marked with blue. All prosumer and grid parameters are taken from [77]. We increased the exciter gains from 200 to 600 to obtain a stable system. The overall linear system consists of 190 states and 100 tunable controller parameters.

Figure 4.2 shows the time-response of the system to a step-wise 100 MW load increase in bus 21. The response of the linearized system is shown with dashed lines, whereas the nonlinear simulation of the generator frequencies is shown with solid lines. The nonlinear simulation is performed in Simscape Power Systems [68] with nonlinear models of the power plants and the nonlinear power flow equations. The difference between the linear and nonlinear responses in Fig. 4.2 is small, meaning that the linear model can be accurately used for the parameter tuning. In the model, \mathcal{P}_{10} emulates a connected power system, which consists of multiple other power plants. For this reason, \mathcal{P}_{10} has a much larger inertia than the other power plants in the considered system. As the inertia of a power plant has a large impact on the power system dynamics, especially on the frequency dynamics, the behavior of \mathcal{P}_{10} in the time response in Fig. 4.2 is different than the response of the other power plants. The resulting oscillations with the initial parameterization are poorly damped and do not settle after 10 seconds. Additionally, an approximately 70% overshoot is present in the system. We define the overshoot of a signal as the relation between the maximal deviation of

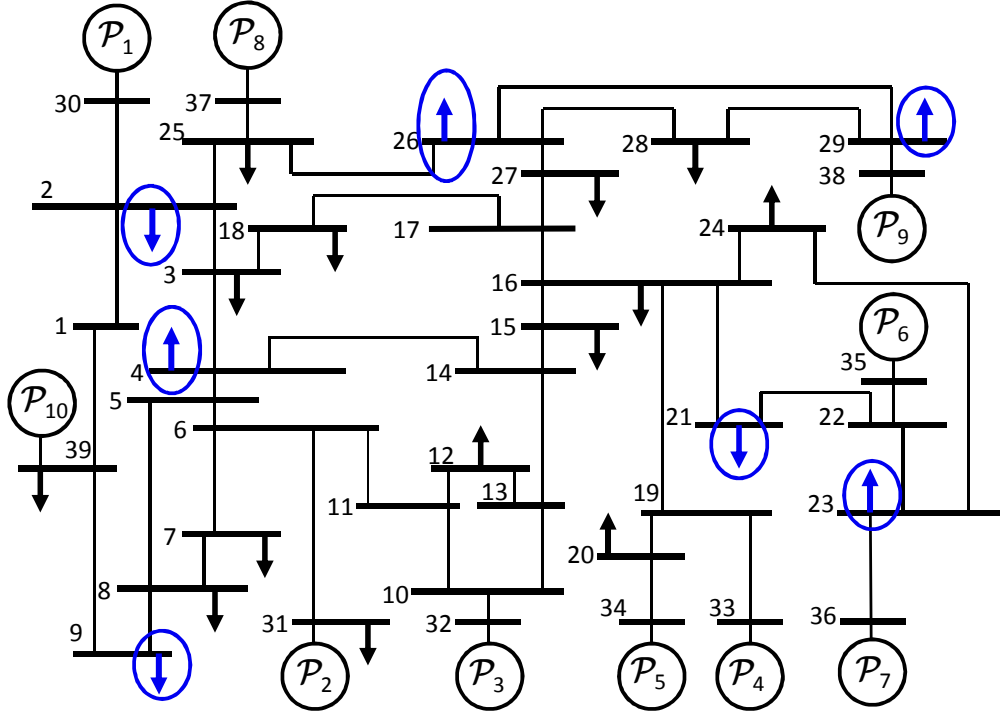


Figure 4.1: The IEEE 39 bus system with 10 power plant prosumers. Blue arrows denote the disturbances w_i .

the signal from the steady-state value and the steady-state value itself, i.e.

$$\%OS = \frac{|y_{max}| - |y_{ss}|}{|y_{ss}|} \times 100\%, \quad (4.1)$$

where y_{max} is the maximal absolute value of the signal, and y_{ss} is the steady-state value after the step disturbance. The oscillations are also visible in the frequency domain in the singular value plot in Fig. 4.4 for the initial parameterization, which shows the resonant peaks causing the oscillations.

To improve the system step response, we apply the proposed approaches on this system. Thereby, both approaches achieve the same result, c.f. Fig. 4.3. The overshoot is reduced to approximately 30%, and the oscillations settle within approximately 4 seconds. Simulation with the optimized parameters of the linear model (dashed lines) again shows good correspondence to the detailed nonlinear simulation (solid lines). The singular value plot of the system, presented in Fig. 4.4, shows that the resonant peaks were practically eliminated after the parameter optimization. The structured controller synthesis reduced the \mathcal{H}_∞ norm by a factor of 10. Thus, the optimally tuned parameters reject disturbances significantly better than in the untuned case.

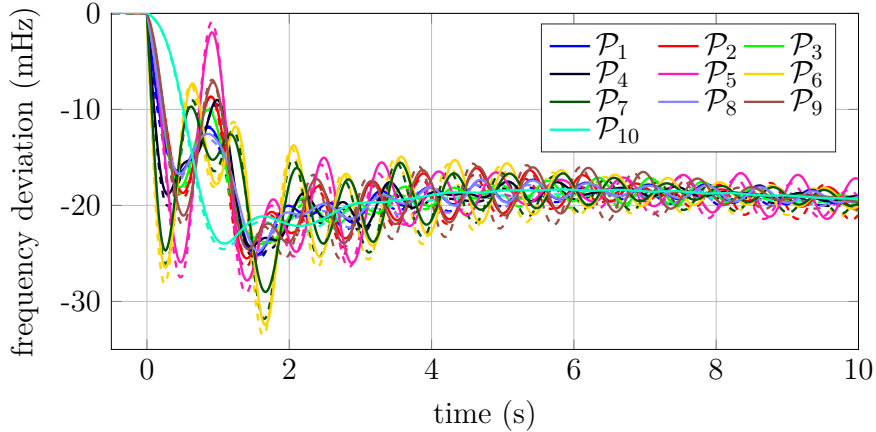


Figure 4.2: Time-domain response of power plant frequencies in the IEEE 39 bus system after a 100 MW load step in bus 21 with initial parameters. Solid lines represent simulations with the nonlinear model, whereas dashed lines represent simulations with the linear model.

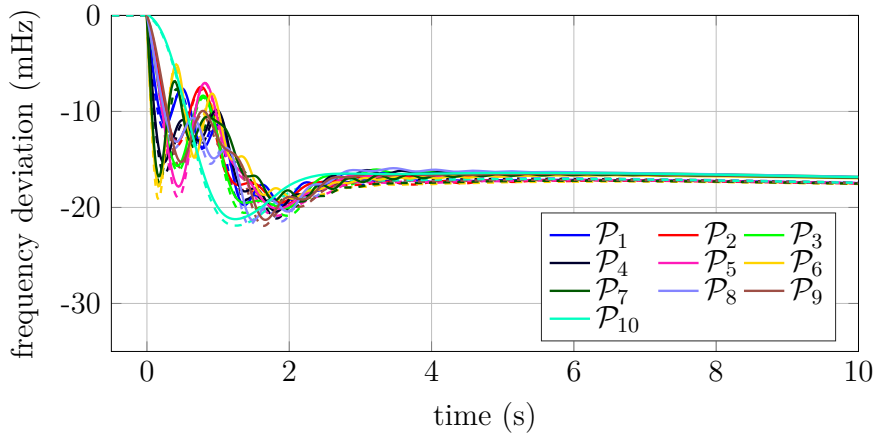


Figure 4.3: Time-domain response of power plant frequencies in the IEEE 39 bus system after a 100 MW load step in bus 21 with tuned parameters. Solid lines represent simulations with the nonlinear model, whereas dashed lines represent simulations with the linear model.

4.2 AC/DC integration

New components in power systems, such as flexible AC transmission system elements (FACTS) and high voltage direct current (HVDC) lines with AC/DC converters, allow for new degrees of freedom in power system control. We focus in this section on power oscillation damping with HVDC lines, which has been an interesting research topic in recent years [81, 84, 85, 113]. We improve the power oscillation damping in an exemplary AC-DC system by tuning parameters of local controllers. Additionally, we show the possibility for oscillation damping using only local control of HVDC systems.

For this purpose, we modify the IEEE 39 bus system, considered in Section 4.1 by adding a HVDC line between randomly selected buses 16 and 27, as depicted in Fig. 4.5.

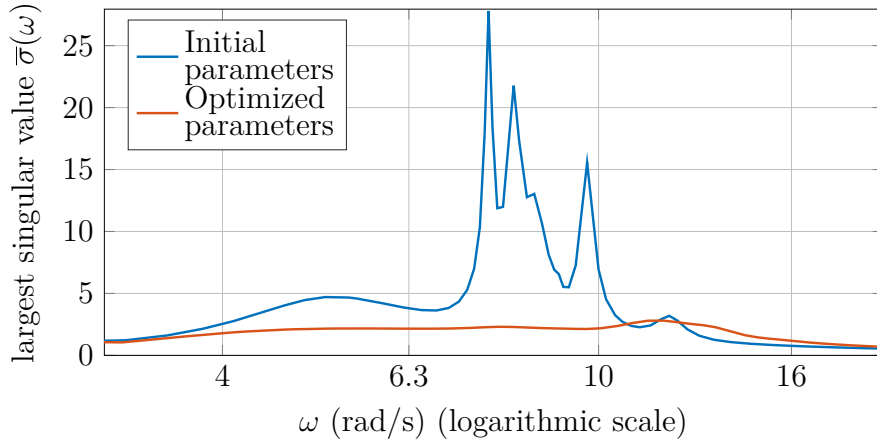


Figure 4.4: Largest singular value of the linearized IEEE 39 bus power system as a function of the input frequency ω . After optimization, most of the resonant peaks in the system are eliminated.

Thereby, converter \mathcal{C}_1 controls its DC-voltage and is connected to bus 27, whereas converter \mathcal{C}_2 is connected to bus 16 and controls its active power. Both converters also control their reactive power infeeds. For further details see Appendix C.2. For the optimization, we consider as performance inputs the active power of loads in the same buses as in Section 4.1, marked blue in Fig. 4.5. The modeling of coupled AC/DC systems is shown in Appendix B, whereas the parameters of the considered system are shown in Appendix C.2.

With this setup, nonlinear simulation in Simscape Power Systems [68] of the frequency response of the 10 power plants \mathcal{P}_i after a 100 MW load step in bus 26 is shown in Fig. 4.6(a). Strong oscillations are present in the system, which do not settle after 30 s, and the response has an overshoot of approximately 50%.

To eliminate these oscillations, we first tune all power plant and HVDC converter controller parameters. Figure 4.6(b) shows the frequency response with optimized parameters. By tuning the power plant controller parameters, power oscillations can practically be eliminated. The oscillations settle in approx. 3 seconds and the overshoot is reduced to 17%. For the next evaluation, we consider that only the HVDC controller parameters can be tuned. All power plant parameters are set to their initial values. As shown in Fig. 4.6(c), oscillations in the system are better damped with the optimized parameters, compared to Fig. 4.6(a). Nonetheless, much better damping is achieved when all power plant controllers are tuned as well. For the same setup, Fig. 4.7 shows the system frequency response with initial and optimized parameters after a load step in bus 29, showing similar improvement as for the previous load step.

This numerical evaluation demonstrates that HVDC lines can improve oscillation damping in the system even though they do not store any energy, and only use local measurements. This can be intuitively explained by the fact that \mathcal{P}_5 oscillates the most for any load step, and the HVDC control is tuned to damp the oscillations of \mathcal{P}_5 .

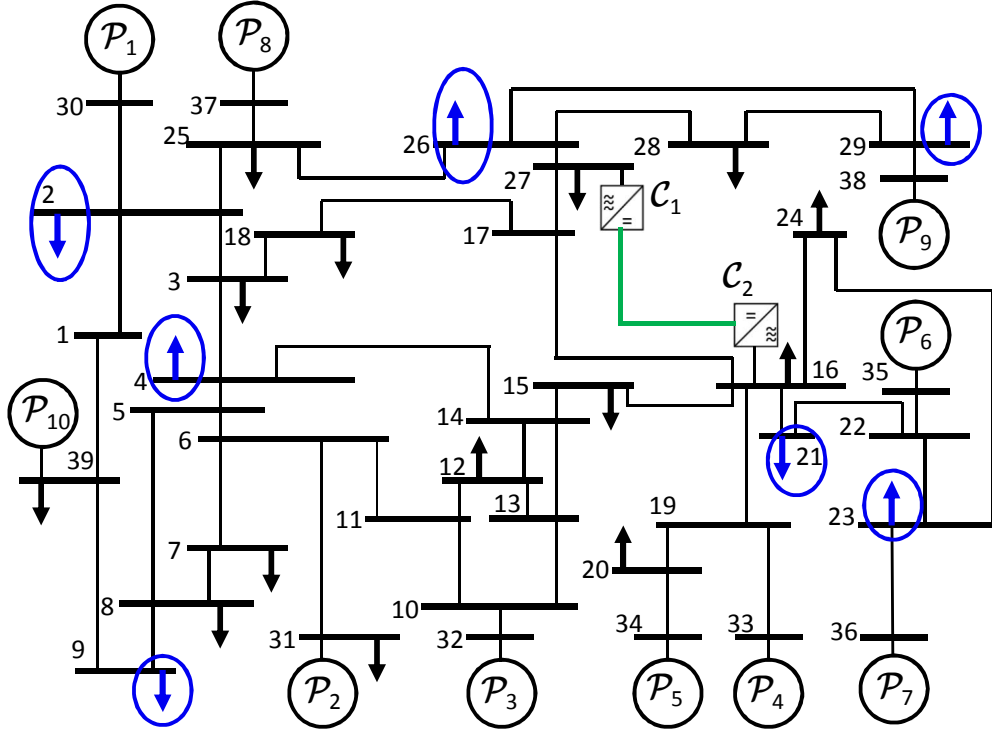


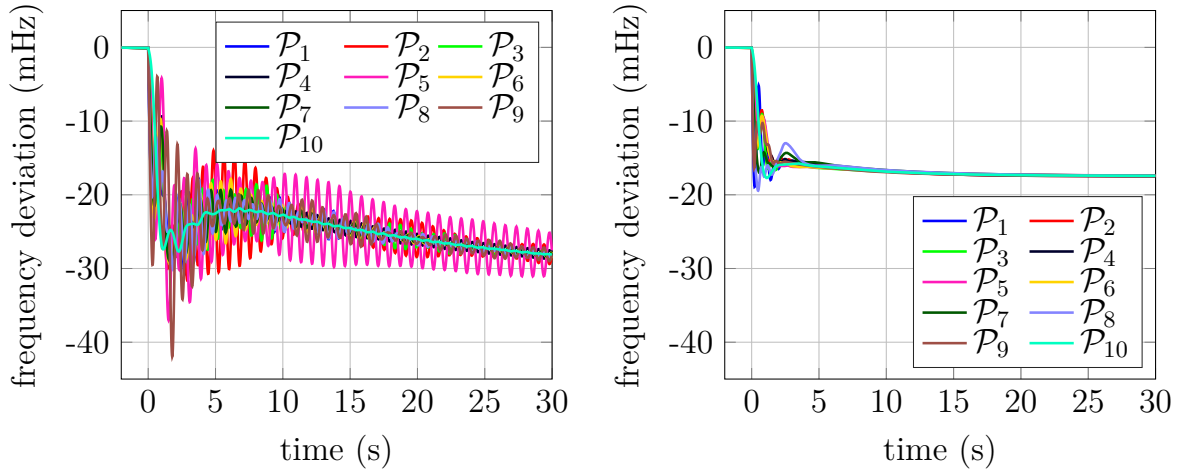
Figure 4.5: Modified IEEE 10 generator 39 bus system. An HVDC power line is added between buses 16 and 27.

Additionally, even though the HVDC line covers a small part of the grid, it can still make a visible contribution to oscillation damping in the system.

4.3 European 53 power plant system

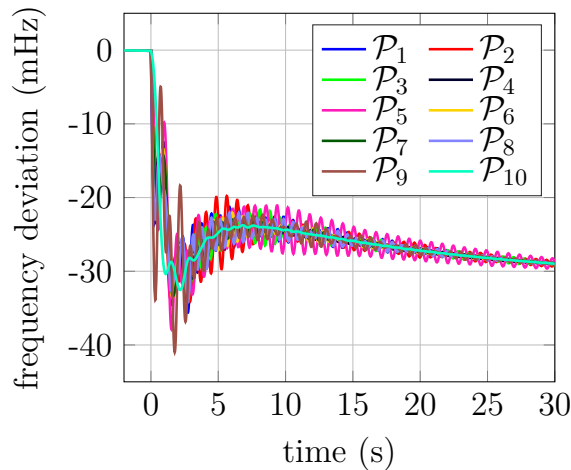
We apply the parameter tuning methods on a model with 53 power plants. It represents a reduced version of the European power system, developed as a part of the research project DynaGridCenter [27]. An overview of the power system structure is shown in Fig. 4.8. The grid consists of 35 buses (nodes), connected by long power transmission lines. Two power plants are attached to most buses (nodes) in the system, and each node has static prosumers which emulate loads and renewable generation. The controllers used for this model are presented in Appendix C.3. A more detailed description of the considered system is avoided as it is not necessary for the understanding of the presented results. Nineteen power plants in the system have tunable controllers, whereas all other power plants have a constant exciter voltage $E_{fd,i}$ and turbine mechanical power $P_{m,i}$. Thus, this system represents a good example for a brown-field application, where only some prosumers (power plants) have tunable controllers. The described power system has a total of 469 states and 116 tunable controller parameters. We consider the active power of static prosumers in 15 buses as disturbance inputs, marked with blue in Fig. 4.8.

Figure 4.9(a) shows the frequency response at ten nodes in the system with initial



(a) Initial parameters.

(b) Power plant and HVDC controllers optimized.

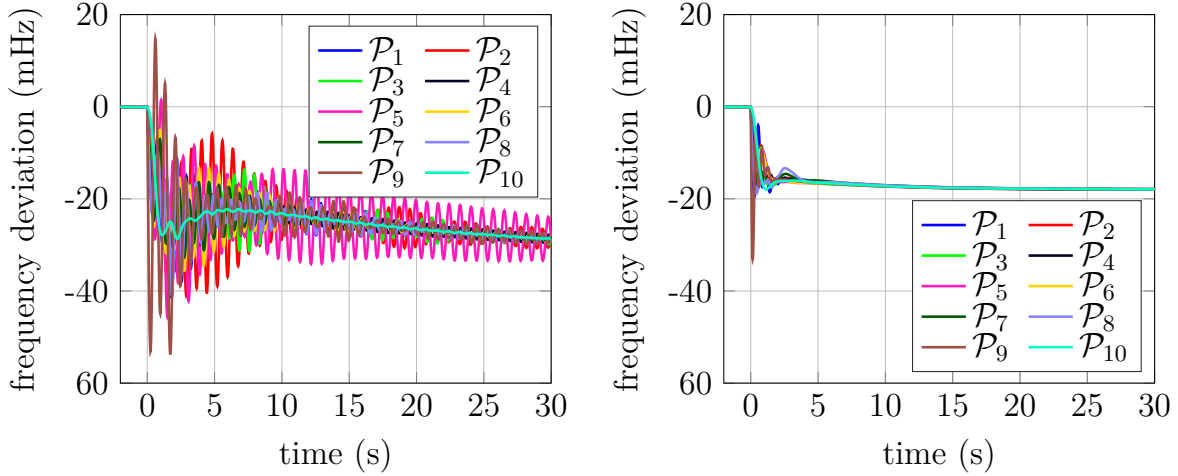


(c) Only HVDC controller parameters optimized.

Figure 4.6: Nonlinear simulation of the generator frequency response after a 100 MW load step in bus 26 in Fig. 4.5 with (a) initial parameters, (b) optimized power plant and HVDC converter parameters, and (c) only optimized HVDC converter parameters.

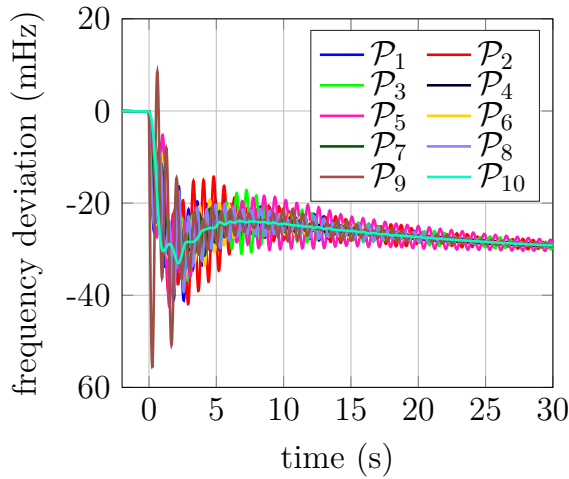
system parameters after a 1.5 GW generation dropout in bus 1. The simulation is done with nonlinear power plant and power grid models in the commercial power system simulation software PSS[®]Netomac. As shown in Fig. 4.9(a), poorly damped oscillations are present in the system. They do not settle within 200 seconds, and the initial overshoot is approx. 210% compared to the steady-state deviation. The initial parameters were obtained manually with iterative simulation in a time-consuming process. Due to the system complexity and time limitations, we did not find a better parameterization manually. The proposed tuning algorithm provides a systematic way to tune the parameters of such complex systems.

Figure 4.9(b) shows the frequency response after the application of the frequency-



(a) Initial parameters.

(b) Power plant and HVDC controller parameters optimized.



(c) Only HVDC controller parameters optimized.

Figure 4.7: Nonlinear simulation of the generator frequency response after a 100 MW load step in bus 29 in Fig. 4.5 with (a) initial parameters, (b) optimized power plant and HVDC converter parameters, and (c) only optimized HVDC converter parameters.

sampling based tuning algorithm. An additional constraint was added in the optimization in order to achieve the same steady-state deviation as with the initial parameterization. It shows a reduction in the overshoot to approx 160% compared to the steady state deviation. Further reduction of overshoot is not possible, as the generation outage happens in proximity to G_1 , and the controllers of G_1 are not fast enough to compensate for this disturbance. The oscillations settle in the first 50 seconds, showing significantly improved oscillation damping. This is also confirmed by the singular value plot in Fig. 4.10, in which many resonant peaks are eliminated with the optimized parameterization. The system \mathcal{H}_∞ norm was reduced by a factor of 5.4, even

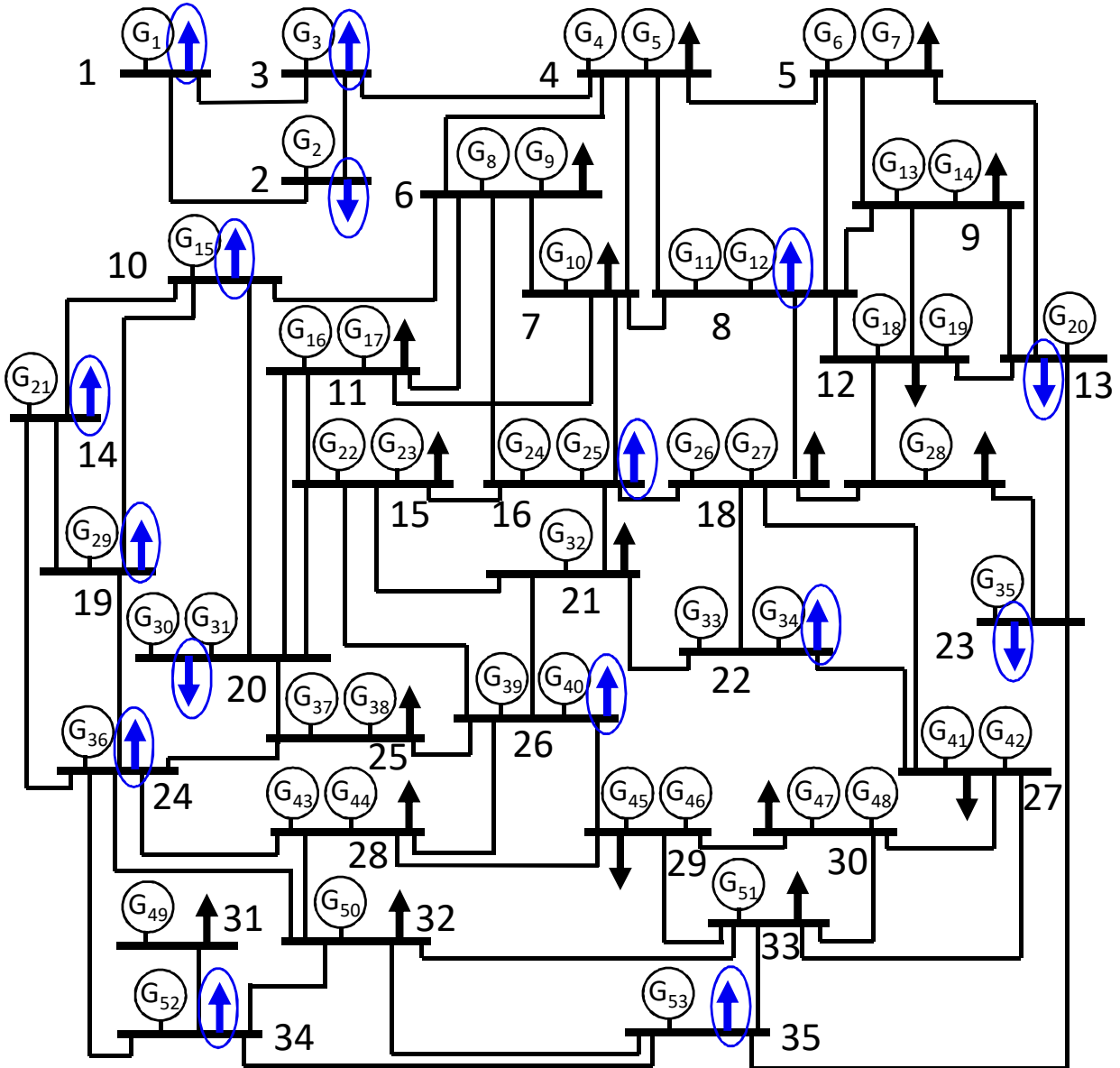


Figure 4.8: The 53 power plant power system developed in the DynaGridCenter project [27]. Buses with uncertain infeeds, denoting disturbances w_i , are marked blue.

though the parameters of only 19 power plants, from a total of 53, were optimized.

4.4 Summary

The applicability of the proposed approach is shown in three power systems. Thereby, the flexibility of the proposed methods is demonstrated as well, as the second system was an AC/DC system, and the third system emulated a brown-field application with additional steady-state constraints. The proposed tuning methods successfully reduced the \mathcal{H}_∞ norm of all considered systems, thereby significantly reducing the

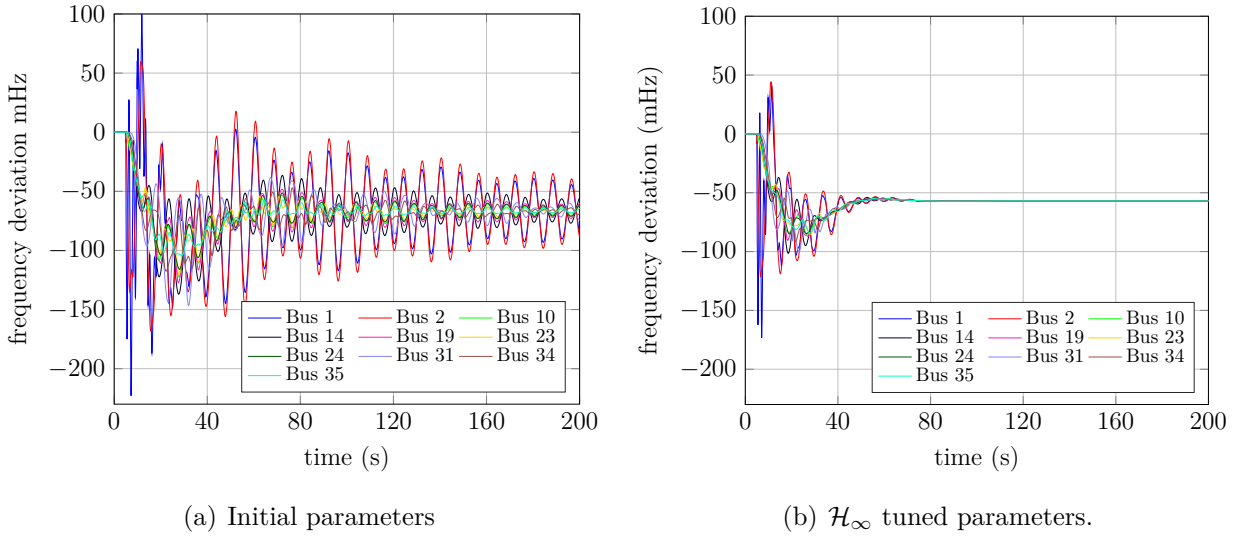


Figure 4.9: Nonlinear simulations of the frequency response in several buses of the reduced European power system model from Fig. 4.8 after a 1.5 GW generator outage in bus 1.

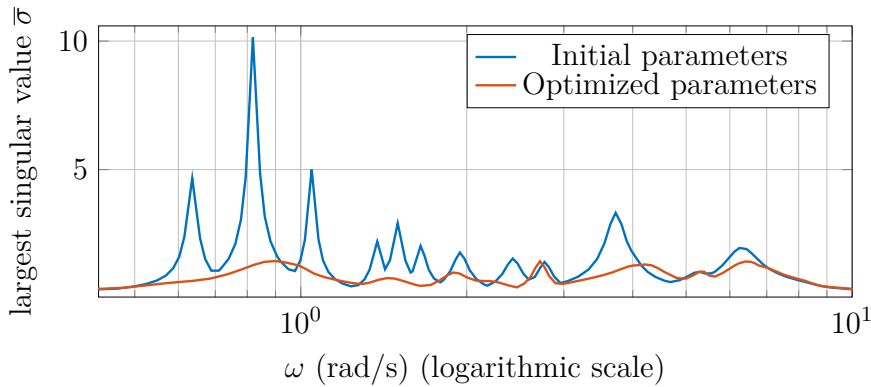


Figure 4.10: Largest singular value of the linearized reduced European power system model from Fig 4.8 as a function of frequency ω . After optimization, most of the resonant peaks in the system are significantly reduced.

time-domain settling time and overshoot of those systems. The presented approaches provide a systematic solution and show very good results for parameter tuning in these complex systems. The outcomes of the optimization are validated in commercial power system simulation software with detailed nonlinear component models, showing the applicability of the approach to practically relevant systems.

5 Experimental validation

In the previous chapter, numerical studies are performed on transmission systems, which consist of power plants with large power infeeds. Online controller reparameterization cannot be easily tested in such systems due to the vital role they play. Furthermore, renewable penetration in the largest systems today is still relatively low, and the need for controller reparameterization is not evident. However, this is starting to change for large island grids [28, 42]. In this chapter, we experimentally validate our approaches. We start with a smaller system, a testbed microgrid in Wildpoldsried, Germany, which was installed in the frame of a research project [1], shown in Fig. 5.1.

The benefits of microgrids are well recognized and accepted [41]. One of the most interesting capabilities of microgrids is islanding, i.e. the ability to operate separately from a supply grid, which can under certain circumstances improve the power quality and reliability of customer supply. In remote and disaster-endangered areas or on ships, islanded microgrids are often the only possibility for power supply. Renewable generation is now a standard component in microgrids due to their low-cost, environmental-friendliness, low maintenance, and non-reliance on fossil fuels, which often need to be brought from far away. Renewables add, however, additional complexity to microgrid control, in comparison to grids running mainly with synchronous generation, such as diesel generators. Renewable power generation varies over time and does not provide spinning reserve in the system. Renewables are thus often combined with a battery storage system to balance the uncertain renewable generation and provide grid forming, i.e. voltage control. Such systems are, however, not N-1 secure in relation to resilience: when the battery or inverter fails, the system can suffer from a blackout. For redundancy, thus, at least two grid-forming inverters are needed. For increased reliability, resilience, and voltage quality, even more inverters are recommended.

The considered system consists of six 55 kVA SINAMICS inverters [3], connected to three Lithium-Ion batteries, and a controllable 150 kW load bank, c.f. Fig. 5.2. The microgrid can operate attached to the supply grid, as well as in islanded operation. Further details can be found in [1, 88]. We consider the case when the microgrid is running independently of the supply grid and all inverters are running in grid-forming mode, i.e. they control their voltage magnitude and frequency based on their active and reactive power infeed, as shown in Fig. 2.6. This leads to increased reliability and power quality in the system, as the failure of one inverter will not cause a blackout when properly configured. In order to enable parallel operation of the inverters, droop control of active and reactive power is used, as described in Subsection 2.1.2. Droop control



Figure 5.1: Photo of the testbed Microgrid in Wildpoldsried, Germany.

is the current state-of-the-art method for control of distributed generations as: (1) it requires only local measurements and no real-time communication or accurate time synchronization, (2) it enables power sharing and parallel operation of grid-forming inverters, (3) it can be implemented on simple control hardware. In order to evaluate the system performance, we perform load steps and evaluate the step response of the system.

The presented microgrid system is of interest for several reasons:

- To avoid circulating currents, two isolating transformers are a part of the system, as shown in Fig. 5.2, which are sources of asymmetry in the load-step response of the inverters. Such asymmetry will also occur if the inverters are geographically distributed within a microgrid. Therefore this configuration is a good test case for a real life setup.
- Results obtained from the setup can directly be transferred to systems with 100% power-electronic based generation. As wind generation and photovoltaics are connected to the power grid via inverters, a similar inverter model as in Fig. 2.6 can be used to model renewable generation for stability studies.

5.1 Initial parameterization

With the initial parameterization of the inverters, shown in Table 5.1, the system is unstable when inverters 1 and 6 are running in parallel. Thereby, the instability is dependent on the system load level. As shown in Fig. 5.3, the system is initially running stable with an approx. 30 kW load. However, when the load changes to 45 kW, the system becomes unstable. Thereby, the inverter oscillations cancel out, and the power P_L at the load is approximately constant. The oscillations are thus not

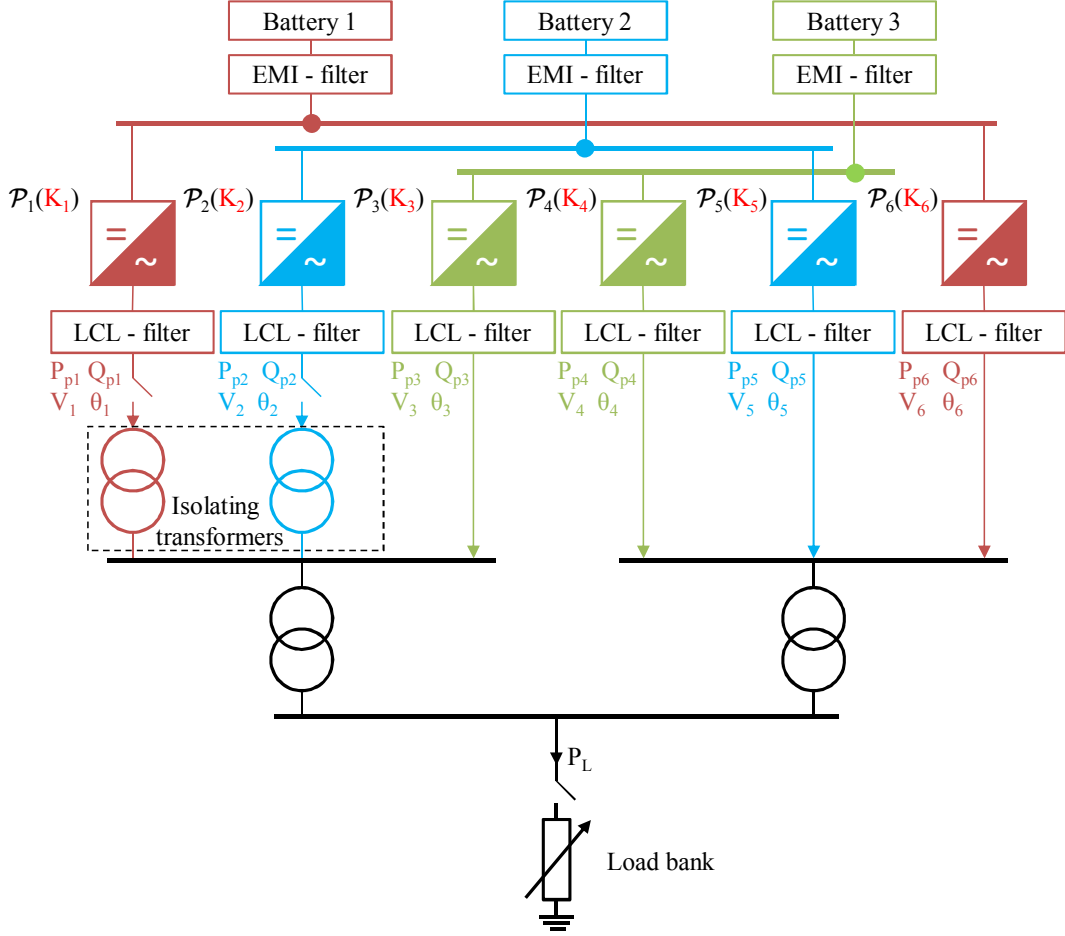


Figure 5.2: Structure of the considered part of the microgrid, consisting of six parallel connected inverters. Details can be found in [88]. The active power of the load bank, denoted with P_L , is the disturbance input w_i into the system.

Table 5.1: Initial unstable parameterization of inverters 1 and 6.

Inv	K_P (%)	K_Q (%)	T_f (ms)	T_v (ms)
1	10	3.1	50	50
6	10	3.1	50	50

observable at the load connection point, meaning that measurements on the load do not show any problems.

This system is unstable even though it consists only of two inverters with the same dynamic behavior and parameterization. The instability arises due to imbalances in the interconnection of the inverters. Counter-intuitively, even though grids with high renewable penetration will have many components with similar dynamics, it does not mean that guaranteeing the stability of such systems is simpler than today. On the contrary, the power grid parameters will play an even more important role, as shown in the following. When only inverters 3 and 4 produce power, the system remains stable with the initial parameterization, as inverters 3 and 4 are connected symmetrically to

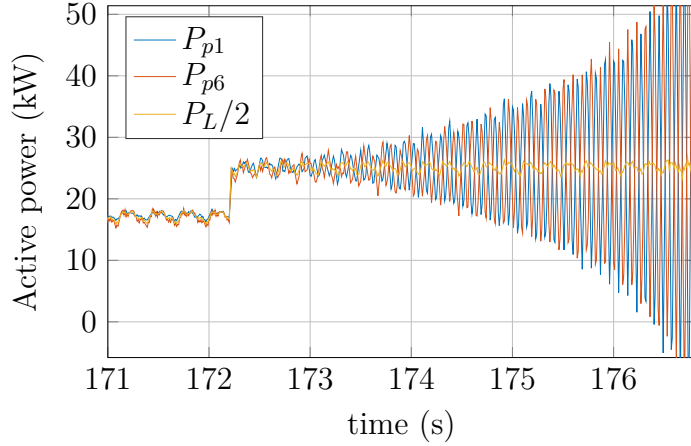


Figure 5.3: Measurements from the testbed grid showing an unstable load step response of inverters 1 and 6 due to a load change from 30 kW to 45 kW; P_L is calculated as the sum of P_{p1} and P_{p6} .

Table 5.2: Stable manual parameterization of inverters 1 and 6.

Inv	K_P (%)	K_Q (%)	T_f (ms)	T_v (ms)
1	2	3.1	100	100
6	2	3.1	100	100

the load. Hence, even in this simple system, the parameters of the power grid between the inverters play an important role.

5.2 Manual tuning

Manual tuning of the system was performed with iterative simulation methods based on the inverter model described in Subsection 2.1.2, see Fig. 2.6. The step response in Fig. 5.4 is obtained with the parameters given in Table 5.2. It shows good correspondence between measurements (solid lines) and simulations (dashed lines), demonstrating the validity of the used model. The difference between measurement and simulation originates from unmodeled loads and/or additional inverter controllers, phase-asymmetries etc. We show active power measurements, because the oscillations are better visible in the active power than in the frequencies for this system.

The same parameters from Table 5.2 are also used for the operation of all six inverters, resulting in the 150 kW load step response shown in Fig. 5.5. A discrepancy in the oscillations is present between measurement and simulation of inverter 3. A better match can be obtained by an iterative adaptation of grid parameters, i.e. impedances in the grid. We avoid this because mismatches between measurements and simulation are expected in real systems, and as it allows to test the sensitivity of the proposed method to model discrepancies. This parameterization of the six inverters was also

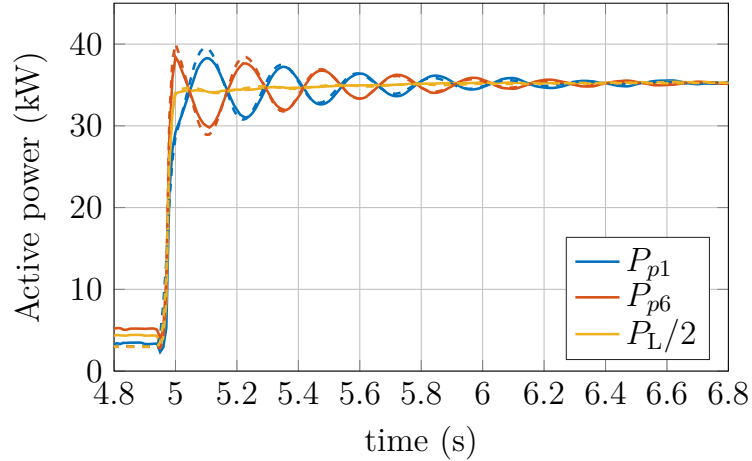


Figure 5.4: Response to a 60 kW load step with inverters 1 and 6 achieved by manual tuning; P_L is calculated as the sum of P_{p1} and P_{p6} . Solid lines represent measurements, whereas dashed lines represent simulations with the nonlinear model.

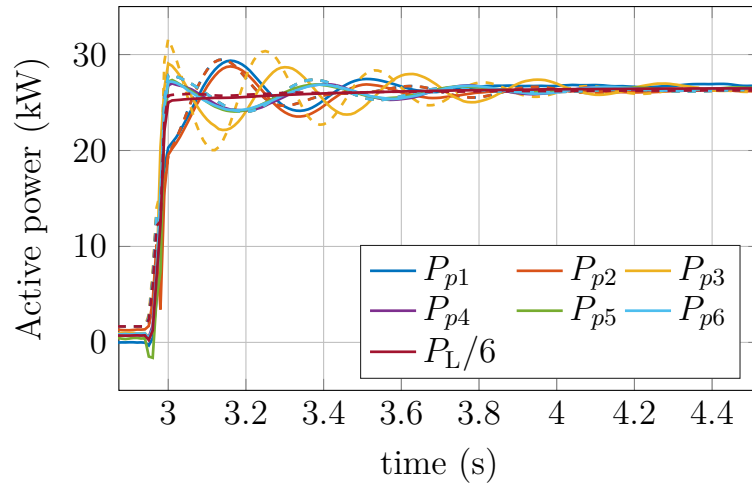


Figure 5.5: Response to a 150 kW load step with all inverters achieved by manual tuning; P_L is calculated as the sum of all inverter powers. Solid lines represent measurements, whereas dashed lines represent simulations with the nonlinear model.

used for successful operation with household consumers in islanded mode.

5.3 Automatic tuning

The results obtained by manual tuning in Figs. 5.4 and 5.5 show prevailing oscillations in the system after a load step. Arguably, they are still satisfactory for many applications. However, manual tuning requires expert know-how and is associated with a significant time-effort. Automatic tuning methods enable the fast design of robust microgrids, without expert knowledge. We apply and experimentally validate the proposed \mathcal{H}_∞ tuning method on the testbed system.

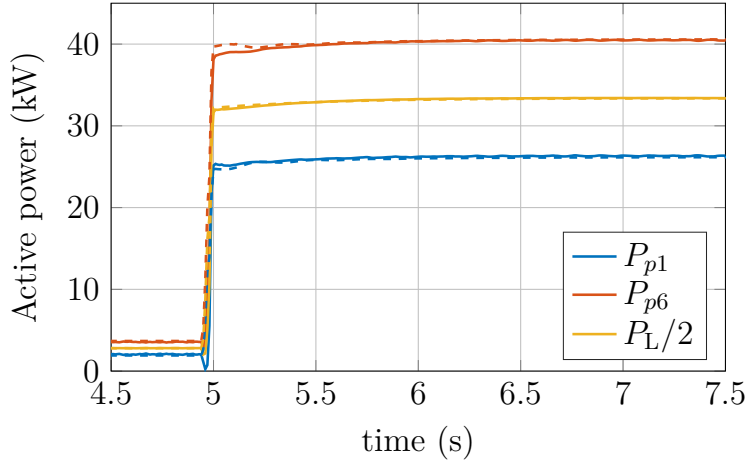


Figure 5.6: Response to a 60 kW load step with inverters 1 and 6 achieved by optimal tuning of all parameters; P_L is calculated as the sum of P_{p1} and P_{p6} . The optimized parameters are shown in Table 5.3. Solid lines represent measurements, whereas dashed lines represent simulations with the nonlinear model.

Table 5.3: Optimal parameterization of inverters 1 and 6 when all parameters are optimized.

Inv	K_P (%)	K_Q (%)	T_f (ms)	T_v (ms)
1	3.13	3.56	108	104
6	2	3.62	115	104

5.3.1 Parameter tuning for inverters 1 and 6

We first apply the \mathcal{H}_∞ parameter tuning algorithm to the system when only inverters 1 and 6 are running. The response for a 60 kW load step with optimized parameters, c.f. Table 5.3, is shown in Fig. 5.6. The settling time of the step response is practically reduced to zero. However, due to different droop values of $K_{P,1}$ and $K_{P,6}$, the steady state power of the inverters is not identical. Such parameterization may cause inverter 6 to overload after a large load step. Still, if the inverters have sufficient power reserves, and no large sudden load changes are expected, this parameterization provides the best step response with regard to oscillation suppression. The generation of the inverters can be balanced out with slower control schemes, so called secondary controllers, which are standard for power system control. As they operate at a slower time scale, they are beyond the scope of this work.

In order to eliminate the generation imbalance even without secondary control, we introduce additional constraints which enforce the equality of the droop gains, i.e. $K_{P1} = K_{P6}$ and $K_{Q1} = K_{Q6}$. With these constraints, we obtain optimized parameters shown in Table 5.4, which achieve the step response shown in Fig. 5.7. We see that, even with the equality constraint, improvement in the step response of the system is still possible compared to manual tuning results.

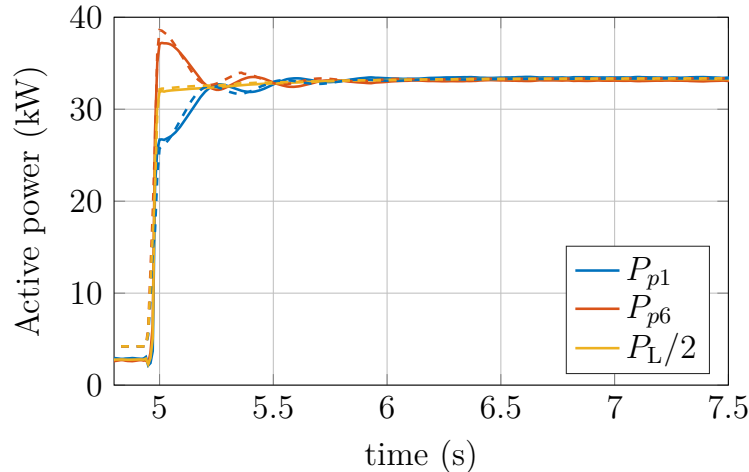


Figure 5.7: Response to a 60 kW load step with inverters 1 and 6 achieved by optimal tuning together with the droop gain equality constraints; P_L is calculated as the sum of P_{p1} and P_{p6} . The optimized parameters are shown in Table 5.4. Solid lines represent measurements, whereas dashed lines represent simulations with the nonlinear model.

Table 5.4: Optimal parameterization of inverters 1 and 6 with droop equality constraints.

Inv	K_P (%)	K_Q (%)	T_f (ms)	T_v (ms)
1	2	3.13	89	100
6	2	3.13	130	100

5.3.2 Parameter tuning for all inverters

For the next experiment, all 6 inverters operate in parallel in grid-forming mode. The 150 kW load step response when all tunable inverter parameters are optimized, is shown in Fig. 5.8. The optimized parameters are shown in Table 5.5. In this case, the oscillations could not be completely eliminated because of insufficient freedom in the controller parameterization. Still, a noticeable improvement is still observable compared to manual tuning, c.f. Fig. 5.5.

To avoid unequal power sharing, equality constraints for the droop gains are introduced, i.e. $K_{P,1} = K_{P,2} = \dots = K_{P,6}$ and $K_{Q,1} = K_{Q,2} = \dots = K_{Q,6}$. The step response for this case is shown in Fig. 5.9, and the obtained parameters in Table 5.6. The overshoot in this case cannot be avoided. However, the power oscillations after the initial overshoot are reduced when compared to the manual tuning results in Fig. 5.5.

5.4 Summary

We experimentally validated the \mathcal{H}_∞ controller tuning approach on a testbed microgrid. The results show a good match between measurements and the inverter models.

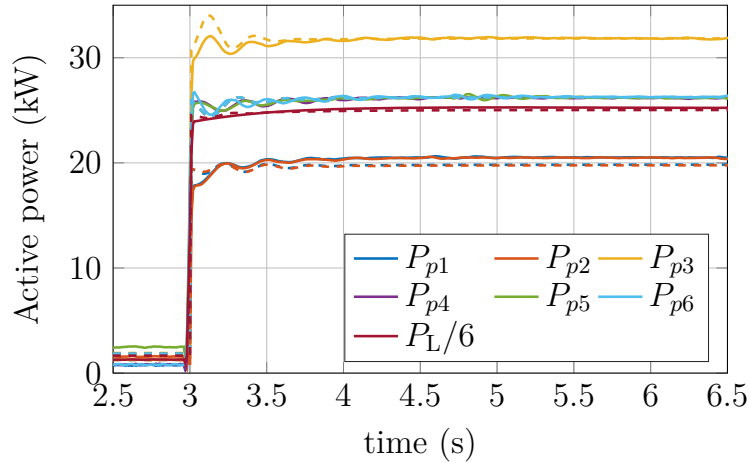


Figure 5.8: Response to a 150 kW load step with all inverters with optimal tuning of all parameters; P_L is calculated as the sum of all inverter powers. The optimized parameters are shown in Table 5.5. Solid lines represent measurements, whereas dashed lines represent simulations with the nonlinear model.

Table 5.5: Optimal parameterization of all inverters 1-6 with no droop equality constraints.

Inv	K_P (%)	K_Q (%)	T_f (ms)	T_v (ms)
1-2	3.1	3.3	107	105
2	3.1	3.6	109	105
3	2	3.5	124	104
4-6	2.1	3.6	102	104

Even though the manual tuning results, as shown in Figs. 5.4 and 5.5, may be satisfactory for many applications, the results obtained with the proposed parameter tuning algorithm, shown in Figs. 5.4 – 5.9, are better with respect to oscillation damping. Thereby, additional droop-equality constraints were added to the optimization problem, demonstrating the flexibility of the proposed optimization methods. Additionally, no expert knowledge is necessary for the automatic parameterization, and the parameterization process can be done faster than with manual tuning.

This chapter also showed that stable operation of relatively complex and asymmetric systems with no synchronous generation is possible. However, the power grid play

Table 5.6: Optimal parameterization of all inverters 1 - 6 with droop equality constraints.

Inv	K_P (%)	K_Q (%)	T_f (ms)	T_v (ms)
1-2	2	3.1	86	96
3	2	3.1	154	101
4-6	2	3.1	123	100

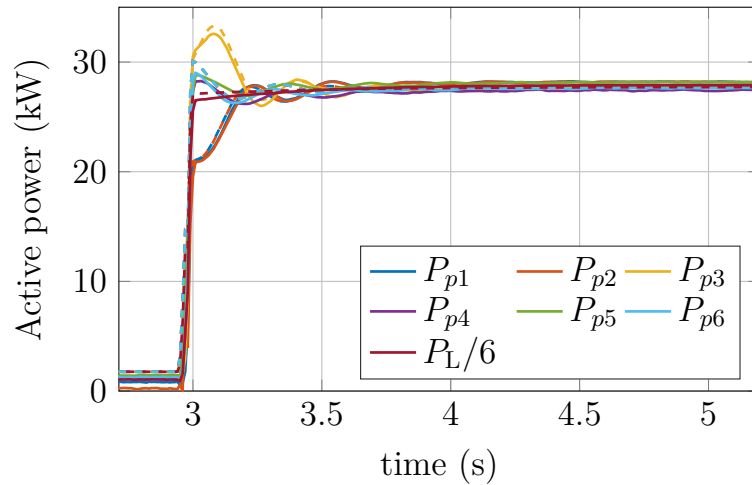


Figure 5.9: Response to a 150 kW load step with all inverters, achieved by optimal tuning and droop equality constraints; P_L is calculated as the sum of all inverter powers. The optimized parameters are shown in Table 5.6. Solid lines represent measurements, whereas dashed lines represent simulations with the nonlinear model.

thereby a more significant role for the stability and needs to be taken into account for the parameter tuning of controllers.

6 Performance comparison

In this chapter, we compare the proposed methods for structured \mathcal{H}_∞ controller synthesis with existing methods. We first evaluate the applications, i.e. controller synthesis in power systems, without boring at the detailed mathematical formulation of the approach. As outlined in Chapter 1, most approaches do not consider the sole parameter tuning, they rather introduce new controllers. To evaluate the benefits and disadvantages of such approaches, we compare in Section 6.1 the proposed approach with two approaches for the synthesis of distributed controllers, focused towards power systems. The focus of the comparison is on the deliverable results in the time- and frequency domain, observed on an exemplary numerical example.

In the second part, we focus on computational efficiency of methods which consider structured \mathcal{H}_∞ controller synthesis. For this purpose, we adapt four methods from literature to the considered application, and compare them in Section 6.2. Thereby, we observe the computation time of these methods on several numerical examples.

6.1 Synthesis methods for distributed controllers

We review and compare in this section the proposed controller tuning approach, i.e. tuning of existing local controllers, with two (sub)optimal controller design methods, tailored towards power systems. Both methods introduce an additional control layer in the system, c.f. Fig. 1.5, however they are "sparsity-promoting". The two methods exploits \mathcal{H}_2 [115] and \mathcal{H}_∞ [100] optimization to create distributed controllers, focusing on the reduction of communication links, while achieving satisfying system performance. We compare all approaches with respect to the transients after a load step, achieved system norms, as well as the necessary communication structures for the control schemes.

The methods proposed in [100, 115] introduce an additional higher-level control layer. They use \mathcal{H}_2 and \mathcal{H}_∞ controller synthesis methods to design optimal static and distributed state-feedback controllers. The additional control layer requires fast communication of all system states to the controller, see Fig. 1.5. This can be challenging in large systems, such as power systems, because fast, reliable and time-synchronized communication across large distances is needed. In order to minimize the dependency on fast communication, these methods aim to minimize the number of communication links necessary. Depending on the desired performance, they achieve a control architecture similar to the one in Fig. 1.5(c), or a fully decentralized architecture depicted in Fig. 1.5(d). We call these methods subsequently "sparsity-promoting \mathcal{H}_2 controller

synthesis” (SPH2), see Subsection 6.1.1, and “sparsity-promoting \mathcal{H}_∞ controller synthesis” (SPHinf), see Subsection 6.1.2.

In the rest of the subsection, we avoid explicitly writing the parameter dependency of the system matrices when it is not necessary, as the considered approaches do not change these parameters. It is assumed, however, that the matrices are always functions of the controller parameters.

6.1.1 Sparsity-promoting \mathcal{H}_2 controller synthesis (SPH2)

This section summarizes the sparsity-promoting \mathcal{H}_2 optimal control design method presented in [59, 114, 115]. This method aims to minimize the \mathcal{H}_2 norm of system (2.8) by introducing and designing the static state-feedback controller \mathcal{K}_2 , where the subindex 2 denotes that the \mathcal{H}_2 norm is used for its synthesis, using the sparsity-promoting optimal control approach. The \mathcal{H}_2 norm of a linear system represents the total output energy of the system response after an impulse of the input. It can also be interpreted as the amplification of white stochastic disturbances from the input to the output. Thus, the \mathcal{H}_2 norm can also be considered as an appropriate tuning goal, as the disturbances from renewable generation and loads represent stochastic disturbances. A more detailed discussion about the use of the \mathcal{H}_2 norm in power systems can be found in [96, 115].

The trade-off between sparsity and \mathcal{H}_2 performance is achieved by tuning of a sparsity emphasis parameter. When the sparsity emphasis parameter is set to zero, the algorithm recovers the optimal centralized controller. By appropriate selection of the sparsity emphasis parameter, control structures as shown in Figs. 1.5(c) and 1.5(d) can be obtained. For this method, we expand the considered system equations (2.8) with the static state-feedback controller $\mathbf{u} = \mathcal{K}_2\mathbf{x}$, and we obtain

$$\dot{\mathbf{x}} = A\mathbf{x} + B\mathbf{w} + B_u\mathbf{u} \quad (6.1a)$$

$$\mathbf{y} = C\mathbf{x} + D_u\mathbf{u} \quad (6.1b)$$

$$\mathbf{u} = \mathcal{K}_2\mathbf{x}. \quad (6.1c)$$

Since this approach considers the \mathcal{H}_2 norm, the feed through matrix of the disturbance input \mathbf{w} to the performance output \mathbf{y} needs to be zero. Otherwise, the \mathcal{H}_2 norm of the system would not be finite [96]. The feedthrough matrix, however, is zero when the prosumer frequencies are considered as performance outputs, and \mathcal{H}_2 optimization can be applied. We denote this system as

$$H_2(s) = (C + D_u\mathcal{K}_2)(sI - A - B_u\mathcal{K}_2)^{-1}B.$$

The \mathcal{H}_2 norm of H_2 is given by [59]

$$J(\mathcal{K}_2) := \|H_2(s)\|_2 = \text{trace}\left(X(C^T C + \mathcal{K}_2^T D_u^T D_u \mathcal{K}_2)\right). \quad (6.2)$$

Here X is the solution to the equation

$$(A + BK_2)X + X(A + BK_2)^T = -BB^T. \quad (6.3)$$

A desired tradeoff between the \mathcal{H}_2 performance and the sparsity of \mathcal{K}_2 is achieved by solving the optimal control problem [59]

$$\min_{\mathcal{K}_2} J(\mathcal{K}_2) + \alpha \|\text{vec}(\mathcal{K}_2)\|_0, \quad (6.4)$$

where the notation $\text{vec}(\mathcal{K}_2)$ creates a vector from the elements of \mathcal{K}_2 by stacking all the columns of \mathcal{K}_2 , and $\|\cdot\|_0$ denotes the 0-norm of a vector, i.e. the number of non-zero elements in the vector. The first term of the objective function (6.4) is smooth and we can use gradient-based methods to solve it. The second term of the objective function is non-smooth and non-convex, making it challenging to solve efficiently. To obtain a smooth cost function, the problem is reformulated into

$$\min_{\mathcal{K}_2} J(\mathcal{K}_2) + \alpha g(\mathcal{K}_2). \quad (6.5)$$

The regularization term $g(\mathcal{K}_2)$ is given by the weighted ℓ_1 -norm of \mathcal{K}_2 ,

$$g(\mathcal{K}_2) := \sum_{i,j} W_{ij} |\mathcal{K}_{2ij}|, \quad (6.6)$$

which is an effective relaxation for inducing elementwise sparsity [16]. This problem can for example be solved iteratively with the so called alternating direction method of multipliers (ADMM) [11]. In each iteration, the weights W_{ij} 's are updated with the values of \mathcal{K}_2 from the previous iteration, see Algorithm 3 and [16] for details. Problem (6.5) allows the synthesis of sparse state-feedback controllers. The sparsity level of the matrix \mathcal{K}_2 depends on the value of the sparsity parameter α . By varying α in (6.5), we can control the sparsity-level which we want to achieve in the system. A larger value for α results in more elements of \mathcal{K}_2 being set to zero, however at the cost of a worse \mathcal{H}_2 performance. With this method, we obtain a family of different distributed controllers with varying sparsity levels and performance. The control designer can then select one with an appropriate sparsity-performance trade-off.

The details of the sparsity-promoting optimal control algorithm can be found in [115]. We perform the numerical evaluation of the SPH2 method in Subsection 6.1.3.

6.1.2 Sparsity-promoting \mathcal{H}_∞ controller synthesis (SPHinf)

We reviews the sparsity promoting \mathcal{H}_∞ controller synthesis presented in [100]. The objective of this method is to design a linear static feedback matrix \mathcal{K}_∞ with as many zero entries as possible. This is similar to the SPH2 method, however it optimizes the \mathcal{H}_∞ system performance instead of the \mathcal{H}_2 system performance.

```

1  $\mu = 1$ ;
2  $\mathcal{K}_{2,0}$  = dense feedback matrix;
3  $W_{ij} = 1, \forall i, j$ ;
4 while stopping criteria not satisfied do
5    $\mathcal{K}_{2,\mu}$  = solution of (6.5) via ADMM with  $\mathcal{K}_{2,\mu-1}$  as initial value;
6    $W_{ij} \leftarrow 1/|\mathcal{K}_{2,\mu,ij}|, \forall i, j$ ;
7    $\mu = \mu + 1$ ;
8 end
9 return ( $\mathcal{K}_{2,\mu}$ )
    
```

Algorithm 3: Optimization algorithm of the SPH2 method for solving (6.5).

We consider again system (2.8), which is extended by a static state-feedback controller \mathcal{K}_∞

$$\dot{\mathbf{x}} = A\mathbf{x} + B_w\mathbf{w} + B_u\mathbf{u} \quad (6.7a)$$

$$\mathbf{y} = C\mathbf{x} + D_u\mathbf{u} \quad (6.7b)$$

$$\mathbf{u} = \mathcal{K}_\infty\mathbf{x}. \quad (6.7c)$$

We denote this system as

$$H_\infty(s) = (C + D_u\mathcal{K}_\infty)(sI - A - B_u\mathcal{K}_\infty)^{-1}B.$$

The centralized controller, i.e. the \mathcal{K}_∞ matrix with all entries non zero, shown in Fig 1.5(b), uses all possible degrees of freedom and can be designed via convex optimization [32]. In order to increase the sparsity of \mathcal{K}_∞ , the following theorem is used in [100], which is derived from the Bounded-Real Lemma (Lemma 1)

Theorem 5 [100] *The following statements are equivalent*

- *There exists a controller \mathcal{K}_∞ which asymptotically stabilizes the system (6.7), such that the \mathcal{H}_∞ norm of (6.7) is smaller than β .*
- *There exist matrices $P_1 \succ 0$, diagonal $P_2 \succ 0$ and matrices L_∞ and U_∞ , such that*

$$\Pi(P_1, P_2, L_\infty, U_\infty, \beta) := \begin{pmatrix} \Delta & P_1B_u + D_u^T L_\infty^T & P_1B_w & C^T \\ B_u^T P_1 + D_u L_\infty & -P_2 & 0 & D_u^T \\ B_w^T P_1 & 0 & -\beta I & 0 \\ C & D_u & 0 & -\beta I \end{pmatrix} \prec 0, \quad (6.8)$$

with

$$\Delta = A^T P_1 + P_1 A - U_\infty^T L_\infty - L_\infty^T U_\infty + U_\infty^T P_2 U_\infty.$$

In this case, the controller is given by

$$\mathcal{K}_\infty = P_2^{-1}L_\infty. \quad (6.9)$$

We refer to [100] for a proof of the given theorem. The theorem provides the conditions when a static state feedback controller \mathcal{K}_∞ achieves a defined \mathcal{H}_∞ performance β . Since P_2 is diagonal and positive definite, i.e. all its diagonal elements are greater than zero, it follows from (6.9) that the sparsity pattern of \mathcal{K}_∞ is the same as the sparsity pattern of L_∞ . Consequently, the theorem leads to the following optimization problem for the sparsity improvement of \mathcal{K}_∞ under a constant performance bound β

$$\min_{P_1, P_2, L_\infty, U_\infty} \|\text{vec}(L_\infty)\|_0 \quad (6.10)$$

$$\text{subject to } \Pi(P_1, P_2, L_\infty, U_\infty, \beta) \prec 0, \quad (6.11)$$

where the notation $\text{vec}(L_\infty)$ creates a vector from the elements of L_∞ by stacking the columns of L_∞ , and $\|\cdot\|_0$ denotes the 0-norm of a vector, i.e. the number of non-zero elements in the vector. The previous problem allows the synthesis of sparse state-feedback controllers with a guaranteed performance bound, however due to the presence of the 0-norm in the cost function, it can be very challenging to solve. In order to improve the computation time, analogously as in SPH2, the 0-norm is relaxed into a weighted 1-norm, and we obtain the optimization problem

$$\min_{P_1, P_2, L_\infty, U_\infty} \|\text{vec}(M_\infty \circ L_\infty)\|_1 \quad (6.12)$$

$$\text{subject to } \Pi(P_1, P_2, L_\infty, U_\infty, \beta) \prec 0, \quad (6.13)$$

where \circ denotes the Hadamard (element-wise) product of two matrices, and $M_\infty = [m^{ij}]$ is a weighting matrix. Note that M_∞ is chosen to be the element-wise inverse of $L_\infty = [l^{ij}]$, i.e. $m^{ij} = \infty$ if $l^{ij} = 0$, and $m^{ij} = 1/|l^{ij}|$ otherwise, then the weighted 1-norm and the 0-norm coincide. The same relaxation is proposed in the SPH2 method as well. Since the weights depend on the solution of the optimization problem, this cost function cannot be used to obtain a convex optimization problem. Thus, an iterative solution, similar to the one presented for the SPH2 method, is proposed. However, even if the weights are set to a constant value in one iteration, the term Π in (6.13) is still non-convex, because U_∞ is multiplied with other optimization variables in $\Pi(P_1, P_2, L_\infty, U_\infty, \beta)$.

To solve this problem, Algorithm 4 is proposed in [100], which gives the SPHinf method its final form. The small positive number ν is introduced in the algorithm to avoid bad conditioning of the problem when $l_k^{ij} = 0$. Step 9 is introduced because the 1-norm penalizes large values in the cost term $M_k L_{\infty, k}$, resulting in a controller with small gain values. In Step 9, there is no term which minimizes these values, and the controller obtained through the iterative procedure can be further polished. With

- 1 $k = 1$;
- 2 $\mathcal{K}_{\infty,cent} \leftarrow$ fully centralized controller, obtained with convex optimization;
- 3 $U_{\infty,1} = \mathcal{K}_{\infty,cent}$;
- 4 Choose m_0^{ij} and a sufficiently small number $\nu > 0$. Choose $\beta > 0$;
- 5 **while** *stopping criteria not satisfied* **do**
- 6 For fixed $U_{\infty,k}$ solve the following convex optimization problem

$$\{P_{1k}^*, P_{2k}^*, L_{\infty,k}^*\} = \arg \min_{P_{1k} \succ 0, \text{diagonal } P_{2k} \succ 0, L_{\infty,k}} \|M_k L_{\infty,k}\|_1 \quad (6.14a)$$

$$\text{s.t. } \Pi(U_{\infty,k}, P_{1k}, P_{2k}, L_{\infty,k}) \prec 0. \quad (6.14b)$$
- 7 Update $U_{\infty,k+1} = (P_{2k}^*)^{-1} L_{\infty,k}^*$ and $m_{k+1}^{ij} = (|l_k^{ij}| + \nu)^{-1}$. ;
- 7 $k \leftarrow k + 1$;
- 8 **end**
- 9 Solve the feasibility problem for the fixed controller structure obtained in Step 6

$$\{P_{1k}^*, P_{2k}^*, L_{\infty,k}^*\} = \arg \min_{P_{1k} \succ 0, \text{diagonal } P_{2k} \succ 0, L_{\infty,k}} 0 \quad (6.15a)$$

$$\text{s.t. } \Pi(U_{\infty,k}, P_{1k}, P_{2k}, L_{\infty,k}) \prec 0 \quad (6.15b)$$

$$L_{\infty,k} \text{ has fixed controller structure from Step 6.} \quad (6.15c)$$

- 10 $\mathcal{K}_{\infty} = (P_{2k}^*)^{-1} L_{\infty,k}^*$;
- 11 **return** \mathcal{K}_{∞}

Algorithm 4: Optimization algorithm the SPHinf method [100].

this algorithm, the problem is reduced to a series of convex linear matrix inequality problems. The convergence of weighted optimization with the 1-norm to a local minimum is proven [30]. However, in Algorithm 4, the constraints are also changed in each iteration of the algorithm. For this reason, convergence of the SPHinf method, as well as of the SPH2 method, to a local minimum cannot be guaranteed. However, fast convergence for many numerical examples is reported in [100]. We perform the numerical evaluation of the presented method in the subsequent Section 6.1.3.

6.1.3 Simulation comparison

We compare the approach considered in this work with the methods for sparsity-promoting synthesis. We refer subsequently the LMI approach from Section 3.1 as “structured \mathcal{H}_{∞} controller synthesis of local controllers” (SHinf). Since SPH2 uses the \mathcal{H}_2 norm as the performance metric, whereas SHinf and SPHinf use the \mathcal{H}_{∞} norm, a direct comparison between all three methods is not straightforward. For this reason,

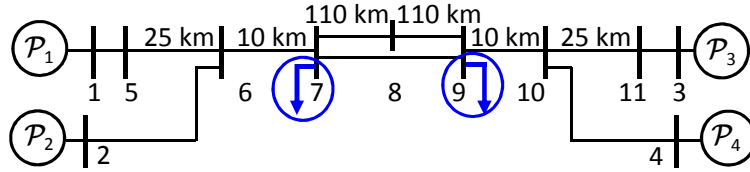


Figure 6.1: A two-area system from [51, p. 813, Example 12.6].

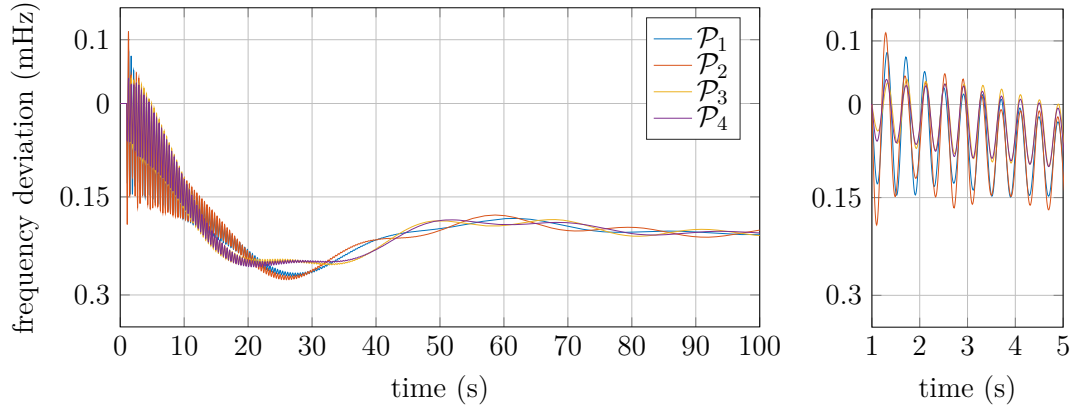


Figure 6.2: (left) Generator frequency response after a 100 MW load step in bus 9. Strong oscillations are present in the system. (right) Zoomed fast oscillations after the load step.

we compare the methods in several aspects on a numerical example:

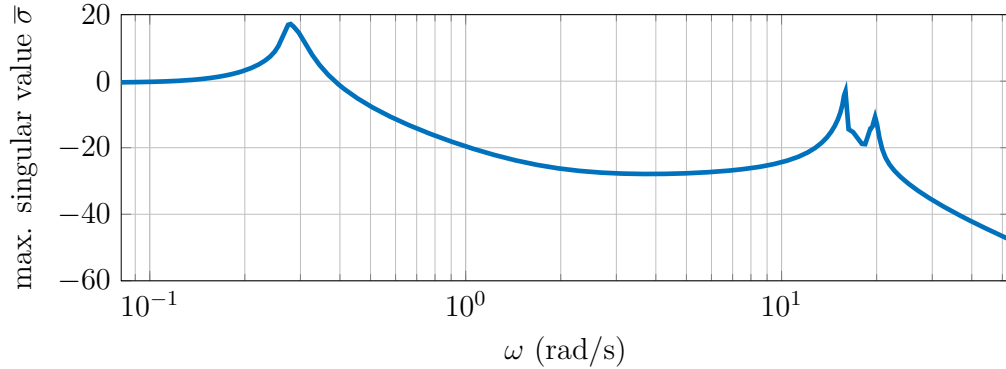
- The achieved \mathcal{H}_∞ and \mathcal{H}_2 norms and how they correlate in the power system example.
- The sparsity patterns in the \mathcal{K}_2 and \mathcal{K}_∞ matrices achieved by SPH2 and SPHinf, respectively.
- Impact on the maximal singular value of the transfer function for all methods.
- Time-domain simulations achieved by a disturbance (load) step.

For the comparison, we consider the four power plant grid from [51, Example 12.6, page 813], see Appendix C.5 and Fig 6.1. The system consists of 48 states and 28 tunable parameters. Thereby, a virtual input is added to the AVR model, which is used as the control input for the SPHinf and SPH2 methods, c.f. Appendix C.5. In order to make the comparison fair, the gain of the TGOV is fixed, i.e. the SHinf method cannot tune it. Consequently, all approaches only influence the voltage control of the power plants, which also includes the power system stabilizer.

Analysis of the system for the initial parameters. Figure 6.2 shows the simulation of the generator frequencies with the initial parameters after a load step in bus 7. In the first 20s after a load step, poorly dampened oscillations with a frequency of

Table 6.1: Poorly dampened modes of the considered system.

mode	frequency (rad/s)	damping ratio (%)
1	9.74	1.7
2	9.42	2.5
3	7.85	0.9
4	0.13	2.8
5	0.13	3.1

**Figure 6.3:** Largest singular value of $G(\mathbf{K}, s)$.

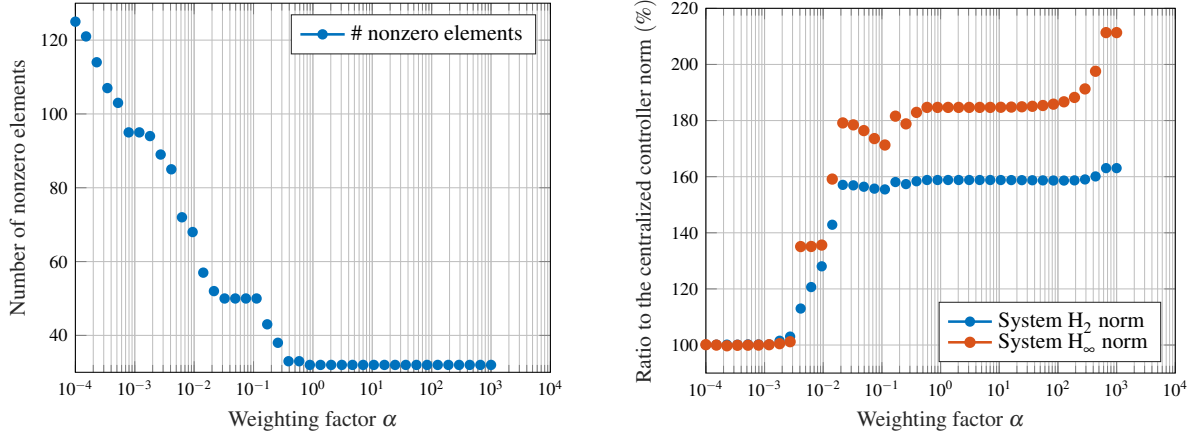
approx. 3 Hz are present. Afterwards, slow oscillations are noticeable, which are not completely dampened even after 100 seconds. Table 6.1 presents the weakly-dampened oscillatory modes of the system, with damping below 5%, which confirm the analysis of the step response plot.

The singular value plot of the system is shown in Fig. 6.3. The frequencies at which the peaks occur in Fig. 6.3 correspond to the oscillatory modes in Table 6.1. The initial system \mathcal{H}_∞ norm is 7.3, and the \mathcal{H}_2 norm is 1. Thus, the considered test system is complex with slow and fast badly-dampened oscillatory modes on which we can test the approaches.

Comparison of optimization results of SPHinf, SPH2, and SPHinf

We now compare the results of the optimization for the defined test system. The numerical results are obtained as follows:

- When the SHinf method is applied, we obtain an optimized parameter vector \mathbf{K}_{opt} . With this vector, an \mathcal{H}_∞ norm of 0.81, and \mathcal{H}_2 norm of 0.82 is achieved. The optimization problem was implemented in Matlab, using SeDuMi [109] and Yalmip [61].
- For the SPH2 method, we first calculate the centralized controller $\mathcal{K}_{2,cent}$ by setting the parameter α in (6.5) to zero. Then, we varied the weighting parameter α from 0.001 to approx. 1000 in 40 logarithmically spaced steps and obtain the matrices $\mathcal{K}_{2,a}$, $a = 1 \dots 40$ with increasing sparsity-degrees. With the completely



(a) Number of nonzero elements in \mathcal{K}_2 . The full controller has 192 elements.

(b) The \mathcal{H}_2 and \mathcal{H}_∞ system norms relative to their respective values for the completely centralized controller.

Figure 6.4: Nonzero elements in \mathcal{K}_2 and the system norms as functions of the weighting γ with the SPH2 method.

centralized controller, we obtain an \mathcal{H}_∞ norm of 0.6824, and an \mathcal{H}_2 norm of 0.4685. The numerical problems were solved using a custom ADMM solver [115].

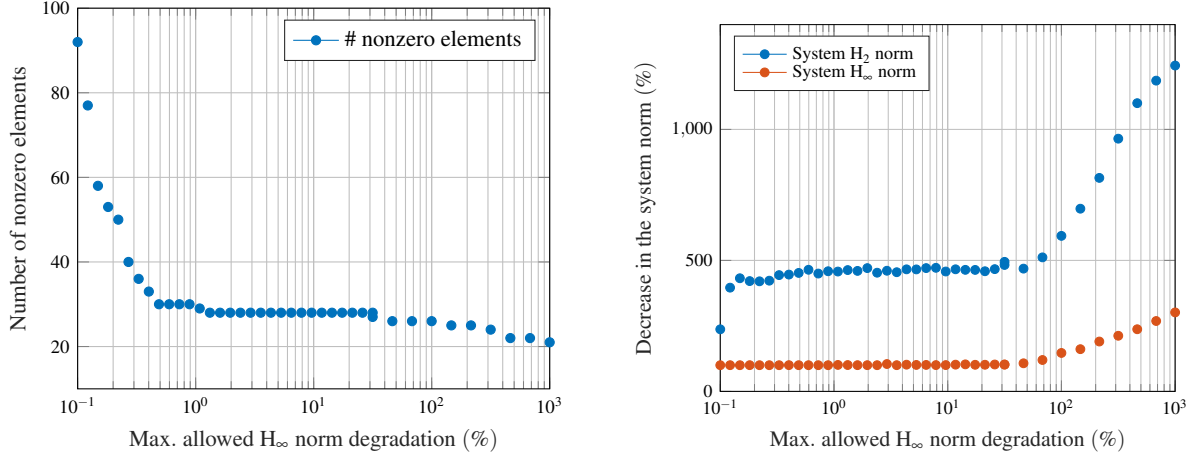
- For the SPHinf method, we also first calculate a centralized controller $\mathcal{K}_{\infty,cent}$ which achieves an \mathcal{H}_∞ norm β_{cent} . We then varied the performance bound β from 1% degradation to approx 32% degradation in 30 steps, and from 32% to 1000% compared to β_{cent} in 10 steps. We obtained the matrices $\mathcal{K}_{\infty,b}$, $b = 1 \dots 40$ matrices with increasing sparsity-degrees. For the calculation of $\mathcal{K}_{\infty,b}$, we use $\mathcal{K}_{\infty,b-1}$ as an initial value for the “hot-start”. For each controller, the iteration limit for the 1-norm weight update was set to 4 (i.e. $k_{max} = 4$ in the algorithm in Algorithm 4). The resulting optimization problem was implemented in Matlab, using SeDuMi [109] and Yalmip [61]. With the completely centralized controller, we obtain an \mathcal{H}_∞ norm of 0.6653, and an \mathcal{H}_2 norm of 0.5018.

Results obtained with the SPH2 method are shown in Fig. 6.4. The number of nonzero elements as a function of α is shown in Fig.6.4(a), and the achieved \mathcal{H}_2 and \mathcal{H}_∞ norms are shown in 6.4(b). Even though SPH2 does not explicitly optimize the \mathcal{H}_∞ norm, it is interesting to see how they correlate for the given system. By increasing α to approx 0.003, we can decrease the number of non-zero elements in \mathcal{K}_2 from 192 in the centralized controller $\mathcal{K}_{2,cent}$ to 89 with only a 3% performance degradation in the \mathcal{H}_2 norm compared to the initial controller $\mathcal{K}_{2,cent}$. We denote this controller with $\tilde{\mathcal{K}}_2$. Afterwards, the performance degradation is relatively steep, and by setting the α to 1.3, we obtain a 60% performance degradation of the \mathcal{H}_2 norm with 32 nonzero elements.

Results obtained with the SPHinf method are shown in Fig. 6.5. The number of

Table 6.2: Comparison of norms of the methods SPHinf, SPH2, and SPHinf.

Norm	Initial	\mathbf{K}_{opt}	$\mathcal{K}_{2,cent}$	$\tilde{\mathcal{K}}_2$	$\mathcal{K}_{\infty,cent}$	$\tilde{\mathcal{K}}_{\infty}$
\mathcal{H}_{∞}	7.3	0.81	0.6824	0.6905	0.6653	0.7137
\mathcal{H}_2	1	0.82	0.4685	0.4825	0.5018	2.3513

(a) Number of nonzero elements in \mathcal{K}_{∞} . The full controller has 192 elements.(b) The \mathcal{H}_2 and \mathcal{H}_{∞} system norms relative to their respective values with the completely centralized controller.**Figure 6.5:** Nonzero elements in \mathcal{K}_{∞} and the system norms as functions of performance limit with the SPHinf method.

nonzero elements as a function of β compared to β_{cent} is shown in Fig. 6.5(a), and the achieved \mathcal{H}_2 and \mathcal{H}_{∞} norms are shown in 6.5(b). SPHinf reduces the number of nonzero elements to 26 with a 7% performance degradation in the \mathcal{H}_{∞} norm compared to the 192 elements from the centralized controllers, however, the \mathcal{H}_2 norm is increased by 470%. We denote this controller as $\tilde{\mathcal{K}}_{\infty}$. The method does not use the full performance degradation available through the constraints, e.g. if a 1000% degradation of the \mathcal{H}_{∞} norm is allowed, the optimization achieves a degradation of 300%. This suggests that it does not converge to a global optimum, as already noted in [100].

The optimized norms for the different controller parameters are shown in Table 6.2. Not surprisingly, the best \mathcal{H}_{∞} norm is achieved with $\mathcal{K}_{\infty,cent}$, and the best \mathcal{H}_2 norm with $\mathcal{K}_{2,cent}$. Interestingly, the degradation of the \mathcal{H}_2 norm from $\mathcal{K}_{2,cent}$ to $\tilde{\mathcal{K}}_2$, and of the \mathcal{H}_{∞} norm from $\mathcal{K}_{\infty,cent}$ to $\tilde{\mathcal{K}}_{\infty}$ is very small, and $\tilde{\mathcal{K}}_2$ achieves a better \mathcal{H}_{∞} norm than $\tilde{\mathcal{K}}_{\infty}$.

In summary, the two methods achieve very different results with regard to the achieved system norms. The SPHinf optimization causes a large increase in the system \mathcal{H}_2 norm, which the SPH2 method avoids, causing large differences in the optimization results regarding the sparsity-performance trade-off. In the following, we compare the methods with regard to the following aspects.

- Sparsity of the obtained controllers: We first show the structure of the $\tilde{\mathcal{K}}_2$ and

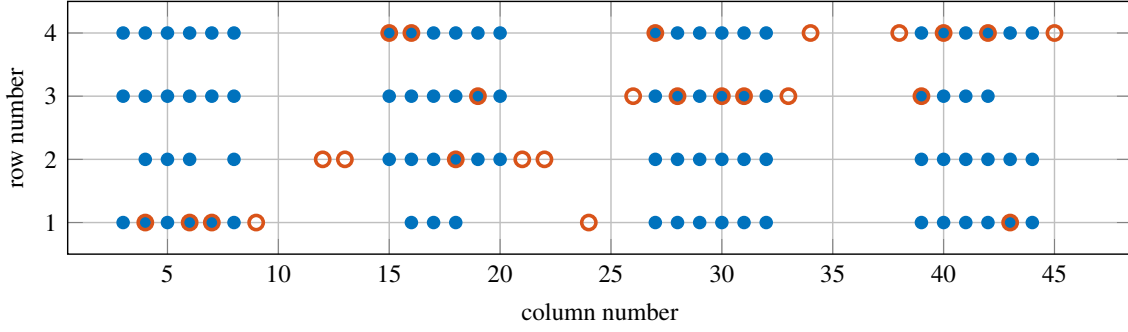


Figure 6.6: Comparison non-zero entries of the $\tilde{\mathcal{K}}_2$ (blue) and $\tilde{\mathcal{K}}_\infty$ (red) matrices.

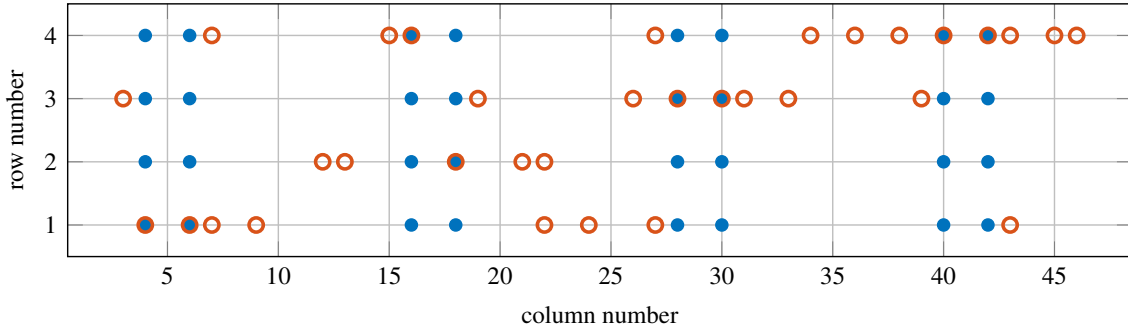


Figure 6.7: Comparison non-zero entries of the $\mathcal{K}_{2,23}$ (blue) and $\mathcal{K}_{\infty,8}$ (red) matrices which have 32 and 33 non-zero elements, respectively.

$\tilde{\mathcal{K}}_\infty$ matrices in Fig. 6.6. Further investigations show that SPH2 mostly uses the states of the AVR and PSS of all generators, as well as the generator angles and frequencies for the state-feedback. On the other hand, SPHinf mostly uses the states of the same power plant (\mathcal{P}) for the controller: e.g., the controller of \mathcal{P}_1 uses mostly the states of \mathcal{P}_1 , with two additional states from \mathcal{P}_2 and \mathcal{P}_4 .

We also analyze the structures of \mathcal{K}_2 and \mathcal{K}_∞ when they both have a similar number of elements. We have chosen the case where SPH2 achieves 32 nonzero elements in the \mathcal{K}_2 matrix, a performance degradation of the \mathcal{H}_2 norm of 60%, and of the \mathcal{H}_∞ norm of 85%. The SPHinf method achieves 33 nonzero elements in the \mathcal{K}_∞ matrix, a performance degradation of the \mathcal{H}_2 norm of 446%, and of the \mathcal{H}_∞ norm of 0.2%. The results are presented in Fig. 6.7. SPH2 focuses in this case only on the states of the PSSs of all power plants, whereas for SPHinf, the choice of the necessary states varies with the power plant controller. Interestingly, SPH2 needs all-to-all communication in both cases, whereas the communication structure for SPHinf is more localized.

- Singular value plot: We now analyze the impact of the methods on the singular value plot of the system, which is shown for the initial system in Fig. 6.3. We show the results obtained with the initial system, \mathbf{K}_{opt} , $\mathcal{K}_{2,cent}$, $\mathcal{K}_{\infty,cent}$, $\tilde{\mathcal{K}}_\infty$, $\tilde{\mathcal{K}}_2$ in Fig. 6.8. We see that all methods were able to eliminate the largest peak in

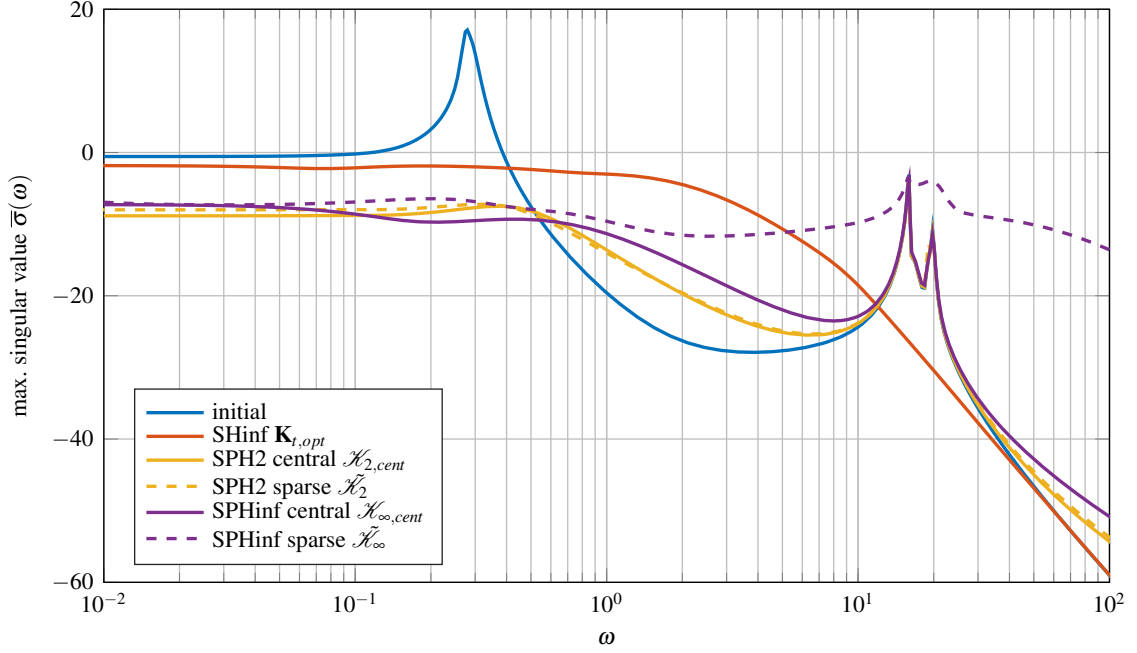


Figure 6.8: Comparison of the singular value plots obtained with the initial system, $\mathbf{K}_{t,opt}$, $\mathcal{K}_{2,cent}$, $\mathcal{K}_{\infty,cent}$, $\tilde{\mathcal{K}}_{\infty}$, and $\tilde{\mathcal{K}}_2$.

Table 6.3: Overshoot and settling time to within ± 0.004 mHz, which corresponds to a $\pm 2\%$ bound of the initial steady-state deviation.

	Initial	SHinf	SPH2	SPHinf
Overshoot (mHz)	0.2762	0.336	0.2535	0.19
Settling time (s)	138	13	93	85

the low frequency range. However, only SHinf is able to eliminate the peak in the 3 Hz area as well. This may be due to the fact that SHinf only tunes the parameters of controllers which were already designed for that specific purpose. All other methods focused on reducing the maximal singular value in the very low frequency area, i.e. below 0.1 Hz, which can only be achieved with significant control effort. However, for better oscillation damping, it is more important to eliminate resonant peaks from the singular value plot than to minimize the maximal singular values in all frequency ranges, see Appendix A.2. Another interesting observation is that the curve obtained with $\tilde{\mathcal{K}}_{\infty}$, which has the worst \mathcal{H}_2 degradation of 446%, has also the largest area below the curve. This corresponds to the SISO interpretation of the \mathcal{H}_2 norm.

- Time domain comparison: Finally, we compare the time-domain step responses after a load step of 100 MW in bus 7 for the parameterizations \mathbf{K}_{opt} , $\mathcal{K}_{2,cent}$, $\mathcal{K}_{\infty,cent}$; shown in Fig. 6.9 with the linear system model. Other time-domain results are visually similar and are thus not included. The SHinf method achieved the best oscillation damping for the tested system, confirming the analysis of

the singular value plot. A possible cause for this is that external controllers \mathcal{K} cannot provide enough compensation if the internal controllers are badly tuned. However, SHinf also shows the largest overshoot after a load step. Better results with the SPH2 and SPHinf methods could possibly be obtained by introducing shaping functions, however this is beyond the scope of this chapter. The overshoot and the settling time are shown in Table 6.3. Even though SHinf has the smallest settling time to within a 2% bound of the steady-state deviation, it achieves the largest overshoot. On the other hand, SPHinf achieves the smallest overshoot.

Discussion: Overall, all three methods are able to improve the closed loop system behavior. As visible from the singular value plot in Fig. 6.8, all methods eliminated the resonant peak at approx. 1 Hz, whereas only SHinf also eliminated the second peak at approx. 3 Hz. These results indicate that, in the considered system, external controllers may not be able to compensate all internal resonances in a system, and that tuning of existing controllers in the system may be necessary. When comparing SPH2 and SPHinf, they achieved very different results regarding the sparsity-performance trade-off. The cause of the difference is that the SPHinf method, while minimizing the system \mathcal{H}_∞ norm, significantly increases the \mathcal{H}_2 norm of the considered system. On the other hand, the SPH2 method, while minimizing the \mathcal{H}_2 norm, also achieved a good \mathcal{H}_∞ norm. In the time domain, SHinf achieved the best settling time, however at the cost of an increased overshoot. SPH2 and SPHinf decreased both the settling time and overshoot, however the 3 Hz oscillation is still present.

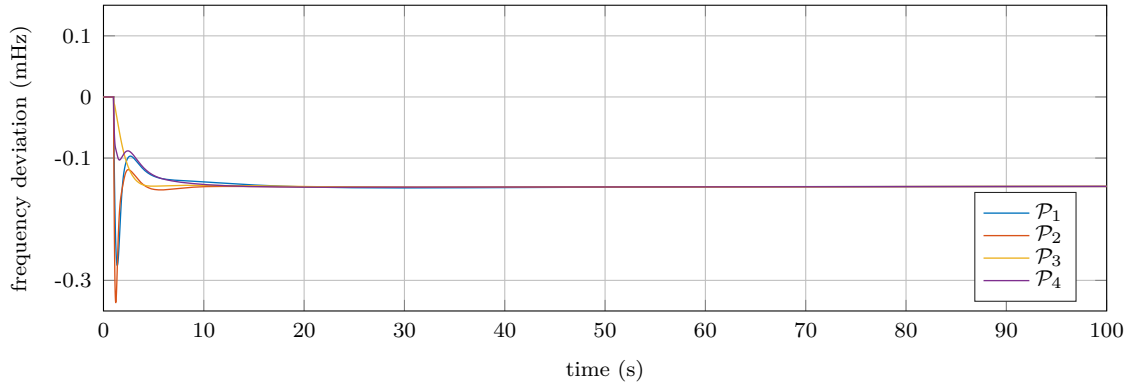
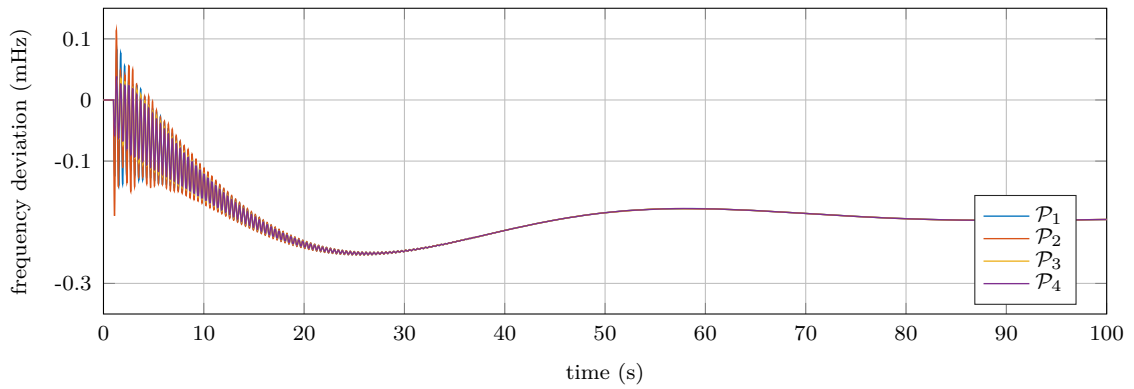
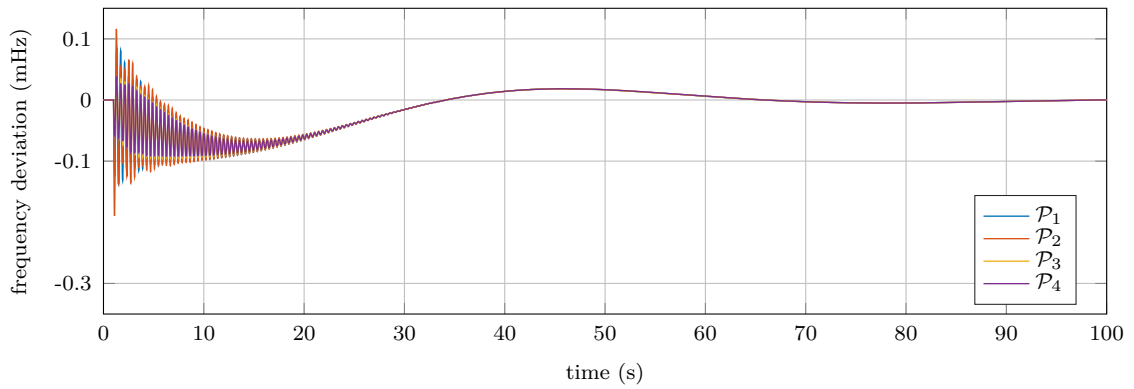
(a) \mathbf{K}_{opt} parameterization.(b) $\mathcal{K}_{2,cent}$ parameterization.(c) $\mathcal{K}_{\infty,cent}$ parameterization.

Figure 6.9: Time-domain simulation after a load step in bus 7 with the parameterizations \mathbf{K}_{opt} , $\mathcal{K}_{2,cent}$, $\mathcal{K}_{\infty,cent}$.

6.2 Computational complexity of structured \mathcal{H}_∞ synthesis methods

We compare in the following section the computational complexity of the proposed methods for \mathcal{H}_∞ synthesis with several methods from the literature. We consider methods which solve Problem (2.12), i.e.:

$$\min_{\mathbf{K}} \|G(\mathbf{K}, s)\|_\infty = \|C(\mathbf{K})(sI - A(\mathbf{K}))^{-1}B(\mathbf{K}) + D(\mathbf{K})\|_\infty \quad (6.16a)$$

$$\text{s.t. } \underline{\mathbf{K}} \leq \mathbf{K} \leq \overline{\mathbf{K}}. \quad (6.16b)$$

The comparison is done with respect to the computation times, achieved \mathcal{H}_∞ norm, as well as scalability. For this purpose we consider the path-following method [40], linearized convex-concave decomposition [24], non-smooth optimization from the systune toolbox in MATLAB [70], and the projection approach from [48]. Thereby, we expand these methods to be applicable to nonlinear parameter dependencies. Other methods, which assume a static output feedback formulation of the problem, such as cone complementarity linearization and sequential linear programming matrix method [8, 29, 32, 56, 99] are not included in the comparison, as they introduce transformations only applicable to specific linear parameter dependencies. Before the comparison, we first briefly summarize the considered methods and present their extensions to a nonlinear parameter dependency.

6.2.1 Path-following (homotopy) method

The basis for this method is Lemma 1 (Bounded-real lemma). It is similar to the method proposed in Section 3.1, as it considers Problem (3.2). However, instead of alternately optimizing P and \mathbf{K} , this approach proposes to linearize all bilinear matrix products in (3.2b). For example, the term $PA(\mathbf{K})$ is linearized around the values \hat{P} and \hat{A} with

$$PA(\mathbf{K}) = (\hat{P} + \Delta P)(\hat{A} + \Delta A(\mathbf{K})) = \hat{P}\hat{A} + \hat{P}\Delta A(\mathbf{K}) + \Delta P\hat{A} + \Delta P\Delta A(\mathbf{K}) \quad (6.17)$$

$$\approx \hat{P}\hat{A} + \hat{P}\Delta A(\mathbf{K}) + \Delta P\hat{A}, \quad (6.18)$$

where ΔP and $\Delta A(\mathbf{K})$ contain the new optimization variables and represent (small) deviations from the linearization points. All other bilinear terms in (3.2b) are linearized analogously. In [40], an iterative LMI optimization approach is proposed, where the values from the previous iteration are used as linearization points. We extend this method for nonlinear parameter dependency analogously as in Section 3.1, i.e. by iteratively linearizing the parametric dependency as well. In [40], the authors propose adding a proximal-regularization term for the Lyapunov matrix in the cost function, i.e. a quadratic cost term $0.5 \cdot \Delta P \times \Delta P$ in addition to minimizing the \mathcal{H}_∞ norm,

which is also subsequently evaluated.

6.2.2 Linearized convex-concave decomposition

This method is only applicable to systems whose B matrix is not a function of \mathbf{K} . Thus, in general, it is not applicable to all power system models. However, this assumption holds for the subsequently considered numerical examples. This method also considers Problem (3.2), based on the Bounded-real Lemma. A convexification is proposed in [24], where the bilinear term $A(\mathbf{K})^T P + PA(\mathbf{K})$ is first decomposed into a convex and a concave part, e.g. with

$$A(\mathbf{K})^T P + PA(\mathbf{K}) = J(\mathbf{K}, P) - H(\mathbf{K}, P) \quad (6.19)$$

$$J(\mathbf{K}, P) = \frac{1}{2}(A(\mathbf{K}) + P)^T (A(\mathbf{K}) + P) \quad (6.20)$$

$$H(\mathbf{K}, P) = \frac{1}{2}(A(\mathbf{K}) - P)^T (A(\mathbf{K}) - P), \quad (6.21)$$

where J is convex and H is a concave function of A. Thus, (3.2b) becomes

$$\begin{pmatrix} J(\mathbf{K}, P) - H(\mathbf{K}, P) & PB & C(\mathbf{K})^T \\ B^T P & -\gamma I & D(\mathbf{K})^T \\ C(\mathbf{K}) & D(\mathbf{K}) & -\gamma I \end{pmatrix} \prec 0, \quad (6.22)$$

where we assume that B is not a function of \mathbf{K} . By using the Schur lemma, the previous matrix inequality can be transformed to

$$\begin{pmatrix} H(\mathbf{K}, P) & -PB & -C(\mathbf{K})^T & (A(\mathbf{K}) + P)^T \\ -B^T P & \gamma I & -D(\mathbf{K})^T & 0 \\ -C(\mathbf{K}) & -D(\mathbf{K}) & \gamma I & 0 \\ (A(\mathbf{K}) + P) & 0 & 0 & 2I \end{pmatrix} \succ 0. \quad (6.23)$$

In the last expression, all terms are linear functions of \mathbf{K} and P , except $H(\mathbf{K}, P)$. However, since H is concave, a linearization of H , denoted with H_L is always greater than H , i.e. $H_L(\mathbf{K}, P) \succ H(\mathbf{K}, P), \forall \mathbf{K}, P$. This fact is used in [24] to construct an iterative LMI optimization algorithm to solve (3.2). Thereby, H is linearized in each iteration around the values from the previous iteration. For a linear parametric dependency, it can be shown that the algorithm converges to a (local) optimum. We extend this algorithm to nonlinear parameter dependencies by iteratively linearizing the parameter dependency as well.

6.2.3 Non-smooth optimization

Non-smooth optimization methods focus on directly solving

$$\min_{\underline{\mathbf{K}} < \mathbf{K} \leq \overline{\mathbf{K}}} T(\mathbf{K}), \quad (6.24)$$

where $T(\mathbf{K}) = \max_{\omega \in \mathbb{R}_{\geq 0}} \bar{\sigma}(G(\mathbf{K}, j\omega))$, by explicitly calculating the gradient of the cost function. However, since T is not differentiable, non-smooth optimization techniques, such as sub-gradient methods, need to be used to solve (6.24). Such methods are implemented, e.g. in the open source MATLAB toolbox HIFOO [37], or in the commercial toolbox from MATLAB called systune [70]. We use systune subsequently in the comparison. It can directly handle nonlinear parameter dependencies, so no adjustments are necessary.

6.2.4 Projection onto the cone of positive definite matrices

The last method we consider uses the projection of a BMI onto the cone of positive definite matrices [48] for the tuning. This projection is defined with

$$[A]^+ = \arg \min_{S \succeq 0} \|A - S\|_F, \quad (6.25)$$

where $\|\cdot\|_F$ denotes the Frobenius norm of a matrix. Given the eigenvalue composition of A , i.e. $A = U\Lambda U^T$, where U is an orthogonal matrix containing the eigenvectors of A , and Λ is a diagonal matrix containing the eigenvalues of A , i.e. $\Lambda = \text{diag}\{\lambda_1, \dots, \lambda_n\}$. Then $[A]^+$ is calculated with $[A]^+ = U \text{diag}\{\lambda_1^+, \dots, \lambda_n^+\} U^T$, where $\lambda_i^+ = \max(0, \lambda_i)$. The basic idea of this method is that a matrix A is negative definite if and only if $\|[A]^+\|_F = 0$. Thus, we have

$$M(\gamma, \mathbf{K}, P) \prec 0 \quad \Leftrightarrow \quad \|[M(\gamma, \mathbf{K}, P)]^+\|_F = 0, \quad (6.26)$$

where M is defined in (3.2b). Note that $\|[M(\gamma, \mathbf{K}, P)]^+\|_F$ is a differentiable function whose gradient can be analytically calculated [48]. In [48], the following optimization problem is proposed for a constant γ

$$\min_{\mathbf{K}, P} \quad \|[M(\gamma, \mathbf{K}, P)]^+\|_F \quad (6.27a)$$

$$\text{s.t.} \quad \underline{\mathbf{K}} \leq \mathbf{K} \leq \overline{\mathbf{K}}. \quad (6.27b)$$

The system \mathcal{H}_∞ norm is smaller than γ if and only if the solution of (6.27) is zero. A line search can then be made on γ to obtain the minimal \mathcal{H}_∞ norm. For the considered problem, better results were obtained by setting $\|[M(\gamma, \mathbf{K}, P)]^+\|_F = 0$ as a constraint, thus transforming (6.27) into a feasibility problem. By using a nonlinear solver, this method can directly incorporate nonlinear parameter dependencies. For this purpose,

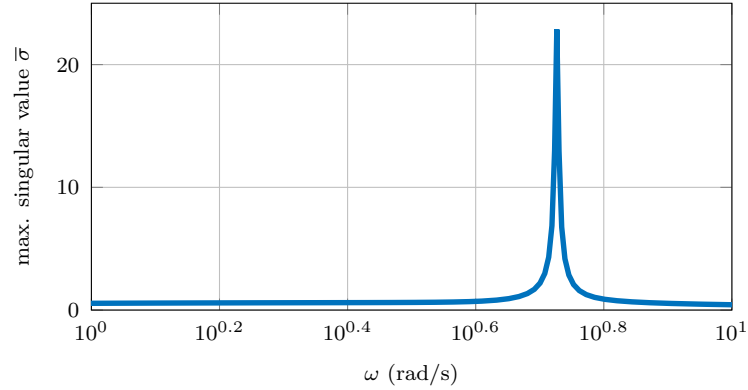


Figure 6.10: Singular value plot of the small 2 generator system.

the *fmincon* solver from MATLAB is used.

6.2.5 Comparison of computation times

We use for the comparison a Windows computer with an Intel[®] i7-4810MQ CPU running at 2.8 GHz and with 8 GB of RAM. Note that the presented times should only give a hint about the computational complexity, as more tailored methods would allow to further decrease the computation time.

We start the comparison with a small system with two power plants, 28 states and 16 optimization parameters. The system is obtained by taking the four power plant grid (see Appendix C.5), disconnecting power plants 2 and 4 with their connecting branches, and by dividing the load in half. The initial \mathcal{H}_∞ norm of the system is 23. Figure 6.10 shows the singular value plot of the system. Based on this plot, the grid $\Omega = \left\{ \omega_k \mid \omega_k = 4 + 0.1 \cdot (k - 1), k = 1 \dots 31 \right\}$ is chosen for the frequency sampling method. Table 6.4 summarizes the comparison results for this system. All methods improved the system \mathcal{H}_∞ norm. Thereby, the systune toolbox, deploying non-smooth optimization, achieves the smallest \mathcal{H}_∞ norm. The frequency sampling method achieves a similar norm, but in 20% of time systune required. They are followed by the PK iteration, which achieves a similar system norm as the convex-concave decomposition, but in 75% of the time. The path-following method achieves a worse system norm, but with the second-fastest time. Path following with proximal regularization also achieves a similar norm. However, with significantly increased computation times. With the projection method, the obtained system norm is the largest, and, even on the small system, the optimization time is over 20 minutes. This is due to the necessity for an eigenvalue decomposition in every step in the inner optimization in one iteration. Since our goal is to find scalable optimization methods, we do not consider path-following with proximal regularization and the projection method subsequently in larger examples.

The second example we consider is the four power plant system (see Appendix C.5).

Table 6.4: Comparison of structured \mathcal{H}_∞ synthesis methods on a system with two power plants, 28 states and 16 optimization parameters. The initial \mathcal{H}_∞ norm of the system is 23.

method	\mathcal{H}_∞ norm	computation time	outer iterations
PK iteration	0.72	83 s	50
Frequency sampling	0.48	6 s	3
Path-following (PF)	1.1	29 s	16
PF with proximal-regularization	1.1	343 s	16
Convex-concave decomposition	0.83	112 s	50
<i> systune </i>	0.42	31 s	NA
Projection method	4.8	1300 s	7

Table 6.5: Comparison of structured \mathcal{H}_∞ synthesis methods on a system with four power plants, 56 states and 32 optimization parameters. The initial \mathcal{H}_∞ norm of the system is 11.5.

method	\mathcal{H}_∞ norm	computation time	outer iterations
PK iteration	0.65	670 s	50
Frequency sampling	0.56	27 s	5
Path-following	1.9	640 s	50
Convex-concave decomposition	1.18	1264 s	50
<i> systune </i>	0.27	687 s	NA

This system has 56 states, 32 optimization parameters, and an initial \mathcal{H}_∞ norm of 11.5. Table 6.5 summarizes the results with the considered methods. Again, *systune* achieved the smallest \mathcal{H}_∞ norm of the system, reducing the norm to approx. 2.3% of the initial value. The frequency sampling method, using the same frequency grid as in the previous example, achieved similar results by reducing the system norm to 4.9% of the initial value, but with a 25 times faster computation time. The PK iteration achieves the third-best \mathcal{H}_∞ norm, with a computation time similar to *systune*.

The third considered example is the ten power plant system from Appendix C.1. For this system, most of the methods reach the limit for practically tolerable computation times. The tuning with *systune* could not be done due to an "out of memory" error. The optimization results are shown in Table 6.6. The PK iteration, path-finding, and convex-concave decomposition have large computation times due to the presence of the Lyapunov matrix, whose size scales quadratically with the number of constraints. For this system, the total computation time for these methods is in the range of one to several days. Only the frequency sampling method was able to find a solution in reasonable time by using the grid $\Omega = \{0.01, 3, 4, 5, 6\} \cup \{\omega_k \mid \omega_k = 7 + 0.1 \cdot (k - 1), k = 1 \dots 81\}$. Thereby, the density of the grid was increased in the frequency interval with resonant peaks, shown in the singular value plot in Fig. 4.4.

A summary of the computation times for the different methods is shown in

Table 6.6: Comparison of structured \mathcal{H}_∞ synthesis methods on the IEEE 39 bus system with ten power plants, 190 states and 100 optimization parameters. The initial \mathcal{H}_∞ norm of the system is 27.7.

method	\mathcal{H}_∞ norm	computation time	outer iterations
PK iteration		3800 s per iteration	
Frequency sampling	2.33	266 s	4
Path-following		8257 s per iteration	
Convex-concave decomposition		13700 s per iteration	
<i>systune</i>		out of memory error	

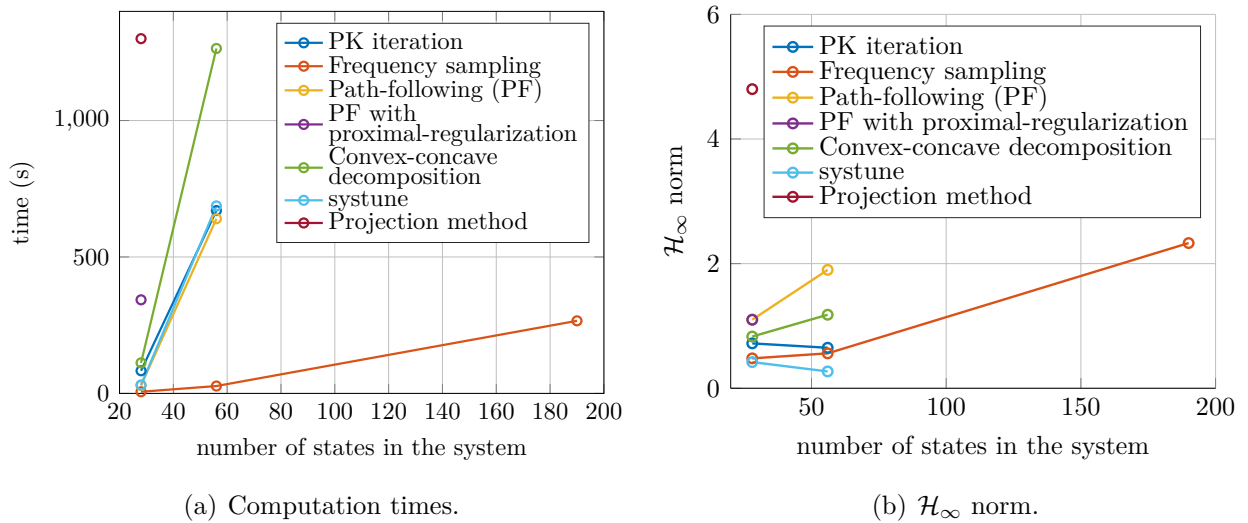


Figure 6.11: Comparison of computation times and achieved \mathcal{H}_∞ norms for the different methods.

Fig. 6.11(a). It shows that the frequency sampling method achieves much smaller computation times, while being only behind *systune* with respect to the achieved \mathcal{H}_∞ norm. However, the performance of the frequency sampling is strongly dependent on the size of the frequency grid. It is important to choose the smallest grid that covers the necessary frequency area with sufficient density. However, this was not a problem for the considered systems.

6.3 Summary

In this chapter, we compared the proposed approaches with existing methods from the literature in two aspects. In the first part, we made the comparison only with respect to the achieved results in the frequency and time domain. For this comparison, we used the SPH2 method from [115] and the SPHinf method from [100], which synthesize additional static state-feedback controllers using \mathcal{H}_2 and \mathcal{H}_∞ optimization methods, respectively, with varying degrees of decentralization. We applied these methods for

power oscillation damping in power systems on a test system with four power plants. The first part is concluded with the comparison of the numerical results in the time and frequency domain with the three presented methods, as well as the obtained sparsity results.

In the second part, we made a computational complexity comparison. The comparison is made on three systems, with 28, 56, and 190 states, respectively. The results, summarized in Fig. 6.11, show that the proposed frequency sampling method outperforms by far other approaches regarding computation time, while only being marginally outperformed by *systune* with regard to the achieved \mathcal{H}_∞ norm. Furthermore, the frequency sampling method was the only one which could tune the parameters of the largest system in a reasonable time, whereas other methods would require more than a day for such computation. However, the performance of the frequency sampling method depends on the chosen frequency grid.

7 Multi-scenario structured controller synthesis

So far, we always optimized one parameter vector \mathbf{K} for one system realization $G(\mathbf{K}, s)$. However, often one is interested in a parameter vector \mathbf{K} which can be used for several system realizations/scenarios n_s , with $G_\kappa(\mathbf{K}, s)$, $\kappa = 1 \dots n_s$, c.f. Fig. 7.1. Such parameterizations are desirable to avoid unnecessary switching of parameters if satisfactory performance for a set of scenarios can be achieved with one parameter vector. Similarly, if the current realization of the system is not exactly known, but only the set of possible system realizations, one parameterization is required which stabilizes and/or improves the performance for possible scenarios.

An example can be fault-tolerant control: failures in power system components, such as power plants or a power lines, can happen instantaneously. This causes a change in the system dynamics, i.e. the system is switched to a different scenario. This switch can occur very fast. There might not be enough time to tune the controllers or to switch to another parameter set, e.g. to ensure stability, after the fault occurred. In such cases, the pre-fault parameterization needs to be able to stabilize the system to give the operator or fault management unit enough time to find a new parameterization or to switch to a pre-calculated one, which is optimized for the new system realization. We focus on parameter tuning for improved post-failure behavior of the system, often referred to as dynamic security of power systems [47]. However, the same approach is not limited to this. It is applicable to any case when one parameter set is needed for multiple possible scenarios.

Handling the dynamic security, i.e. the stability of a power system after a contingency, is typically a challenging issue for power system operators in their routine operation [47]. With the term contingency, we denote the failure of components in a power system. Dynamic security in power systems is often considered in the system analysis after the design, i.e. by simulation studies, c.f. [47, 50, 76], or in combination with redispatch measures which are proposed based on a large number of simulations [21, 118]. To the knowledge of the authors, none of the existing works consider parameter tuning to improve dynamic security of power systems. The tuning for improved dynamic security is typically done a priori, before any contingency occurs. Often one parameter set is obtained for the prosumer controllers which stabilizes the system and increases resiliency after the failure of critical prosumers and power lines. For this purpose, we first introduce an appropriate modeling framework in Section 7.1. We then extend the proposed controller tuning methods to multiple scenarios in Section 7.2. Finally, the developed approach is applied to improve dynamic security of the IEEE 39 bus system in Section 7.3 before the chapter is summarized in Section 7.4.

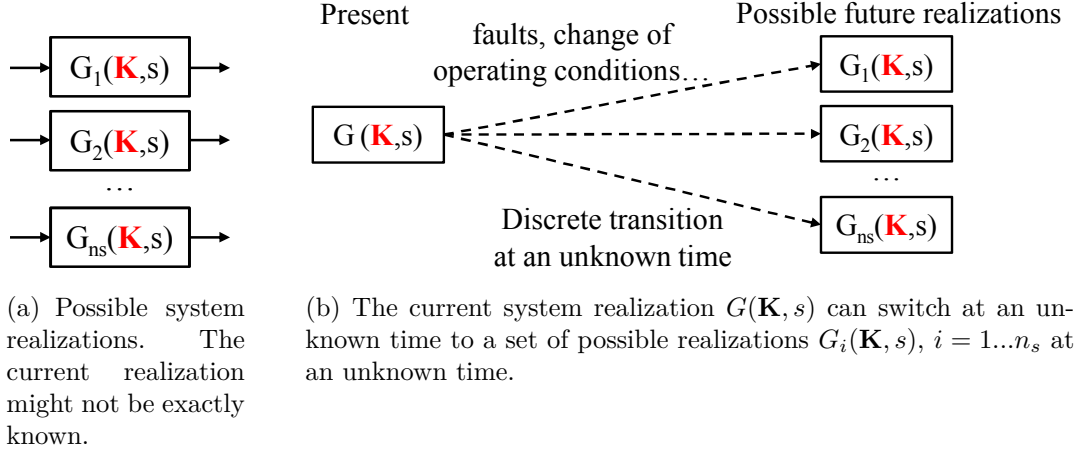


Figure 7.1: Examples when multi-scenario tuning is necessary. One parameter vector is needed which stabilizes and/or improves the performance for all systems.

7.1 Modeling of contingencies

Contingency in a power system denotes the failure of a dynamic prosumer or a branch element, e.g. a power line, transformer, a flexible AC transmission system (FACTS) device etc. We outline how contingencies can be modeled, such that they can be considered in the parameter tuning, relying on the system input-output behavior.

7.1.1 Modeling dynamic prosumer dropouts

We outline the modeling of dynamic prosumer dropouts on the example of a power plant. The dropout of other dynamic prosumers can be handled analogously. When a fault occurs in a power plant, a breaker almost instantly disconnects the power plant from the grid for security. Thus, the dynamics of the power plant does not influence other components, and the power plant dynamics can be ignored after the dropout. Consequently, we replace the power plant that shall drop out in the optimization model by a static prosumer whose infeed drops from P_{pi} , Q_{pi} to zero, see Fig. 7.2. Since P_{pi} and Q_{pi} change simultaneously to zero when the power plant drops out, we model them as a single disturbance input w into the system. As P_{pi} and Q_{pi} can have significantly different magnitudes, we introduce weighting factors $\alpha_{P_{pi}}$ and $\alpha_{Q_{pi}}$:

$$\sigma_{pi} = |P_{pi}| + |Q_{pi}|, \alpha_{P_{pi}} = P_{pi}/\sigma_{pi}, \alpha_{Q_{pi}} = Q_{pi}/\sigma_{pi}. \quad (7.1)$$

The disturbance input for the dropout of a generator is defined as

$$\mathbf{w}_p = \begin{pmatrix} P_{pi} \\ Q_{pi} \end{pmatrix} = \begin{pmatrix} \alpha_{P_{pi}} \\ \alpha_{Q_{pi}} \end{pmatrix} \sigma_{pi} w_p. \quad (7.2)$$

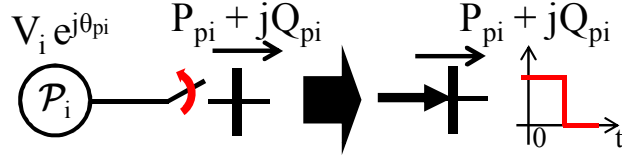


Figure 7.2: A graphical representation of the proposed modeling for failing power plants. The power plant is replaced by a constant power infeed with the same power as the generator.

Without the normalization, i.e. using $\alpha_{P_{pi}} = 1$ and $\alpha_{Q_{pi}} = 1$, the optimizer would focus on suppressing oscillations resulting from equal step sizes in both inputs P_{pi} and Q_{pi} . The normalization ensures that the values are proportionately considered in the optimization depending on their steady-state value. With this method, the dropout of any other component coupled in parallel to the system, such as parallel FACTS devices, capacitors, etc., can be described as well.

7.1.2 Modeling branch dropouts

The dropout of a branch presents a structural change in the system. In the state-space representation of the system, this would mean that the system matrices change, while the system inputs remain the same, which is challenging to consider in optimization. For this reason, we reformulate the power line dropout as a change in the system input.

We explain the modeling of a branch dropout on the example of a power line. We consider the failure of a power line between buses m and n , and propose to replace the power line with two constant power infeeds. These infeeds have the powers P_{plm} , Q_{plm} , and P_{pln} , Q_{pln} . They correspond to the power infeed at $t = t_0$ in buses m and n , respectively, of the power line which they replace, see Fig. 7.3 for an illustration. Doing so, the steady state of the system does not change. Thus it allows to keep the state-matrices of the system unchanged before and after the power line dropout. Basically, the dropout of a power line is converted to an equivalent load step in the system, and in the optimization we work with a system which does not contain the power line. The dropout of any component connected in series to the power system, such as a transformer or series capacitor etc., can be considered similarly. Thus, active and reactive power infeeds of the power line at $t = t_0$ are defined as disturbance inputs: P_{plm} , Q_{plm} , P_{pln} , Q_{pln} .

Remark 3 Note that the magnitudes of P_{plm} and P_{pln} , as well as of Q_{plm} and Q_{pln} , are not the same due to power line losses. The system frequency in steady-state after the dropout also changes by a small amount due to different electric losses in the rest of the system. This is handled on a slower time scale by the secondary controller in the system.

Since the inputs are not independent, i.e. after a power line dropout they change

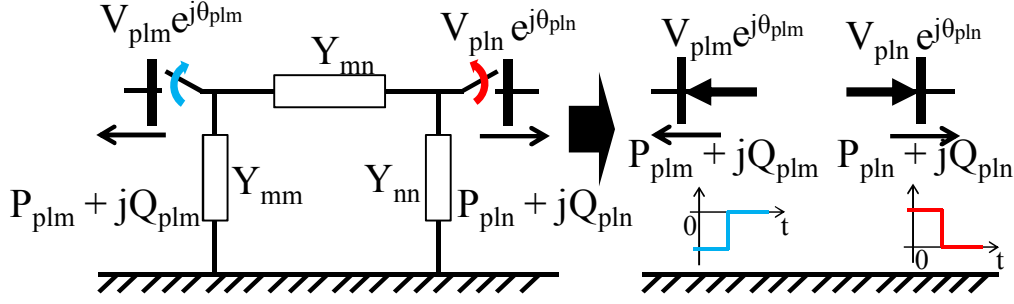


Figure 7.3: A graphical representation of the proposed modeling of power line which drop out from the system. The power line, whose dropout is considered, is replaced with two constant power infeeds with the same power as the power line.

simultaneously to zero, we model them as a single input/disturbance. The values of the active and reactive power which flow through the power line can have significantly different values. Consequently, we introduce weighting factors for the different inputs: α_{Pplm} , α_{Ppln} , α_{Qplm} , and α_{Qpln} , which are defined as

$$\sigma_{pl} = |P_{plm}| + |P_{pln}| + |Q_{plm}| + |Q_{pln}| \quad (7.3)$$

$$\alpha_{Pplm} = P_{plm}/\sigma_{pl} \quad \alpha_{Ppln} = P_{pln}/\sigma_{pl} \quad (7.4)$$

$$\alpha_{Qplm} = Q_{plm}/\sigma_{pl} \quad \alpha_{Qpln} = Q_{pln}/\sigma_{pl}. \quad (7.5)$$

The resulting disturbance input for the dropout of a power line is defined as

$$\mathbf{w}_{pl} = \begin{pmatrix} P_{plm} \\ Q_{plm} \\ P_{pln} \\ Q_{pln} \end{pmatrix} = \begin{pmatrix} \alpha_{Pplm} \\ \alpha_{Qplm} \\ \alpha_{Ppln} \\ \alpha_{Qpln} \end{pmatrix} \sigma_{pl}. \quad (7.6)$$

Analogously as for the power plant dropout, the normalization ensures that the values are proportionately considered in the optimization, depending on their steady-state value.

7.1.3 Modeling of dropouts of several components

The modeling of dropouts of one dynamic prosumer or branch element requires structural changes in the system matrices, compared to the initial system. Consequently, when several dropouts are considered, as is usual in the case for power system analysis, separate models are needed for each dropout. If n_s contingencies are considered, corresponding to different scenarios, then n_s models G_κ are needed, which describe one dropout

$$G_\kappa(\mathbf{K}, s) = C_\kappa(\mathbf{K})(sI - A_\kappa(\mathbf{K}))^{-1}B_\kappa(\mathbf{K}) + D_\kappa(\mathbf{K}), \quad \kappa = 1 \dots n_s. \quad (7.7)$$

These models are used for the subsequently described multi-scenario controller synthesis procedure.

7.2 Multi-scenario structured \mathcal{H}_∞ synthesis

We expand our tuning methods to the case of multiple scenarios. To do so, we propose to consider the following synthesis problem

$$\min_{\Gamma \in \mathbb{R}, \mathbf{K} \in \mathbb{N}^{R_t \times R_t}} \Gamma \quad (7.8a)$$

$$\text{s.t.} \quad \|G_\kappa(\mathbf{K}, s)\|_\infty \leq \Gamma, \kappa = 1, \dots, n_s \quad (7.8b)$$

$$\underline{\mathbf{K}} \leq \mathbf{K} \leq \overline{\mathbf{K}}. \quad (7.8c)$$

Basically Γ represents the worst-case \mathcal{H}_∞ norm for all considered scenarios. Our goal is to obtain one controller parameterization which minimizes the worst-case \mathcal{H}_∞ norm for all G_κ , $\kappa = 1 \dots n_s$. To do so, we extend both proposed methods towards multi-scenario optimization. Furthermore, an exemplary multi-scenario controller synthesis is shown in Section 7.3.

7.2.1 Extension of the Bounded real lemma method

For multi-scenario optimization, we propose extend (3.2) to

$$\min_{P_\kappa, \mathbf{K}, \Gamma} \Gamma \quad (7.9a)$$

$$\text{s.t.} \quad M_\kappa(\Gamma, \mathbf{K}, P_\kappa) := \begin{pmatrix} A_\kappa(\mathbf{K})^T P_\kappa + P_\kappa A_\kappa(\mathbf{K}) & P_\kappa B_\kappa(\mathbf{K}) & C_\kappa(\mathbf{K})^T \\ B_\kappa(\mathbf{K})^T P_\kappa & -\Gamma I & D_\kappa(\mathbf{K})^T \\ C_\kappa(\mathbf{K}) & D_\kappa(\mathbf{K}) & -\Gamma I \end{pmatrix} \prec 0 \quad (7.9b)$$

$$P_\kappa = P_\kappa^T \succ 0, \quad \kappa = 1 \dots n_s \quad (7.9c)$$

$$\underline{\mathbf{K}} \leq \mathbf{K} \leq \overline{\mathbf{K}}, \quad (7.9d)$$

where $P_\kappa \in \mathbb{R}^{N_{x,\kappa} \times N_{x,\kappa}}$ is the Lyapunov matrix for scenario κ , $N_{x,\kappa}$ is the number of states in scenario κ , $\mathbf{K} \in \mathbb{R}^{N_t}$ is the vector of tunable parameters for all scenarios, with the length N_t , and $\Gamma \in \mathbb{R}$ represents the worst-case \mathcal{H}_∞ norm of all scenarios. The solution of (7.9) is a controller parameterization which guarantees the stability of every scenario G_κ , thereby minimizing the worst-case \mathcal{H}_∞ norm of all scenarios. It can be solved analogously as Problem (3.2) with an iterative coordinate descent approach, c.f. Algorithm 1. Thereby, in the P-step of the μ -th iteration, when \mathbf{K} is set to $\mathbf{K}^{(\mu-1)}$,

the following optimization problem is solved

$$\min_{P_\kappa^{(\mu)}, \Gamma} \Gamma \quad (7.10a)$$

$$\text{s.t. } M_\kappa(\Gamma, \mathbf{K}^{(\mu-1)}, P_\kappa^{(\mu)}) \prec 0 \quad (7.10b)$$

$$P_\kappa^{(\mu)} = (P_\kappa^{(\mu)})^T \succ 0, \quad (7.10c)$$

$$\kappa = 1 \dots n_s, \quad (7.10d)$$

Problem (7.10) can be separated into n_s optimization problems

$$\min_{P_\kappa^{(\mu)}, \gamma_\kappa} \gamma_\kappa \quad (7.11a)$$

$$\text{s.t. } M_\kappa(\gamma_\kappa, \mathbf{K}^{(\mu-1)}, P_\kappa^{(\mu)}) \prec 0 \quad (7.11b)$$

$$P_\kappa^{(\mu)} = (P_\kappa^{(\mu)})^T \succ 0, \quad (7.11c)$$

which can be solved in parallel to speed-up the computations. Other steps of the solution procedure are analogous as in Algorithm 1. An analogous extension can be made for multi-scenario stabilization via LMIs by considering the LMI problem (3.7)

$$\min_{P_\kappa, \mathbf{K}, \Gamma} \Gamma \quad (7.12a)$$

$$\text{s.t. } A_\kappa(\mathbf{K})^T P_\kappa + P_\kappa A_\kappa(\mathbf{K}) \prec 0 \quad (7.12b)$$

$$P_\kappa = P_\kappa^T \succ 0, \quad \kappa = 1 \dots n_s \quad (7.12c)$$

$$\underline{\mathbf{K}} \leq \mathbf{K} \leq \overline{\mathbf{K}}. \quad (7.12d)$$

This method is used for the multi-scenario stabilization considered in Section 7.3. As one can see, the extensions are easy, however might result in significantly increased computation.

7.2.2 Extension of the frequency-sampling method

The frequency sampling method (3.19) can also be readily extended for the multi-scenario case as

$$\min_{\Gamma, \mathbf{K}} \Gamma \quad (7.13a)$$

$$\text{s.t. } \begin{pmatrix} \Gamma I & G_\kappa(\mathbf{K}, j\omega_{k,\kappa}) \\ G_\kappa(\mathbf{K}, j\omega_{k,\kappa})^* & \Gamma I \end{pmatrix} \succ 0, \quad \forall \omega_{k,\kappa} \in \Omega_\kappa \quad (7.13b)$$

$$\underline{\mathbf{K}} \leq \mathbf{K} \leq \overline{\mathbf{K}}. \quad (7.13c)$$

Here Ω_κ is defined for every scenario in order to adapt the frequency grid to the scenarios. Problem (7.13) can be solved with an analogous algorithm as the previously presented Algorithm 2. If the initial parameterization is stabilizing, the optimized

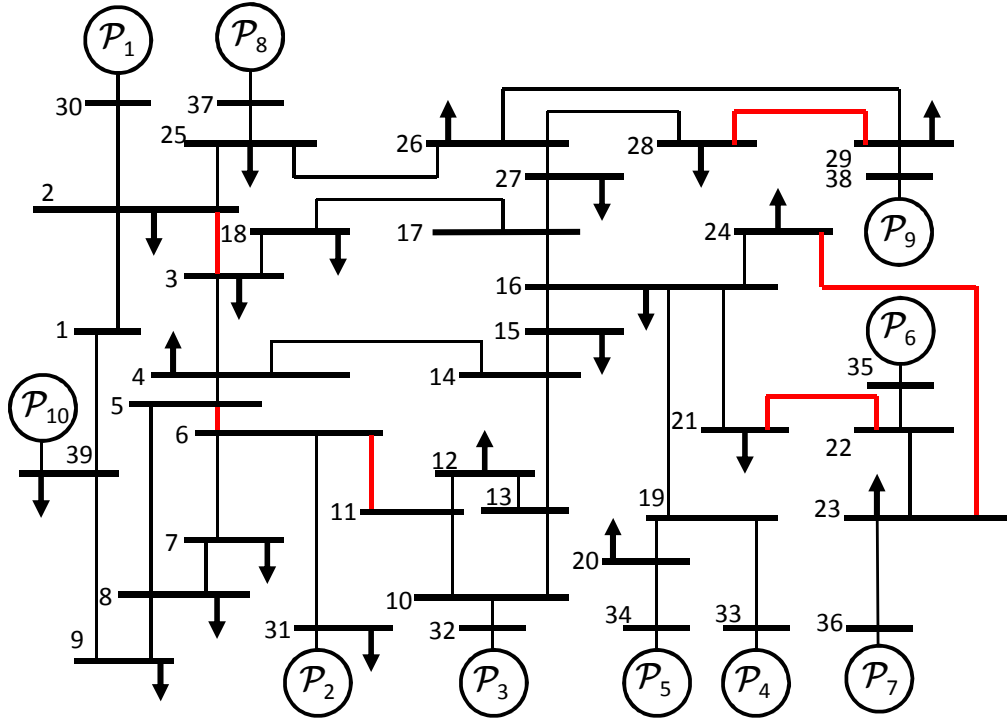
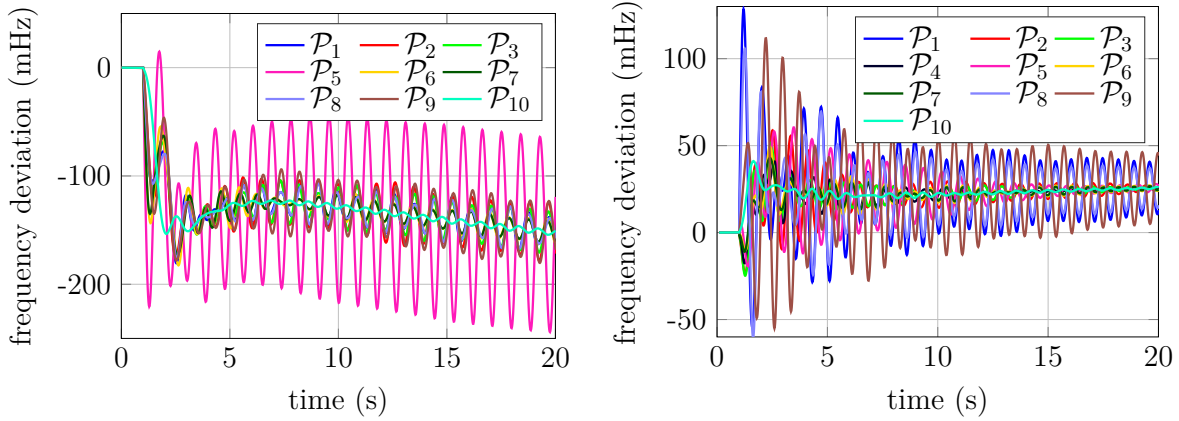


Figure 7.4: The considered IEEE 39 bus power system, c.f. Appendix. C.1. Power lines, considered for the dynamic security optimization, are marked in red. Additionally, the failure of every dynamic prosumer is considered for the dynamic security optimization.

parameterization will minimize the worst-case \mathcal{H}_∞ norm of all systems, while keeping all other systems stable.

7.3 Improvement of the dynamic security for the IEEE 39 bus power system

To demonstrate the effectiveness of the proposed controller tuning towards dynamic security, we consider the IEEE 39 bus system, shown in Fig 7.4, c.f. Appendix C.1. We consider the (separate) failure of each of the 10 dynamic prosumers (power plants), as well as the failure of six power lines. We have chosen power lines with the greatest power flow, such that they do not create asynchronous islands after the failure and that they are geographically distributed across the grid. Consequently, we consider failures of the power lines between buses 2 and 3, 5 and 6, 6 and 11, 21 and 22, 23 and 24, as well as 28 and 29, marked red in Fig. 7.4. The system response to the failure of the dynamic prosumer \mathcal{P}_4 with the initial parameterization is shown in Fig. 7.5(a), whereas the system response to the failure of the power line between buses 2 and 3 is shown in Fig. 7.5(b). In both cases, the resulting oscillations are poorly damped, and in the case of the \mathcal{P}_4 failure, the system even becomes unstable. All simulations are performed in Simscape Power Systems [68] using the full nonlinear



(a) Increasing oscillations, which occur after the drop out of \mathcal{P}_4 . Note that the system becomes unstable.

(b) Oscillations in the system which occur after the drop out of the power line between the buses 2 and 3.

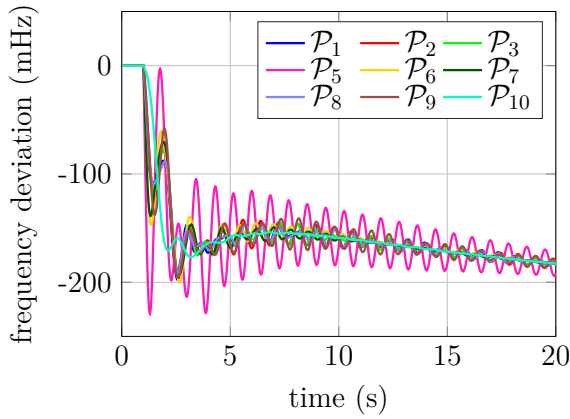
Figure 7.5: Response of the IEEE 39 bus system for the initial parameters \mathbf{K}_{init} for two contingencies.

power system model. Using the outlined modeling approach, we obtain 16 models for the 16 considered contingencies. For the parameter tuning, we use the approach for multi-scenario tuning presented in Subsection 7.2.1. Since the system may be unstable after a contingency with the initial controller parameterization, the tuning is done in two stages: first the controller parameters are tuned to obtain a stable system after the failure of critical prosumers and/or power lines. Then, the parameters are tuned in order to better dampen oscillation occurring after the failure of these components.

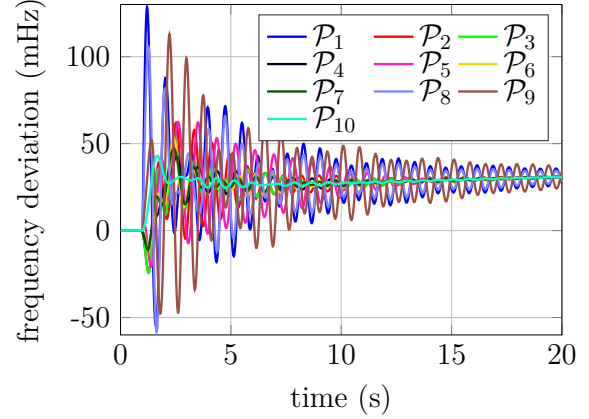
The multi-scenario stabilization is performed with the matrix-inequality approach (7.12), where the proposed iterative coordinate descent method from Section 3.1 is used to solve it. With this procedure, the stabilizing parameter set \mathbf{K}_{stab} is obtained. Figure 7.6 shows the time-response of the system to two selected contingencies with \mathbf{K}_{stab} . The system is successfully stabilized for the failure of each considered component. However, badly damped oscillations are still present in the system.

To further improve oscillation damping in the post-contingency systems, we perform the multi-scenario \mathcal{H}_∞ controller tuning described in Section 3.1, resulting in the parameter set \mathbf{K}_{opt} . Figure 7.7 shows the time-response of the system to the two selected contingencies with \mathbf{K}_{opt} . Compared to Figs. 7.5 and 7.6, the oscillation damping is significantly improved, and the settling time is reduced to approximately 7 seconds for both contingencies.

This section showed the applicability of parameter tuning to increase dynamic security of power systems. To decrease the total computation time, it is e.g. also possible to perform the \mathcal{H}_∞ tuning only for the nominal system, i.e. with no contingencies, with the stability requirements for each system with a contingency. Then, if a contingency occurs, there is sufficient time to reparameterize the prosumers again.

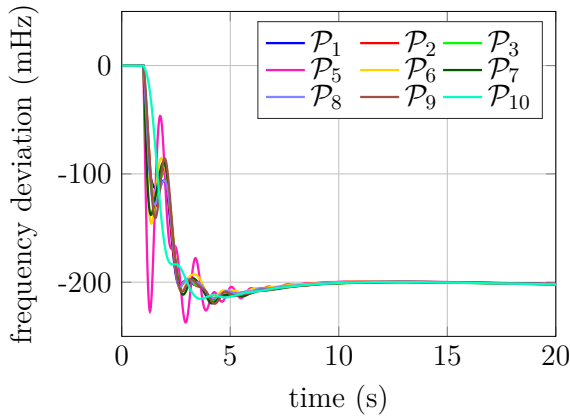


(a) Oscillations in the system which occur after the drop out of \mathcal{P}_4 .

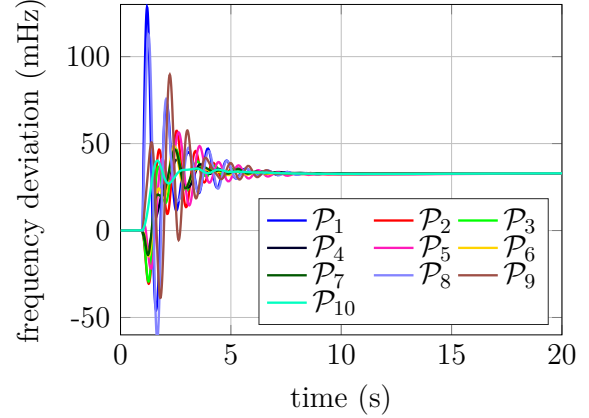


(b) Oscillations in the system which occur after the drop out of the power line between buses 2 and 3.

Figure 7.6: Response of the IEEE 39 bus system with the stabilizing parameters \mathbf{K}_{stab} for two contingencies.



(a) Oscillations in the system which occur after the drop out of \mathcal{P}_4 .



(b) Oscillations in the system which occur after the drop out of the power line between buses 2 and 3.

Figure 7.7: Response of the IEEE 39 bus system with the optimal parameters \mathbf{K}_{opt} for two contingencies.

7.4 Summary

In this chapter, we extended the proposed controller tuning methods towards multiple scenarios and applied them to increase the dynamic security of an exemplary power system. For this purpose, we first modeled contingencies in power systems, such that they can be used within the \mathcal{H}_∞ controller synthesis framework. Then, we presented the extensions of the controller synthesis methods and applied them to a numerical example. The proposed approach successfully stabilized the system, and significantly improved its performance after every contingency.

8 Scalable and Data Privacy Conserving Controller Tuning for Large-Scale Networks

Interconnecting electric power transmission systems has many widely recognized advantages, compared to isolated operation of smaller power systems. These include increased system resiliency, i.e. the ability of the system to withstand larger disturbances, cheaper operation, and reduced frequency variations [51]. Over the last decades, smaller power systems have been intensively coupled. This has led to large systems such as the European grid or the Western Interconnection in the USA. Such systems often consist of hundreds of interconnected subsystems, managed by different subsystem operators. Each subsystem can consist of many different components, such as power plants, wind turbines, households and charging stations, which are interconnected by a power grid, c.f. Fig. 8.1.

The controller tuning approaches presented so far show good results in the considered simulation studies and the testbed system, while requiring reasonable computation times. However, the tuning requires the knowledge of the complete system model and state, rendering their application for large power systems impossible due to several reasons. First, large power systems can have thousands of prosumers and controller parameters, which cannot be handled by the proposed centralized tuning approaches. Second, large power systems belong to multiple (sub)system operators, which cannot share detailed parameters and models of their (sub)systems, as this could expose user information as well as critical vulnerabilities to others. Due to these concerns, a decentralized approach is introduced in this chapter, which does not rely on

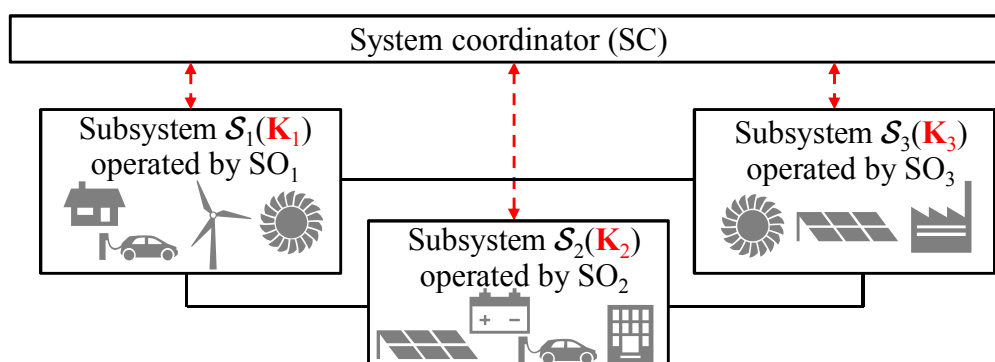


Figure 8.1: Simple power system example consisting of three interconnected subsystems belonging to different subsystem operators (SOs). Physical connections, i.e. power lines, are denoted with solid lines, whereas (slow) communication links are denoted with dashed lines.

a detailed model of the entire power system. This approach scales to larger systems than the centralized tuning, making it better suitable for optimization of large power systems. Furthermore, a centralized detailed model of the power system is not needed, leading to increased data privacy. The proposed method is based on the exchange of structured reduced models of subsystems, which conserves data privacy and reduces computational complexity. For this purpose, suitable methods for model reduction and model matching are introduced. A general description of the proposed approach, together with the adaptation of the power system model for hierarchical tuning, is presented in Section 8.1. Then, details of the approach are described in Section 8.2. Finally, the chapter is concluded with the evaluation of the hierarchical tuning on two numerical examples in Sections 8.3 and 8.4.

8.1 Controller tuning problem for large power systems

Figure 8.1 shows an exemplary power system, consisting of three subsystems $\mathcal{S}_1 - \mathcal{S}_3$. The subsystems are owned by the subsystems operators (SOs). Each subsystem \mathcal{S}_i contains controllers with tunable parameters, which are collected in parameter vectors \mathbf{K}_i , marked red in Fig. 8.1. The SOs communicate with the system coordinator (SC). For example, in Europe, the European Network of Transmission System Operators for Electricity (ENTSOE) could be the system coordinator.

Depending on the infeed of renewable generation and load, the system dynamic behavior changes. In the proposed approach, if the SC or SOs notice that the resiliency of the system decreases, they start the tuning procedure for the controller parameters in the subsystems \mathbf{K}_i . In the proposed hierarchical parameter tuning concept, the SOs only exchange information with the SC, which does not reveal detailed information about each subsystem. The reparameterization process is depicted with red dashed lines in Fig. 8.1. Thereby, only slow communication is needed and limited information exchange. Before explaining the hierarchical tuning procedure in depth in Section 8.2, we outline the solution approach, as well as the used dynamic models.

8.1.1 Outline of the proposed hierarchical controller tuning approach

In order to improve the readability of subsequent sections, we outline the main idea of the proposed approach, without mathematical details. The complete approach is presented in Section 8.2.

We consider systems consisting of a number of subsystems \mathcal{S}_i , c.f. Fig. 8.1. Each \mathcal{S}_i is operated by an SO_i , who might not be willing to exchange detailed information about its subsystem with others. The subsystems are coordinated through a system coordinator (SC). Figure 8.2 outlines the proposed iterative controller tuning approach, consisting of three steps. In the first step, each SO reduces its subsystem model, hiding thereby the detailed dynamics and parameters inside the reduced model, leading to

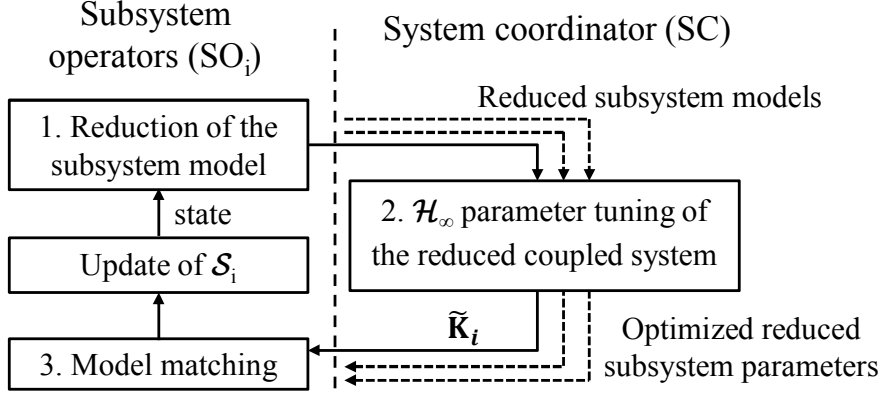


Figure 8.2: Outline of the proposed hierarchical optimization approach.

increased information security. The reduced model typically has a reduced number of controller parameters for tuning. The reduced subsystem models are sent to the SC. The SC combines the reduced subsystem models and tunes the parameters of the resulting reduced overall system. This allows to reduce the computational complexity of the parameter tuning process. The SC sends the optimized reduced parameters of the subsystems back to the SCs. They optimize the parameters of the detailed subsystems to match the reduced models as good as possible, concluding one iteration of the approach. The process is repeated until a satisfactory performance is achieved.

In summary, the increase of data security and reduction of computational complexity is achieved by model reduction in the proposed approach. This, however, leads to a series of challenges which are addressed in more detail in Section 8.2.

8.1.2 Modeling of the subsystems

Figure 8.3 shows an exemplary subsystem \mathcal{S}_i . Each subsystem consists of heterogeneous components, such as power plants, renewable generation, storage systems and households, interconnected by a power grid, detailed in Section 2.1. We introduce in this chapter a notation with two subindices, where the first subindex denotes the i -th subsystem \mathcal{S}_i , and the second subindex denotes the j -th component in \mathcal{S}_i , e.g. \mathcal{P}_{ij} . However, compared to the previously defined models in Section 2.1, the model of \mathcal{S}_i has additional coupling inputs \mathbf{w}_{ci} and outputs \mathbf{y}_{ci} . The coupling between the subsystems is represented through the inputs \mathbf{P}_{cpi} and \mathbf{Q}_{cpi} . They denote the active and reactive powers, respectively, due to the coupling between the \mathcal{S}_i 's. The coupling outputs are the magnitudes \mathbf{V}_{cpi} and angles $\boldsymbol{\theta}_{cpi}$ of the voltage phasors on the border buses (nodes), which are connected through power lines to the other subsystems. We refer to \mathbf{P}_{cpi} and \mathbf{Q}_{cpi} as the coupling input \mathbf{w}_{ci} of \mathcal{S}_i , whereas \mathbf{V}_{cpi} and $\boldsymbol{\theta}_{cpi}$ are the coupling output \mathbf{y}_{ci} . Both are marked orange in Fig. 8.3. Each subsystem can be coupled to other subsystems, i.e. they can have multiple coupling inputs and multiple coupling outputs.

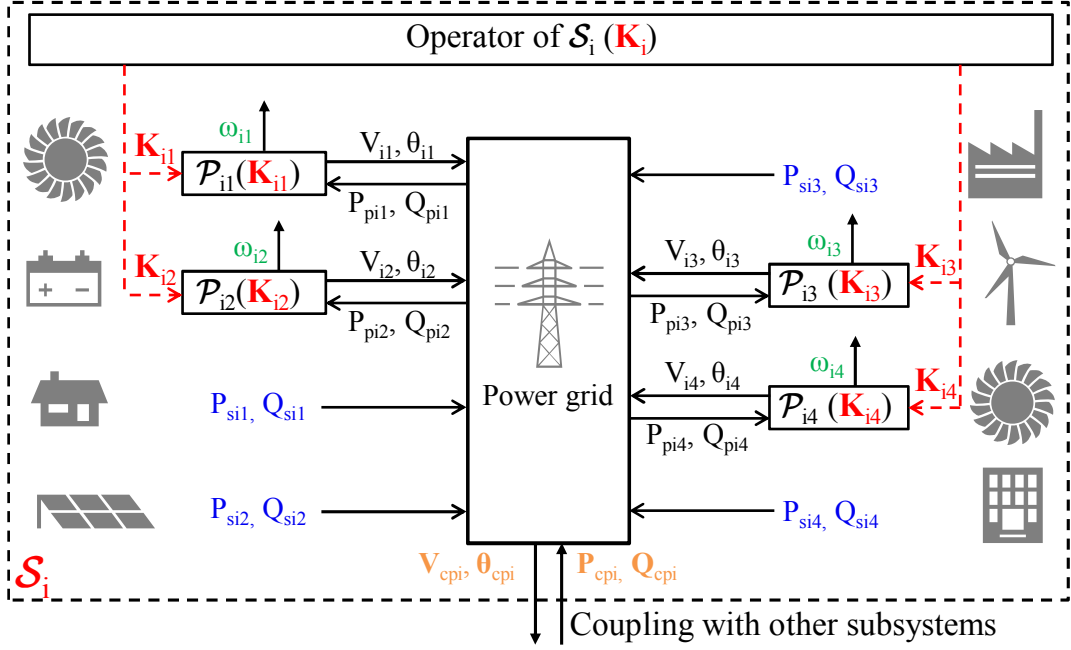


Figure 8.3: Example subsystem \mathcal{S}_i , operated by the operator SO_i . It consists of four dynamic prosumers \mathcal{P}_{ij} and four static prosumers with power infeeds P_{sij} and Q_{sij} . The system operator periodically tunes the controller parameters $\mathbf{K}_i = \text{vec}_j(\mathbf{K}_{ij})$ of the dynamic prosumers, marked red, in order to increase resiliency in the system. The static prosumers, whose infeed is marked with blue, are considered as a disturbance input into the system. The frequencies ω_{ij} of \mathcal{P}_{ij} , marked green, are used as a part of the performance output of the subsystem. The coupling with other subsystems is realized through the input \mathbf{P}_{cpi} , \mathbf{Q}_{cpi} and output \mathbf{V}_{cpi} , $\boldsymbol{\theta}_{cpi}$, marked orange.

Performance outputs for the controller tuning. Performance outputs are used in the controller tuning procedure to define an objectively quantifiable tuning goal. In power systems, the frequencies of dynamic prosumers ω_{ij} are typically used to assess the system performance [51]. They are defined by $\omega_{ij} = \dot{\theta}_{ij}$, where θ_{ij} is the angle of the voltage phasor of \mathcal{P}_{ij} , marked green in Fig. 8.3. Consequently, we choose the vector of all frequencies (or a subset) as a performance output, analogously as in Chapter 2

$$\boldsymbol{\omega}_i = (\omega_{i1} \quad \dots \quad \omega_{iN_{Di}})^T, \quad (8.1)$$

where N_{Di} is the number of dynamic prosumers in \mathcal{S}_i . When oscillations between subsystems are considered, prosumers in one subsystem oscillate against prosumers of other subsystems. Thus, choosing the so-called center-of-inertia frequency [112] as the performance output for one subsystem is a standard choice when oscillations between subsystems should be suppressed

$$\omega_{COIi} = \frac{\sum_{j=1}^{N_{Di}} J_{ij} \omega_{ij}}{\sum_{j=1}^{N_{Di}} J_{ij}}. \quad (8.2)$$

Here J_{ij} is the inertia of the j -th dynamic prosumer. The center-of-inertia frequency represents the weighted arithmetical mean of all generator frequencies.

Model of subsystem \mathcal{S}_i . Analogously as in Section 2.1, the dynamical model of \mathcal{S}_i is given by a differential-algebraic nonlinear model

$$\dot{\mathbf{x}}_i = f_i(\mathbf{x}_i, \mathbf{w}_{si}, \mathbf{w}_{ci}, \mathbf{K}_i) \quad (8.3a)$$

$$0 = h_i(\mathbf{x}_i, \mathbf{w}_{si}, \mathbf{w}_{ci}, \mathbf{K}_i), \quad (8.3b)$$

Here $\mathbf{x}_i \in \mathbb{R}^{N_{xi}}$ combines all dynamic prosumer states of \mathcal{S}_i , \mathbf{w}_{si} is the vector of inputs from static prosumers in \mathcal{S}_i , represented by a subset of \mathbf{P}_{si} and \mathbf{Q}_{si} , $\mathbf{w}_{ci} \in \mathbb{R}^{n_{ci}}$ is the vector of coupling inputs, represented by \mathbf{P}_{cpi} and \mathbf{Q}_{cpi} , $\mathbf{K}_i \in \mathbb{R}^{N_{ki}}$ is the vector of tunable controller parameters of all dynamic prosumers in \mathcal{S}_i , f_i describes the prosumer dynamics in \mathcal{S}_i , and h_i represents the power flow equations in \mathcal{S}_i . All considered outputs of (8.3) are linear combinations of the elements in \mathbf{x}_i .

Analogously as in Section 2.1, (8.3) is linearized and the zero-eigenvalue is eliminated, leading to

$$\dot{\mathbf{x}}_i = A_i(\mathbf{K}_i)\mathbf{x}_i + B_{ci}(\mathbf{K}_i)\mathbf{w}_{ci} + B_{si}(\mathbf{K}_i)\mathbf{w}_{si}. \quad (8.4)$$

The proposed approach is based on different transfer functions, for which we need to define the outputs of interest, c.f. Fig. 8.2. First, a transfer function is needed for each subsystem which couples the disturbance and coupling inputs \mathbf{w}_{ci} , \mathbf{w}_{si} and outputs $\mathbf{y}_{ci} = (\mathbf{V}_{cpi}^T \quad \boldsymbol{\theta}_{cpi}^T)^T$, $\mathbf{y}_{pi} = \omega_{COIi}$, defined as

$$\begin{pmatrix} \mathbf{y}_{ci} \\ \mathbf{y}_{pi} \end{pmatrix} = G_i(\mathbf{K}_i, s) \begin{pmatrix} \mathbf{w}_{ci} \\ \mathbf{w}_{si} \end{pmatrix} = \begin{pmatrix} G_{cci}(\mathbf{K}_i, s) & G_{csi}(\mathbf{K}_i, s) \\ G_{pci}(\mathbf{K}_i, s) & G_{psi}(\mathbf{K}_i, s) \end{pmatrix} \begin{pmatrix} \mathbf{w}_{ci} \\ \mathbf{w}_{si} \end{pmatrix}. \quad (8.5)$$

The transfer function $G_{csi}(\mathbf{K}_i, s)$ represents algebraic power flow equations which couple the power of static prosumers \mathbf{w}_{si} with the coupling output \mathbf{y}_{ci} . Thus, $G_{csi}(\mathbf{K}_i, s)$ is not a function of controller parameters and is written as a constant matrix, i.e. $G_{csi}(\mathbf{K}_i, s) = M_{si}$.

The second transfer function, $G_i^*(\mathbf{K}_i, s)$, is used for the \mathcal{H}_∞ controller tuning, see Fig. 8.2. For this purpose, the vector of all dynamic prosumer frequencies is defined as the performance output, described with (8.1). We consider \mathbf{w}_{ci} and \mathbf{w}_{si} as disturbance inputs, because disturbances can come from other subsystems through the coupling input, as well as from internal static prosumers. Thereby, if \mathcal{S}_i is not coupled with other systems, i.e. if \mathcal{S}_i represents an isolated system, the vector \mathbf{w}_{ci} is empty. Thus, $G_i^*(\mathbf{K}_i, s)$ is in this case given by

$$\mathbf{y}_{pi}^* = \boldsymbol{\omega}_i = G_i^*(\mathbf{K}_i, s) \begin{pmatrix} \mathbf{w}_{ci} \\ \mathbf{w}_{si} \end{pmatrix}, \quad (8.6)$$

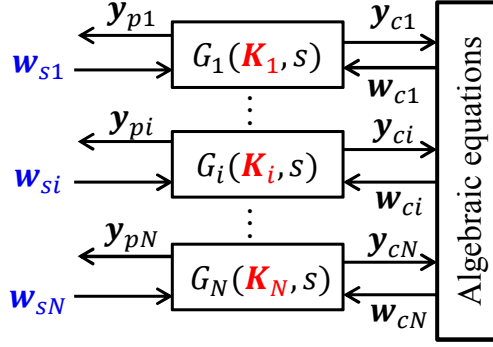


Figure 8.4: Coupled power system model consisting of N subsystems \mathcal{S}_i . The vector \mathbf{w}_s is the disturbance input, representing aggregated static prosumers in the system, i.e. $\mathbf{w}_s = \text{vec}_i(\mathbf{w}_{si})$.

Further details on the use of the transfer functions can be found in Section 8.2.

8.1.3 Coupled power system model

The previous subsection outlined the modeling and structure for a single \mathcal{S}_i . We now outline how the subsystems are coupled to obtain the model of the entire power system. Physically, the subsystems are coupled via power lines, which we model using linearized algebraic power flow equations, c.f. Fig. 8.4. The coupling between the subsystems is given by

$$\mathbf{w}_c = M\mathbf{y}_c, \quad (8.7)$$

where $\mathbf{w}_c = \text{vec}_i(\mathbf{w}_{ci})$, $\mathbf{y}_c = \text{vec}_i(\mathbf{y}_{ci})$, and M represents the linearized coupling between the subsystems and is a full-rank matrix. The transfer function of the coupled system, i.e. $G(\mathbf{K}, s)$, from the disturbance input $\mathbf{w}_s = \text{vec}_i(\mathbf{w}_{si})$ to the performance output $\mathbf{y}_p = \text{vec}_i(\mathbf{y}_{pi})$, which quantifies oscillations between subsystems, is obtained by combining (8.7) with G_{ci} and G_{pi} in (8.5)

$$G(\mathbf{K}, s) = \text{bd}_i(G_{psi}(\mathbf{K}_i, s)) + \text{bd}_i(G_{pci}(\mathbf{K}_i, s)) (I - M\text{bd}_i(G_{cci}(\mathbf{K}_i, s)))^{-1} M\text{bd}_i(M_{si}) \quad (8.8)$$

where $\mathbf{K} = \text{vec}_i(\mathbf{K}_i)$. The transfer function $G(\mathbf{K}, s)$ has several challenging properties: (1) The dependency of G on \mathbf{K} is nonlinear, (2) the coupled system can be very large with thousands of states, (3) no single entity knows the parameters and detailed structure of $G(\mathbf{K}, s)$. Only the SO of \mathcal{S}_i is aware of all parameters of $G_i(\mathbf{K}_i, s)$. The SC knows only the parameters of the coupling matrix M .

Given this setup, we can formulate the main research question considered in this chapter: what are the optimal parameters \mathbf{K} to minimize the \mathcal{H}_∞ norm of $G(\mathbf{K}, s)$?

8.2 Hierarchical parameter tuning

As outlined previously, centralized tuning is often undesired or not possible. Thus, we introduce in this Section a hierarchical decentralized tuning approach. The hierarchical tuning is based on the ideas sketched in Fig. 8.2. To allow scalability and to increase privacy, we propose the following steps in the k -th iteration of the algorithm, compare also Fig. 8.5:

1. Model reduction of the subsystems: all SOs first calculate a reduced model of their subsystem, denoted with $\widetilde{G}_i^{(k)}(\widetilde{\mathbf{K}}_{i,init}^{(k)}, s)$, based on the detailed model $G_i(\mathbf{K}_{i,init}^{(k)}, s)$, which is defined in (8.5). Here \widetilde{G}_i and $\widetilde{\mathbf{K}}_i$ denote the reduced model of \mathcal{S}_i and its parameter vector, respectively, and (k) denotes the iteration. The detailed parameters and dynamics of the individual prosumers and of the power grid are "hidden" in \widetilde{G}_i and $\widetilde{\mathbf{K}}_i$, which leads to increased data privacy. The SOs send $\widetilde{G}_i^{(k)}$ and $\widetilde{\mathbf{K}}_{i,init}^{(k)}$ to the SC.
2. Centralized \mathcal{H}_∞ parameter tuning based on the reduced subsystem models: the system coordinator (SC) couples the reduced subsystems and calculates a reduced model of the whole system $\widetilde{G}^{(k)}(\widetilde{\mathbf{K}}, s)$. It optimizes the reduced system, which has a smaller complexity than an overall detailed model capturing the detailed dynamics of all subsystems. The optimized reduced set of parameters $\widetilde{\mathbf{K}}_{i,opt}^{(k)}$ are sent back to the SOs.
3. Model matching: The optimized reduced subsystems $\widetilde{G}_i^{(k)}(\widetilde{\mathbf{K}}_{i,opt}^{(k)}, s)$ serve as a reference model for the SOs. They optimize the parameters of their respective detailed models $G_i(\mathbf{K}_i, s)$ to match the reference model to the best possible extent.

This iterative process is performed repeatedly until a stopping criterion is fulfilled. Step 2, i.e. the optimization step based on the reduced models, contains the main idea of the approach: instead of optimizing the entire detailed system, the SC uses the reduced models, leading to improved data privacy and scalability of the approach. However, the optimization of reduced models introduces challenges with respect to the model reduction and model matching steps. In general, $\widetilde{\mathbf{K}}_{i,init}^{(k)}$ is not the same as $\widetilde{\mathbf{K}}_{i,opt}^{(k-1)}$, as $\widetilde{\mathbf{K}}_{i,init}^{(k)}$ is obtained from the model reduction step.

In the next sections we provide details for each step of the approach. We start with the optimization step in order to better clarify the main idea of the approach. Afterwards, we detail the model matching step before turning to the model reduction step, which is detailed last as the requirements are derived from the optimization and model matching steps.

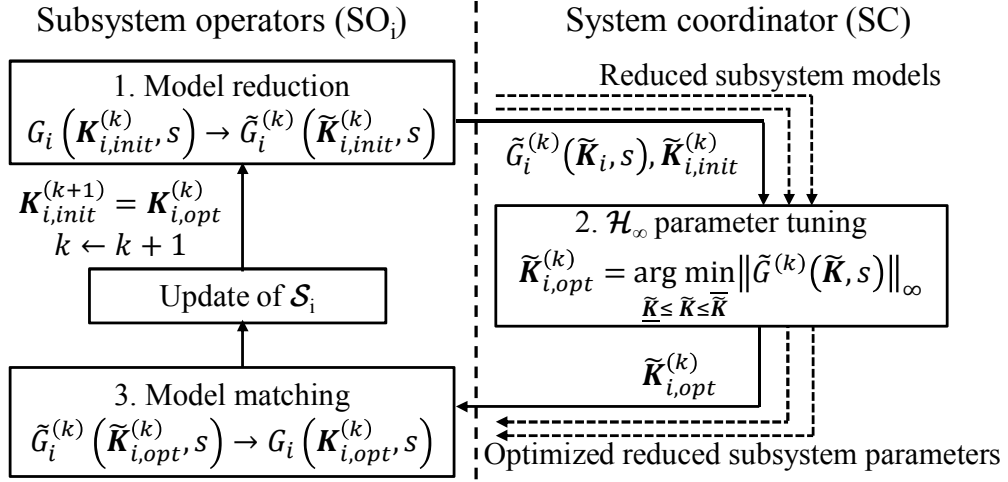


Figure 8.5: Details of the proposed optimization approach.

8.2.1 Structured \mathcal{H}_∞ parameter tuning of the reduced system

For the tuning, the SC receives reduced models of each subsystem, i.e. $\tilde{G}_i^{(k)}(\tilde{\mathbf{K}}_i, s)$, together with initial reduced parameter vectors $\tilde{\mathbf{K}}_{i,init}^{(k)}$ from each SO. As the SC knows the coupling matrix M , the overall reduced model can be formulated

$$\tilde{G}(\tilde{\mathbf{K}}, s) = \text{bd}_i(\tilde{G}_{psi}(\tilde{\mathbf{K}}_i, s)) + \text{bd}_i(\tilde{G}_{pci}(\tilde{\mathbf{K}}_i, s)) (I - M \text{bd}_i(\tilde{G}_{cci}(\tilde{\mathbf{K}}_i, s)))^{-1} M \text{bd}_i(M_{si}), \quad (8.9)$$

where $\text{bd}_i(M_{si})$ constructs a block-diagonal matrix consisting of matrices M_{si} , for all i . Based on this model, the SC performs the structured \mathcal{H}_∞ controller tuning

$$\tilde{\mathbf{K}}_{opt}^{(k)} = \text{vec}_i(\tilde{\mathbf{K}}_{i,opt}^{(k)}) = \arg \min_{\underline{\tilde{\mathbf{K}}} \leq \tilde{\mathbf{K}} \leq \overline{\tilde{\mathbf{K}}}} \|\tilde{G}(\tilde{\mathbf{K}}, j\omega)\|_\infty \quad (8.10)$$

with (3.19), where $\underline{\tilde{\mathbf{K}}}$ and $\overline{\tilde{\mathbf{K}}}$ are box constraints on the reduced vector of controller parameters. The optimization is initialized with $\tilde{\mathbf{K}}_{i,init}^{(k)} = \text{vec}_i(\mathbf{K}_{i,init}^{(k)})$. The optimized parameter vectors $\tilde{\mathbf{K}}_{i,opt}^{(k)}$ are sent to the SOs.

8.2.2 Model matching step

When the SO of the i -th subsystem receives the reduced optimized parameter vector $\tilde{\mathbf{K}}_{i,opt}^{(k)}$ from the SC, it uses $\tilde{G}_i^{(k)}(\tilde{\mathbf{K}}_{i,opt}^{(k)}, j\omega)$ as the reference model to adapt the parameters of the full subsystem, such that the detailed model best matches the optimized reduced model. The SO_i solves an \mathcal{H}_∞ model matching problem to obtain the vector of detailed controller parameters of \mathcal{S}_i in the k -th iteration

$$\mathbf{K}_{i,opt}^{(k)} = \arg \min_{\underline{\mathbf{K}}_i \leq \mathbf{K}_i \leq \overline{\mathbf{K}}_i} \left\| G_i(\mathbf{K}_i, j\omega) - \tilde{G}_i^{(k)}(\tilde{\mathbf{K}}_{i,opt}^{(k)}, j\omega) \right\|_\infty \quad (8.11)$$

where $\underline{\mathbf{K}}_i$ and $\overline{\mathbf{K}}_i$ represent box constraints on the controller parameters. From the solution of this problem, the optimized detailed parameter vector in the k -th iteration $\mathbf{K}_{i,opt}^{(k)}$ is obtained for each area. This parameter vector is used as the initial value for the model reduction for the next updated iteration.

8.2.3 Model reduction step

From the previous two steps, the following requirements for the reduced model $\widetilde{G}_i^{(k)}(\widetilde{\mathbf{K}}, j\omega)$ are evident:

1. The error between $\widetilde{G}_i^{(k)}(\widetilde{\mathbf{K}}_{i,init}^{(k)}, j\omega)$ and $G_i(\mathbf{K}_{i,init}^{(k)}, j\omega)$ should be small.
2. The reduced models need to have tunable parameters $\widetilde{\mathbf{K}}_i^{(k)}$ which can be optimized in the optimization step.
3. The \mathcal{H}_∞ error between $\widetilde{G}_i^{(k)}(\widetilde{\mathbf{K}}_{i,opt}^{(k)}, j\omega)$ and $G_i(\mathbf{K}_{i,opt}^{(k)}, j\omega)$ after the model matching step should be small. This means that the reduced model needs to have a representative, realistic dependency on the vector of reduced tunable parameters $\widetilde{\mathbf{K}}_i$, i.e. similar to the dependency of the detailed model on the full parameter vector \mathbf{K}_i .

Due to the second requirement, the application of unstructured model reduction approaches, such as balanced model order reduction, is difficult, as they do not retain parametric dependencies in the reduced model. This can be overcome, e.g., by introducing an additional static state-feedback controller for the reduced model whose parameters can be optimized. However, such a model may have very different dynamic properties after the optimization step, meaning that the model matching step may not allow to reduce the error between the detailed model and the reduced model, i.e. the third requirement may not be satisfied.

Instead, we propose to perform the model reduction step by selecting a structured reference model for one area. The reference model has a fixed structure and is parameterized to match the detailed model. Structured reduced models have been widely used in the power system community, replacing groups of interconnected power plants by a small number of power plants, see e.g. in [19]. Every SO obtains its reduced model \widetilde{G}_i by solving the following parameter matching problem

$$(\mathbf{R}_i^{(k)}, \widetilde{\mathbf{K}}_{i,init}^{(k)}) = \arg \min_{\substack{\underline{\mathbf{R}}_i \leq \mathbf{R}_i \leq \overline{\mathbf{R}}_i \\ \underline{\widetilde{\mathbf{K}}}_i \leq \widetilde{\mathbf{K}}_i \leq \overline{\widetilde{\mathbf{K}}}_i}} \left\| G'_i(\mathbf{R}_i, \widetilde{\mathbf{K}}_i, j\omega) - G_i(\mathbf{K}_{i,init}^{(k)}, j\omega) \right\|_\infty. \quad (8.12)$$

Here G'_i is the reduced model with the predefined structure, and \mathbf{R}_i is the vector of other model parameters. For power systems, \mathbf{R}_i can represent, for example, the

physical parameters of TGOV_{ij} , AVR_{ij} , and PSS_{ij} . The reduced model becomes

$$\widetilde{G}_i^{(k)}(\widetilde{\mathbf{K}}_i, j\omega) := G'_i(\mathbf{R}_i^{(k)}, \widetilde{\mathbf{K}}_i, j\omega). \quad (8.13)$$

The model reduction is outlined in detail in Section 8.3.3.

8.2.4 Condition for the improvement of the system \mathcal{H}_∞ norm

The minimization of $\|\widetilde{G}(\widetilde{\mathbf{K}}, j\omega)\|_\infty$ does not guarantee that $\|G(\mathbf{K}, j\omega)\|_\infty$ will be reduced per iteration. This can be captured by the following Lemma:

Lemma 4 $\|G(\mathbf{K}_{init}^{(k)}, s)\|_\infty$ is reduced if and only if

$$\max_{\omega \in \mathbb{R}} \epsilon_{opt}^{(k)}(\omega) - \epsilon_{init}^{(k)}(\omega) + \alpha^{(k)}(\omega) + \bar{\sigma}(G(\mathbf{K}_{init}^{(k)}, j\omega)) < \max_{\omega \in \mathbb{R}} \bar{\sigma}(G(\mathbf{K}_{init}^{(k)}, j\omega)). \quad (8.14)$$

Here $\epsilon_{init}^{(k)}(\omega)$ denotes the singular value error between the detailed model $G(\mathbf{K}_{init}^{(k)}, j\omega)$ and the reduced model $\widetilde{G}(\widetilde{\mathbf{K}}_{init}^{(k)}, j\omega)$ after the model reduction step

$$\epsilon_{init}^{(k)}(\omega) = \bar{\sigma}(G(\mathbf{K}_{init}^{(k)}, j\omega)) - \bar{\sigma}(\widetilde{G}(\widetilde{\mathbf{K}}_{init}^{(k)}, j\omega)). \quad (8.15)$$

Furthermore, $\epsilon_{opt}^{(k)}(\omega)$ is the error term which occurs after the model matching step between $\widetilde{G}(\widetilde{\mathbf{K}}_{opt}^{(k)}, j\omega)$ and $G(\mathbf{K}_{opt}^{(k)}, j\omega)$

$$\epsilon_{opt}^{(k)}(\omega) = \bar{\sigma}(G(\mathbf{K}_{opt}^{(k)}, j\omega)) - \bar{\sigma}(\widetilde{G}(\widetilde{\mathbf{K}}_{opt}^{(k)}, j\omega)), \quad (8.16)$$

and $\alpha^{(k)}(\omega)$ quantifies the change in the singular values of the reduced system during the parameter tuning in the k -th iteration

$$\alpha^{(k)}(\omega) = \bar{\sigma}(\widetilde{G}(\widetilde{\mathbf{K}}_{opt}^{(k)}, j\omega)) - \bar{\sigma}(\widetilde{G}(\widetilde{\mathbf{K}}_{init}^{(k)}, j\omega)). \quad (8.17)$$

Proof. Reduction of $\|G(\mathbf{K}_{init}^{(k)}, s)\|_\infty$ in an iteration is equivalent to the condition

$$\|G(\mathbf{K}_{opt}^{(k)}, j\omega)\|_\infty < \|G(\mathbf{K}_{init}^{(k)}, j\omega)\|_\infty \quad (8.18)$$

$$\Leftrightarrow \max_{\omega \in \mathbb{R}} \bar{\sigma}(G(\mathbf{K}_{opt}^{(k)}, j\omega)) < \max_{\omega \in \mathbb{R}} \bar{\sigma}(G(\mathbf{K}_{init}^{(k)}, j\omega)). \quad (8.19)$$

Combining Equations (8.15), (8.16), and (8.17), leads us to the following relation

$$\bar{\sigma}(G(\mathbf{K}_{opt}^{(k)}, j\omega)) = \epsilon_{opt}^{(k)}(\omega) + \alpha^{(k)}(\omega) - \epsilon_{init}^{(k)}(\omega) + \bar{\sigma}(G(\mathbf{K}_{init}^{(k)}, j\omega)). \quad (8.20)$$

Inserting (8.20) into (8.19), we obtain (8.14). ■

Note that $\alpha^{(k)}(\omega)$ does not need to be < 0 for all $\omega \in \mathbb{R}$. Rather, the following relation

must be satisfied for successful \mathcal{H}_∞ norm minimization

$$\max_{\omega \in \mathbb{R}} \alpha^{(k)}(\omega) + \bar{\sigma}(\tilde{G}(\tilde{\mathbf{K}}_{init}^{(k)}, j\omega)) < \max_{\omega \in \mathbb{R}} \bar{\sigma}(\tilde{G}(\mathbf{K}_{init}^{(k)}, j\omega)). \quad (8.21)$$

Ideally, $\epsilon_{init}^{(k)}(\omega)$ and $\epsilon_{opt}^{(k)}(\omega)$ would be equal to 0 for all frequencies, i.e. no error is introduced during model reduction and model matching. This reduces (8.14) to (8.21), making optimization of the reduced and detailed models equivalent. However, in general, $\epsilon_{init}^{(k)}(\omega)$ and $\epsilon_{opt}^{(k)}(\omega)$ are non-zero, since model reduction and model matching are not exact. A consequence of (8.14) is that non-zero error terms can even be beneficial for the success of the optimization. If $\epsilon_{opt}^{(k)}(\omega)$ is smaller than zero, and $\epsilon_{init}^{(k)}(\omega)$ is greater than zero, for all $\omega \in \mathbb{R}$, (8.14) becomes less restrictive than (8.21). However, this would mean that the reduced model \tilde{G} needs to overestimate the detailed model G for the initial parameters $\mathbf{K}_{init}^{(k)}$ and $\tilde{\mathbf{K}}_{init}^{(k)}$, and vice-versa for the optimized parameters $\mathbf{K}_{opt}^{(k)}$ and $\tilde{\mathbf{K}}_{opt}^{(k)}$. Finding a model and optimization procedure, which guarantees this property, is in general not possible. Hence, we adopt the strategy to find a model which achieves minimal error terms both before and after the optimization.

8.2.5 Evaluation of the improvement of the system \mathcal{H}_∞ norm

To evaluate (8.14), $\epsilon_{init}^{(k)}(\omega)$ and $\epsilon_{opt}^{(k)}(\omega)$ need to be known. This is, however, challenging, as $G(\mathbf{K}, s)$ is unknown and, thus, (8.15) and (8.16) cannot be directly evaluated. This can be overcome by requiring that each SO sends the discrepancies at sampling frequencies to the SC

$$\Delta_i(\omega)^{(k)} = G_i(\mathbf{K}_{i,opt}^{(k)}, j\omega) - \tilde{G}_i^{(k)}(\tilde{\mathbf{K}}_{i,opt}^{(k)}, j\omega). \quad (8.22)$$

As the SC knows $\tilde{G}_i^{(k)}(\tilde{\mathbf{K}}_{i,opt}^{(k)}, j\omega)$, the values of $G(\mathbf{K}_{i,opt}^{(k)}, j\omega)$ can be calculated combining (8.22) and (8.8) for frequency samples, and consequently $\left\| G(\mathbf{K}_{i,opt}^{(k)}, j\omega) \right\|_\infty$, without knowledge of the detailed structure of each G_i . The Condition (8.14) can be directly used to evaluate whether the optimization was successful.

Remark 4 *The sampled values $\Delta_i(\omega)^{(k)}$ do not explicitly reveal detailed information about the structure and parameters of the subsystems. However, arguably, providing such sampling information decreases the data privacy. By using matrix norm inequalities, it is possible to find sufficient conditions for the norm improvement which require less data to be exchanged between the SOs and SC. One example is $\epsilon_{opt}^{(k)}(\omega)$. However, this introduces conservativeness to the approach, making it less applicable, whereas (8.22) allows us to check the norm-improvement without any conservativeness. Finding less conservative conditions with increased data privacy is a part of future research.*

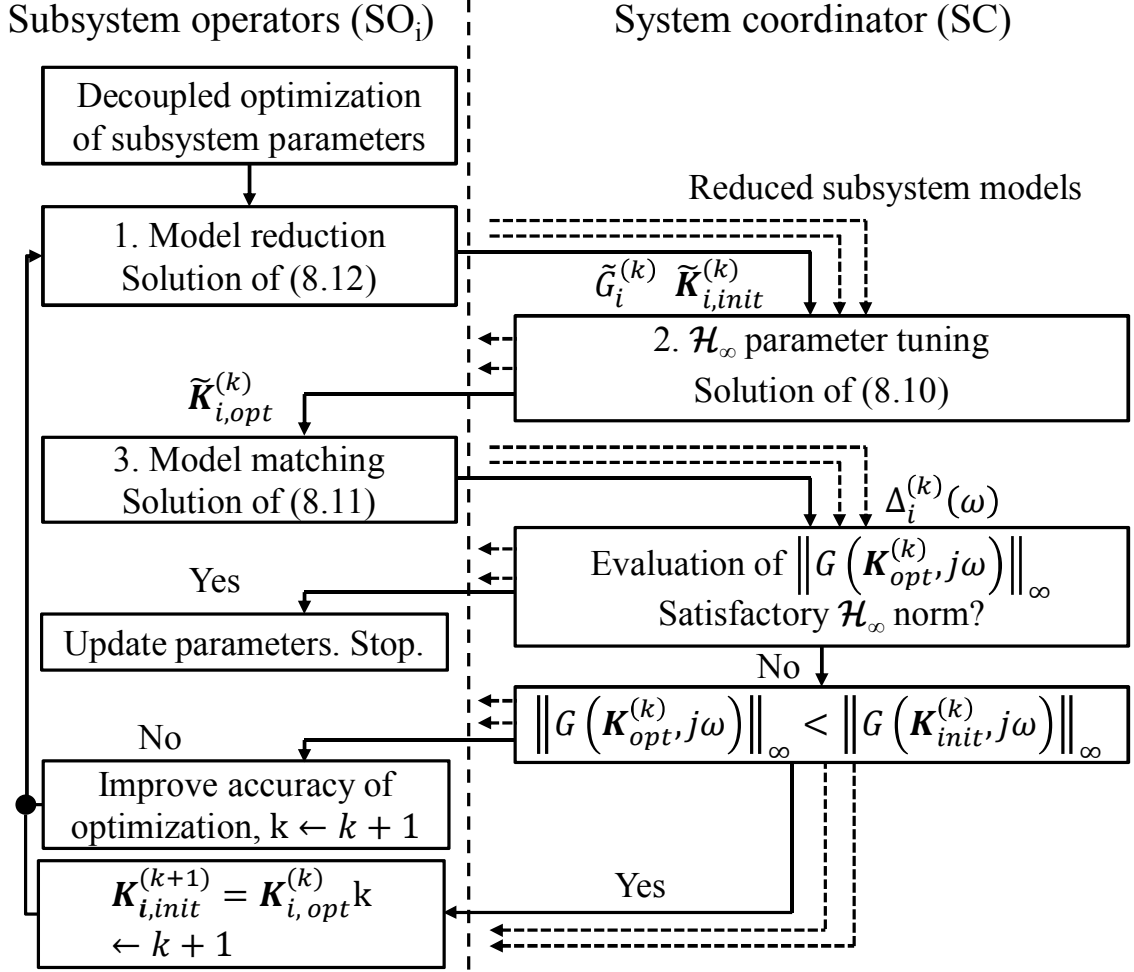


Figure 8.6: Detailed illustration of the proposed optimization approach.

8.2.6 Detailed algorithm for the proposed approach

The overall proposed algorithm is shown in Fig. 8.6. Before the iterations, each SO first tunes its parameters in order to eliminate local oscillations. As described in Section 8.1.3, we use the transfer function $G_i^*(\mathbf{K}_i, s)$, defined with (8.6) for this purpose, where the coupling inputs are used as disturbance inputs for the optimization, in addition to the infeeds of static prosumers. Afterwards, the iterative procedure can start.

In each iteration, the SOs reduce their detailed area model $G_i(\mathbf{K}_i, j\omega)$ by optimizing the parameters of the structured reduced model $\tilde{G}_i'(\mathbf{R}_i, \tilde{\mathbf{K}}_i, j\omega)$ with (8.12). The reduced models, together with the initial reduced parameter vectors $\tilde{\mathbf{K}}_{i,init}^{(k)}$ are then sent to the SC. The SC optimizes the reduced system model with (8.10) and sends the optimized parameter vectors $\tilde{\mathbf{K}}_{i,opt}^{(k)}$ to the SOs. Each SO performs the model matching step by solving (8.11), and sends $\Delta_i^{(k)}(j\omega)$ to the SC.

The SC calculates $\|G(\mathbf{K}_{opt}^{(k)}, j\omega)\|_\infty$ with (8.22) and (8.8). Based on the result, the SC can make the decision to stop the algorithm if the results are satisfactory, to

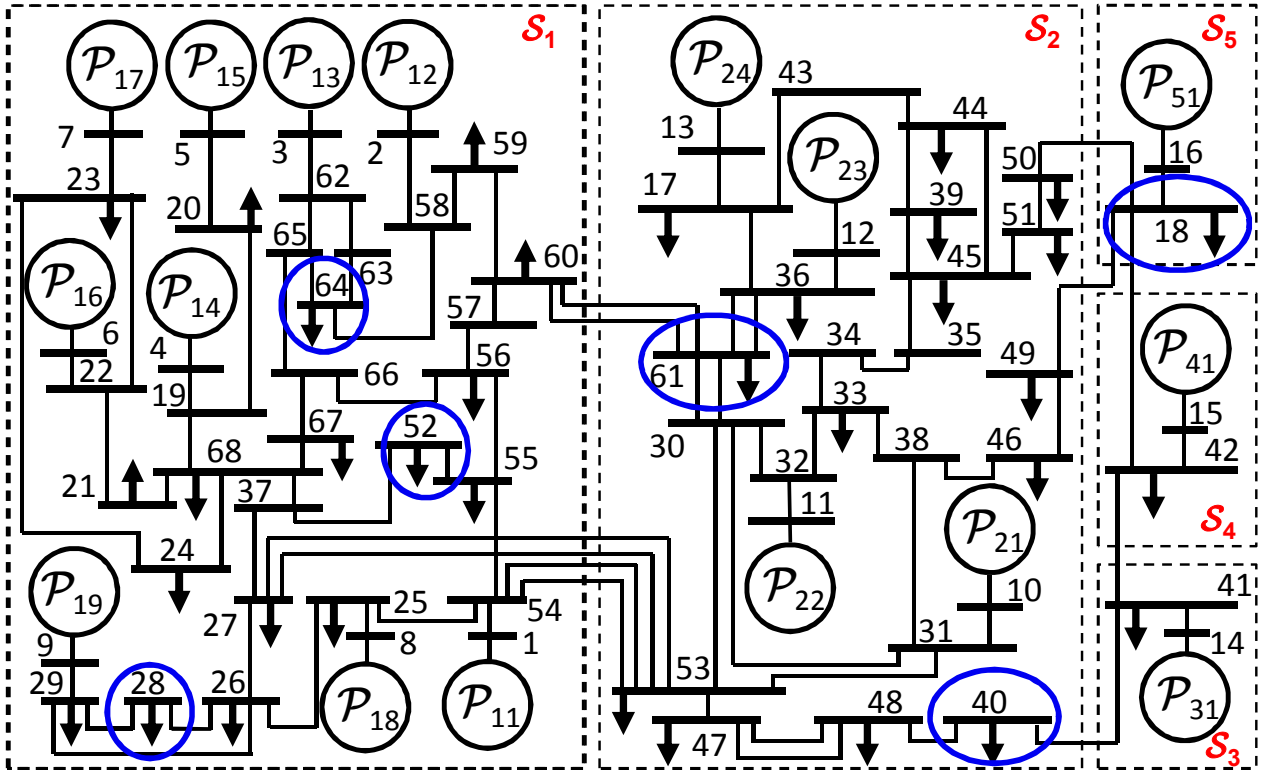


Figure 8.7: IEEE 68 bus model with 16 power plant prosumers, divided into 5 subsystems [105]. The disturbance inputs considered for the \mathcal{H}_∞ parameter tuning are marked in blue.

continue with the next iteration, or to improve the optimization accuracy if the \mathcal{H}_∞ norm of the system increased during optimization. This can be achieved by improving the accuracy of the structured reduced models, e.g. by introducing a more detailed structure of reduced models. Another possibility is to make the box constraints $\tilde{\mathbf{K}}$ and $\bar{\mathbf{K}}$ tighter around $\tilde{\mathbf{K}}_{init}$. With this adaptation, the reduced parameter vector $\tilde{\mathbf{K}}_{opt}^{(k)}$ remains in closer proximity to the initial vector, causing the model reduction error to be smaller after the optimization of the reduced model.

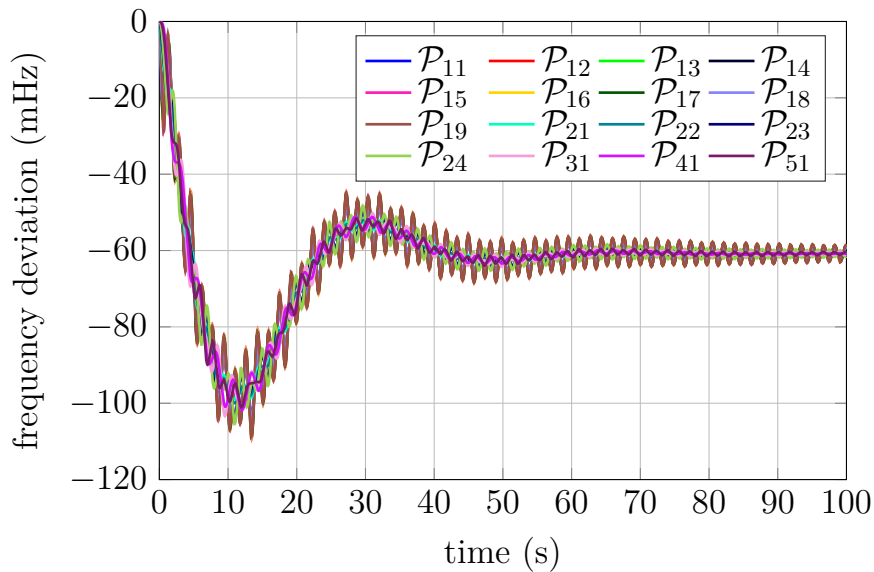
8.3 Application to the IEEE 68 bus example

We consider the IEEE 68 bus power system [105] with 16 dynamic prosumers (power plants), shown in Fig. 8.7. The system consists of five subsystems \mathcal{S}_i , $i = 1 \dots 5$, coupled with power lines, where the subsystems 3-5 are represented by reduced models. The parameters of the power grid and synchronous generators are provided in [105]. All generators are operated with standard IEEE controllers, see Appendix C.4.

In order to justify the motivation of online parameter tuning for power systems with high shares of renewable generation, we first apply the centralized tuning method, which also allows to show the effects of increased renewable penetration in power systems. Subsection 8.3.2, results for the hierarchical algorithm.

Table 8.1: Modes of the IEEE 68 bus system which have damping ratios below 5% for the initial controller parameterization.

mode	frequency (rad/s)	damping ratio (%)
1	3.8	0.5
2	2.5	1.7
3	3.5	2.3
4	6.3	2.9
5	5	4.3
6	7.5	4.4
7	6.3	4.5
8	8.2	4.6

**Figure 8.8:** Frequency response for a 100 MW load step in bus 52. Power plants in subsystems 2 and 3 oscillate against areas 1 and 5.

8.3.1 Centralized tuning and the impact of renewables

In power systems, oscillations with a damping ratio below 5% are considered weakly damped [104]. With the initial parameterization of the controllers, eight oscillatory modes show damping ratios below 5%, see Table. 8.1. The step response of the system to a 100 MW load step in bus 52 is shown in Fig. 8.8. The simulation is performed with a linearized system model, which has shown good accuracy in previous works [71, 72, 74, 75]. The linear system has 280 states and 160 controller parameters with the initial parameter vector \mathbf{K}_{init} .

For the centralized tuning approach, we assume that the transfer function of the entire system is completely known. The solution of the centralized problem will serve as a baseline for the subsequent hierarchical optimization. For the optimization, we use the Matlab toolbox YALMIP [61], together with the solver SeDuMi [109], and the

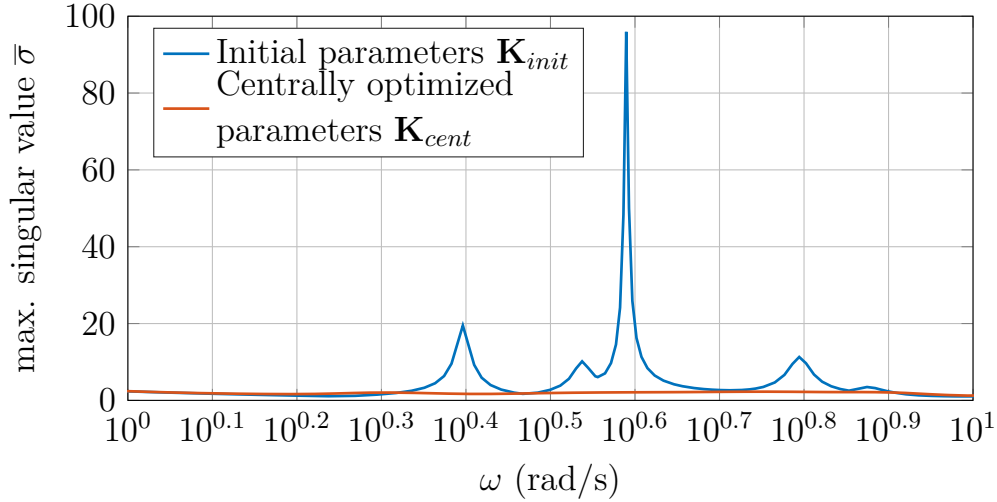


Figure 8.9: Largest singular value of the IEEE 68 bus system as a function of frequency ω . After centralized optimization with (3.19), the resonant peaks in the system are practically eliminated.

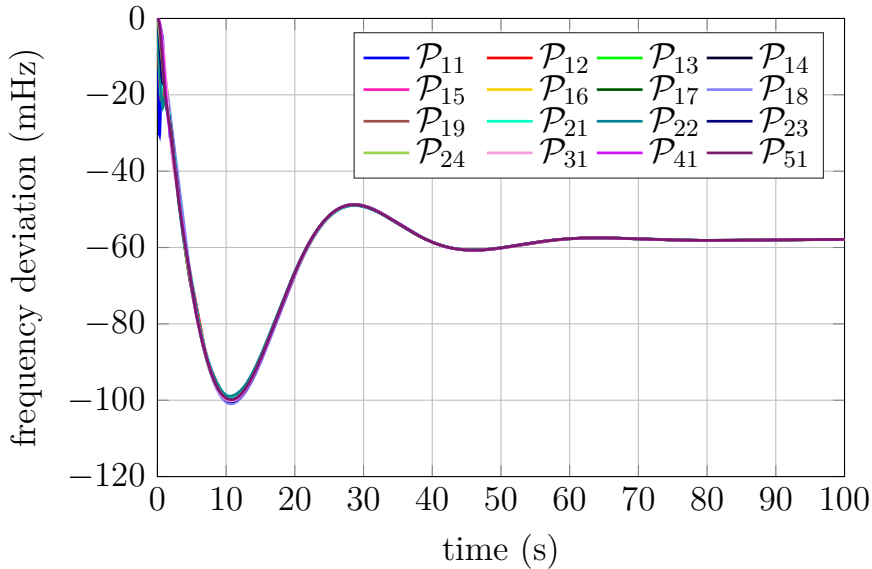


Figure 8.10: Frequency response for a 100 MW load step in bus 52 for the centrally tuned parameters \mathbf{K}_{cent} .

transfer function G^* from (8.6). Disturbance inputs are the active power infeeds of the static prosumers, see Fig. 8.7. After tuning, all oscillatory modes are sufficiently damped with a damping ratio above 7%. We denote the centrally tuned parameter vector of all prosumers with \mathbf{K}_{cent} . The system \mathcal{H}_∞ norm was reduced by 97.5%. Figure 8.9 shows the largest singular values of the system for the initial and optimized parameters. The largest values of the curves in Fig. 8.9 represent the \mathcal{H}_∞ norm with the initial and optimized parameters. The largest peak at approx. 3.8 rad/s corresponds to the oscillatory mode with the poorest damping ratios in Table 8.1. With \mathbf{K}_{cent} , the peak is completely eliminated, which is also visible in Fig. 8.10.

Table 8.2: Frequency and damping of three weakest-dampened modes, which have damping ratios below 5%, for the considered scenarios and controller parameters.

Scenario	\mathbf{K}_{init}	\mathbf{K}_{cent}
Initial	3.9 rad/s, 0.5%	
	2.51 rad/s, 1.7%	
	6.28 rad/s, 2.9%	
\mathcal{P}_{31} scaled	3.83 rad/s, 0.2%	
	2.7 rad/s, 1.4%	4.02 rad/s, 3.6%
	6.28 rad/s, 2.9%	
\mathcal{P}_{22} scaled	3.9 rad/s, 0.4%	2.51 rad/s, 3%
	2.45 rad/s, 1.7%	3.46 rad/s, 3%
	6.28 rad/s, 2.9%	4.9 rad/s, 3.7%

When the amount of renewable generation in the system increases, conventional prosumers, such as power plants, will be disconnected from the grid to prevent overproduction. In the considered power system, power plants already represent aggregated models of multiple smaller power plants, thus, the disconnection of smaller power plants is modeled by reducing the nominal power of the power plants \mathcal{P}_{ij} . The power infeed of the power plant is also reduced and shifted to static prosumers in the same bus, i.e., we model renewable generation in this system as static prosumers [83, 87].

To simulate the effects of large scale renewable generation, we consider two scenarios. The first scenario considers increased renewable integration in \mathcal{S}_3 . For this purpose, we reduce the power of \mathcal{P}_{31} to 15% of its original value and assume that power plants with PSSs are disconnected. In the second scenario, we consider increased renewable generation in \mathcal{P}_{22} . We rescale the power of \mathcal{P}_{22} to 50% of its original value and deactivate PSS₂₂. Details of the scenarios are presented in Table 8.2. In both scenarios, the damping becomes worse for the initial parameters \mathbf{K}_{init} . Even though \mathbf{K}_{cent} eliminates weakly dampened eigenmodes for the initial, nominal, scenario, weakly dampened oscillations still emerge in the other two scenarios. New parameter sets are needed to improve the oscillation damping for these scenarios, demonstrating the necessity for online adaptation of parameters to counteract the change.

It is possible to consider all three scenarios during the parameter tuning procedure by forming a parallel connection of the systems corresponding to the scenarios and solving (3.19), similarly as in [71]. However, as the share of renewable generation in the power system increases, the number of possible scenarios rises exponentially. On one hand, this means that it becomes increasingly difficult to solve (3.19) for all scenarios, and on the other, the parameters which we find for all scenarios can become increasingly suboptimal when one concrete scenario is realized. Consequently, online adaptation of controller parameters will lead to a more resilient system with a better

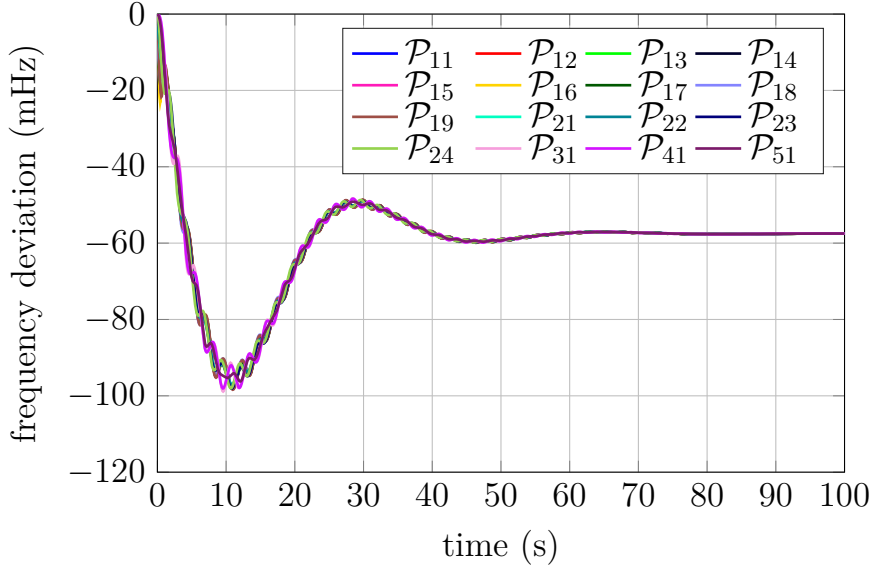


Figure 8.11: Frequency response of the detailed model to a 100 MW load step in bus 52 for completely decentrally optimized parameters \mathbf{K}_{dcp} .

performance, because the controller parameters are optimized for only the realized scenario.

8.3.2 Hierarchical data privacy conserving \mathcal{H}_∞ parameter tuning

We now apply the proposed hierarchical data privacy preserving tuning method on the IEEE 68 bus power system. Note that as subsystems $\mathcal{S}_3 - \mathcal{S}_5$ are already replaced with reduced models, the reduction and matching step is not necessary for these systems.

As shown in Fig. 8.6, each SO first tunes the parameters of its controllers without regarding other systems by using $G_i^*(\mathbf{K}_i, s)$. We consider thereby the coupling inputs as disturbances. Figure 8.11 shows the step response of the detailed coupled system after this step. We denote this (decoupled) parameterization of each subsystem with $\mathbf{K}_{dcp} = \text{vec}_i(\mathbf{K}_{dcp,i})$. As can be seen, the step response was significantly improved compared to the response with initial parameters in Fig. 8.8. However, it is still worse than the centrally tuned parameterization \mathbf{K}_{cent} in Fig. 8.10, and three weakly damped modes still remain, as summarized in Table 8.3. Thus, even though each SO eliminated the oscillations within the subsystem, oscillations between the subsystems could not be eliminated without consideration of the coupling between the subsystems.

In order to improve the step response, we apply the described optimization steps in the next sections.

8.3.3 Structured model reduction

Structured model reduction has been applied for decades in power systems for reducing the number of power plants. However, this is most often done in order to decrease

Table 8.3: Frequency and damping ratios of weakly-dampened modes in the coupled system when each SO optimizes its parameters separately, i.e. with \mathbf{K}_{dcp} .

Mode	frequency (rad/s)	damping ratio (%)
1	2.51	2.6
2	3.52	3.8
3	4.9	4.4

the computational burden for simulation, and not for controller synthesis. Most works in the literature perform model reduction based on the so-called coherency, i.e. the generators are grouped according to the oscillatory mode to which they belong, c.f. [19, 33, 53]. On the other hand, approaches which perform model reduction based on geographical location, require parameters from the whole system for the reduction procedure [55], and/or generate reduced models which do not have a pre-specified structure [95, 108]. An overview of different power system reduction techniques is presented in [57].

Current state of the art approaches for structured model reduction are not suitable for our approach. First, the approaches require the exchange of detailed parameters/data of the subsystems, which violates our goal of data privacy. Second, unstructured models are often generated, which do not allow to retain insight into what parameters can be tuned to minimize the \mathcal{H}_∞ error between the reduced and detailed model.

For this reason, we introduce a hybrid approach for distributed model reduction for power systems. It consists of two steps. In the first step, we create an equivalent model of a synchronous generator (SG) from a group of SGs in \mathcal{S}_i . As equivalent models of SGs are well studied in the literature, we use the analytical procedure from [19] for this step.

In the second step, we parameterize of equivalent controllers for the SG. This challenge, however, was not intensively studied. Thus, to parameterize the controllers of the equivalent SG, i.e. TGOV_{ij}, AVR_{ij}, and PSS_{ij}, we use (8.12). We first choose models for the controllers occurring in the system with the highest frequency. In case of the IEEE 68 bus system, those are the controllers in Figs. C.9, C.1 and C.2 in Appendix C.4. The tunable controller parameters, which are part of the vector $\widetilde{\mathbf{K}}_i$, are marked red in the figures, whereas all other parameters are a part of the vector \mathbf{R}_i .

In case of the IEEE 68 bus system, subsystems \mathcal{S}_1 and \mathcal{S}_2 are each replaced by one equivalent power plant, which has shown to be sufficient. Figures 8.12 and 8.13 show the largest singular values of the reduced and detailed model of \mathcal{S}_1 and \mathcal{S}_2 , respectively, before and after the parameterization procedure. They show a very good match between the detailed models and the reduced models after the parameterization.

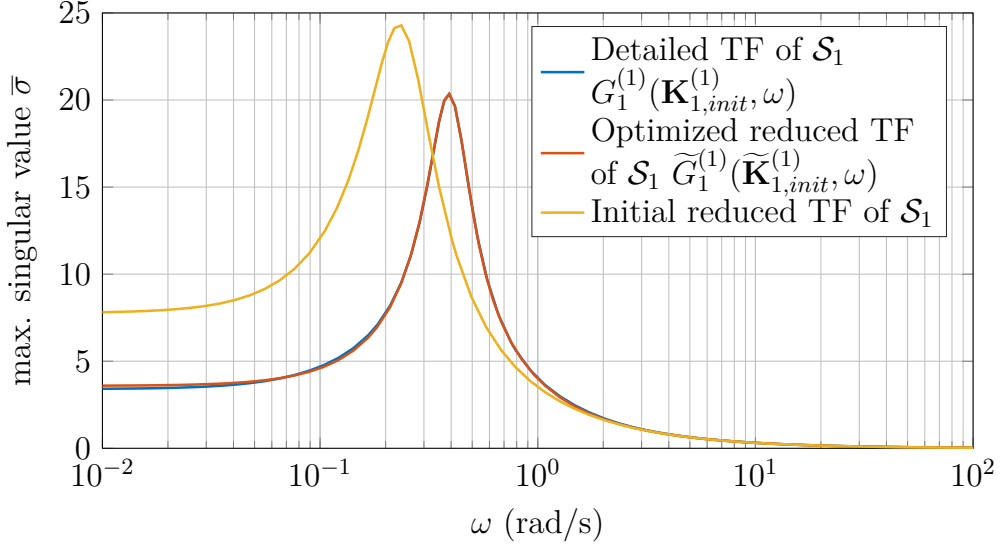


Figure 8.12: Largest singular values of the detailed and reduced model of \mathcal{S}_1 . Note that the blue curve is mostly covered by the red curve.

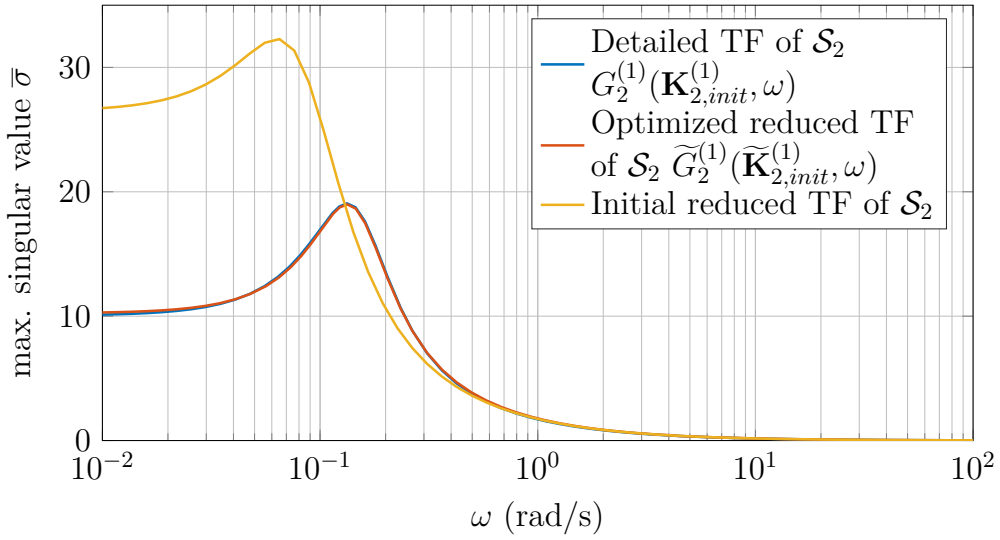


Figure 8.13: Largest singular values of the detailed and reduced model of \mathcal{S}_2 , showing a good match. Note that the blue curve is mostly covered by the red curve.

8.3.4 Structured \mathcal{H}_∞ optimization for the overall reduced system

The SC lumps the reduced subsystem models into $\tilde{G}(\tilde{\mathbf{K}}, s)$. The reduced system for the IEEE 68 bus model is depicted in Fig 8.14. The static infeeds, marked blue, are used as disturbance inputs, and are elements of the reduced vector of disturbances $\tilde{\mathbf{w}}_S$. A system with 89 states and 50 optimization parameters is obtained, whereas the detailed model has 280 states and 160 controller parameters. We denote the initial parameter vector of the detailed and the reduced model by $\mathbf{K}_{init}^{(1)}$ and $\tilde{\mathbf{K}}_{init}^{(1)}$, respectively. The step response of the reduced system to a 100 MW load step in bus 2 is shown in Fig. 8.15. The oscillations in the coupled system are less dampened than with $\mathbf{K}_{init}^{(1)}$

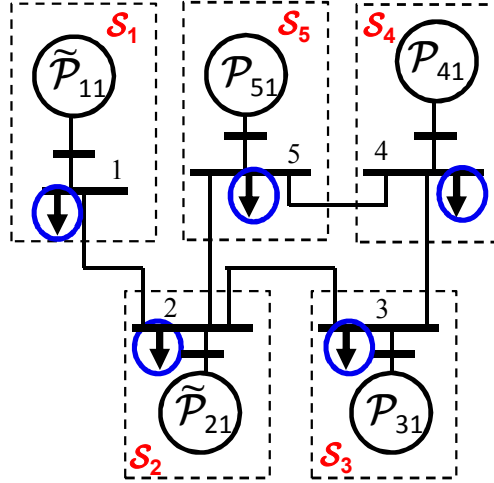


Figure 8.14: Reduced model of the IEEE 68 bus power system. Disturbance inputs for the optimization are marked blue.

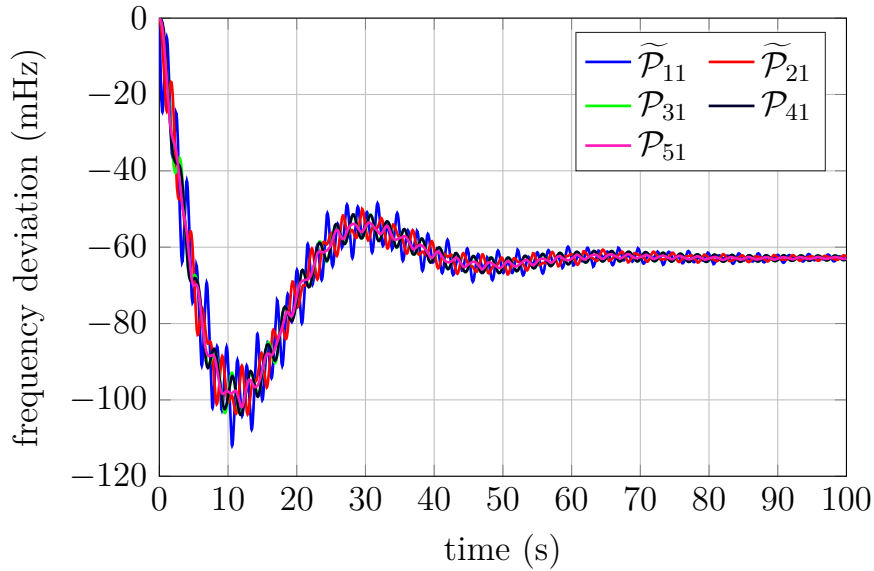


Figure 8.15: Step response of the reduced model in Fig. 8.14 in the first iteration $\tilde{G}^{(1)}(\tilde{\mathbf{K}}_{init}^{(1)}, \omega)$ to a 100 MW load step in bus 2 with $\tilde{\mathbf{K}}_{init}^{(1)}$.

in the detailed model, c.f. Fig. 8.11. However, a 100% accuracy of the reduced model is not required for the approach to be successful, as described in Section 8.2.4.

The SC optimizes the reduced model using (8.10), and obtains the optimized parameter vector $\tilde{\mathbf{K}}_{opt}^{(1)}$.

8.3.5 Model matching

In the last step, the SOs optimize with (8.11) the parameters of the detailed subsystem models to match the reduced model. Figures 8.16 and 8.17 show the results of the model matching step for \mathcal{S}_1 and \mathcal{S}_2 . For \mathcal{S}_2 , model matching could not decrease the

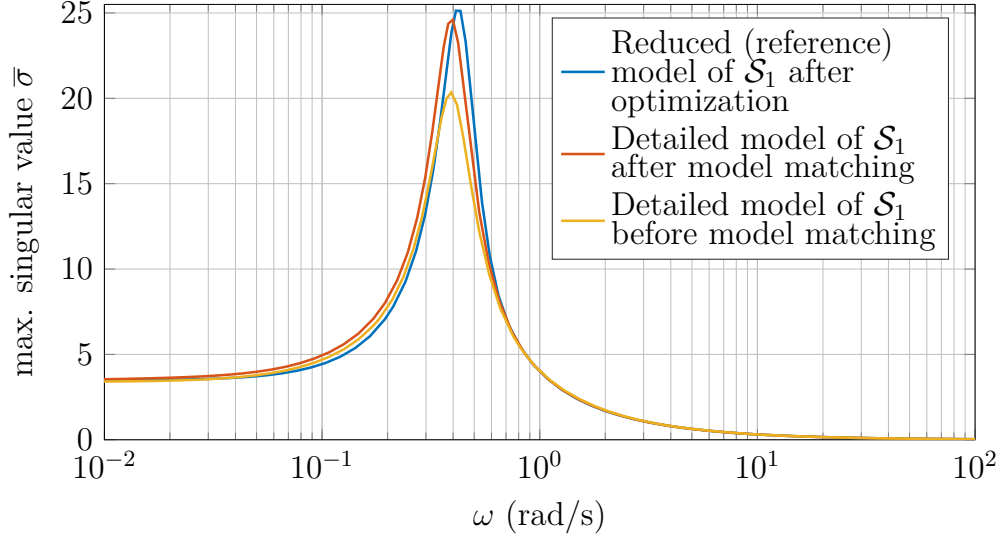


Figure 8.16: Largest singular values of the detailed and reduced system for \mathcal{S}_1 before and after the model matching step.

difference between the detailed and reduced model. However, the error can be reduced by relaxing the box constraints of controller parameters in \mathcal{S}_2 or by making the box constraints for $\tilde{\mathbf{K}}_2$ in the reduced model tighter, which was not necessary, as the obtained coupled system norm is sufficiently good even after one iteration.

Counter-intuitively, the reduced reference models for \mathcal{S}_1 and \mathcal{S}_2 have larger \mathcal{H}_∞ norms than the initial models. This underpins that \mathcal{H}_∞ optimization of the decoupled subsystems does not necessarily minimize the \mathcal{H}_∞ norm of the coupled system. This is also evident from the optimization results shown subsequently in Fig. 8.19, in which the optimized coupled (detailed and reduced) systems have a lower \mathcal{H}_∞ norm than the initial respective systems, even though the \mathcal{H}_∞ norm of the decoupled subsystems increased.

8.3.6 Results of hierarchical \mathcal{H}_∞ controller tuning

After the model matching step, the parameter vectors $\mathbf{K}_{i,opt}^{(1)}$ are obtained for each subsystem \mathcal{S}_i . The time response of the detailed system, with the parameterization $\mathbf{K}_{opt}^{(1)} = \text{vec}_i(\mathbf{K}_{i,opt}^{(1)})$, to a 100 MW load step in bus 52 is shown in Fig. 8.18 with solid lines. The same figure also shows the optimized step response of the reduced model with $\tilde{\mathbf{K}}_{opt}^{(1)}$ in dashed lines, showing a very good correspondence of the two models. Furthermore, the response looks almost identical as the results with centralized tuning in Fig. 8.10. With $\mathbf{K}_{opt}^{(1)}$, all weakly-damped modes are eliminated from the system as well. The system \mathcal{H}_∞ norm was reduced by 97.5%, which was also the case with \mathbf{K}_{cent} . This could not be achieved with \mathbf{K}_{dcp} , when all SOs tuned their parameters separately.

Figure 8.19 shows the largest singular values of the detailed and reduced system in

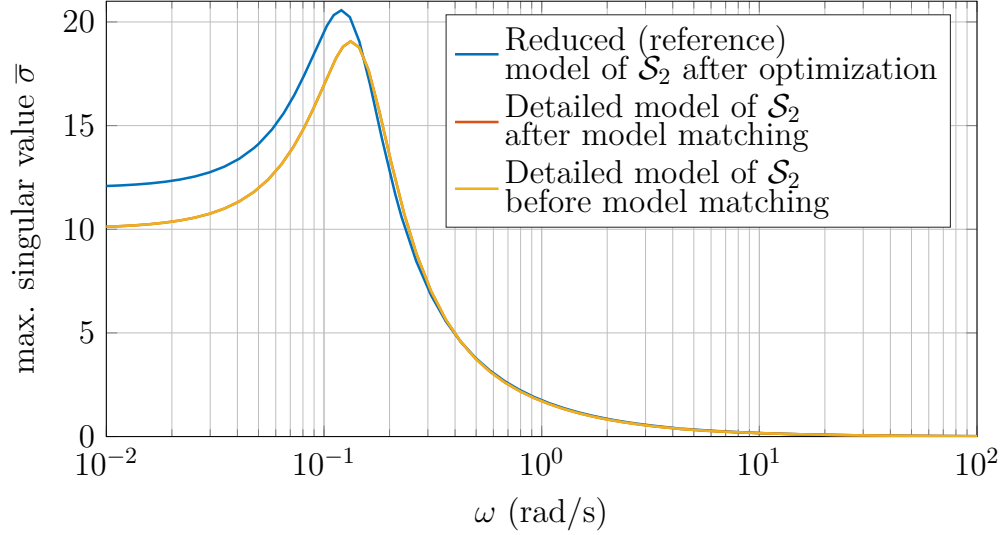


Figure 8.17: Largest singular values of the detailed and reduced system for \mathcal{S}_2 before and after the model matching step. Note that the red curve is under the yellow curve.

the relevant frequency range for the various parameterizations. With the decoupled parameterization \mathbf{K}_{dcp} , a large peak is still present in the system at approx 2.5 [rad/s]. The reduced model with $\widetilde{\mathbf{K}}_{init}^{(1)}$ is able to recreate this peak, and introduces an additional peak at approx. 4 Hz. However, 100% accuracy of the reduced model is not necessary for the approach to be successful. Both peaks in the reduced model are eliminated with $\widetilde{\mathbf{K}}_{opt}^{(1)}$. The resulting parameterization of the detailed model $\mathbf{K}_{opt}^{(1)}$ with the decentralized approach achieves approximately the same results as \mathbf{K}_{cent} .

8.4 Tuning for an artificial large scale power system

To show the applicability of the proposed approach on a large and complex power system, we couple nine IEEE 68 bus power systems, as shown in Fig. 8.20. The northern connection in each subsystem is made with bus 43, the southern connection with bus 48, the eastern with 42, and western with 21. This system is strongly meshed, and has 2520 states and 1440 controller parameters, making centralized optimization impossible.

For the hierarchical tuning, we replace each subsystem \mathcal{S}_i with a single-generator equivalent model in the model reduction step, analogously as in the previous example. Thus, in the optimization step, a system with 171 states and 90 controller parameters is optimized, instead of the original 2520 states and 1440 parameters, which is impossible to handle.

Figure 8.21 shows the singular value plot of the system with the initial parameterization and subsequent results. The largest peak, corresponding to the value 360 at approximately 1 rad/s, is cut-off to improve visibility of other plots. With the pro-

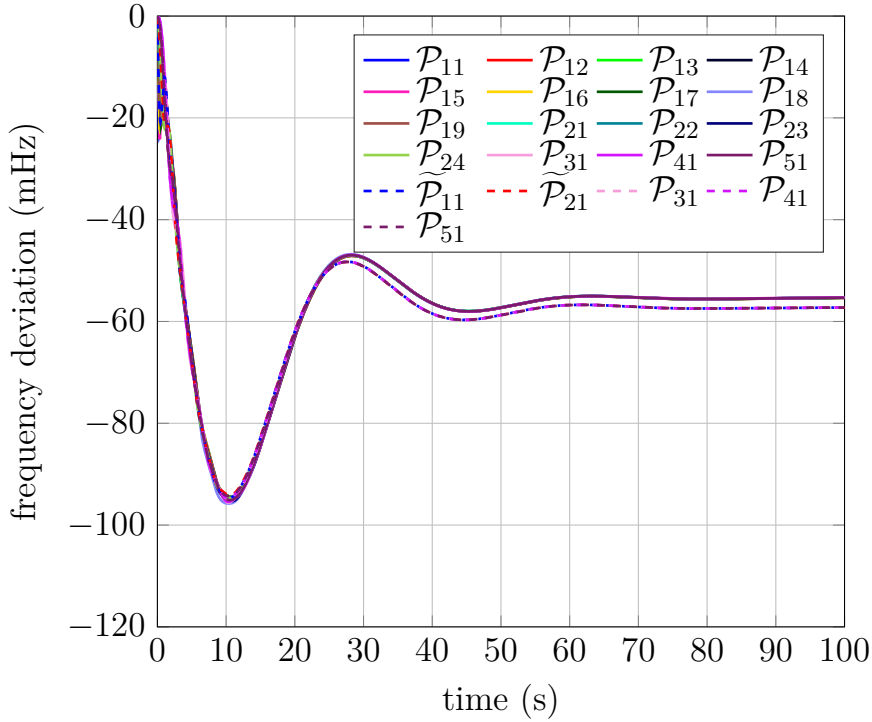


Figure 8.18: Step response of the optimized detailed and reduced IEEE 68 bus model to a 100 MW load step. Solid lines represent simulation of a 100 MW load step in bus 52 with the detailed model and $\mathbf{K}_{opt}^{(1)} = \text{vec}_i(\mathbf{K}_i^{(1)})$, whereas dashed lines represent simulation of a 100 MW load step in bus 2 with the reduced model and $\tilde{\mathbf{K}}_{opt}^{(1)}$.

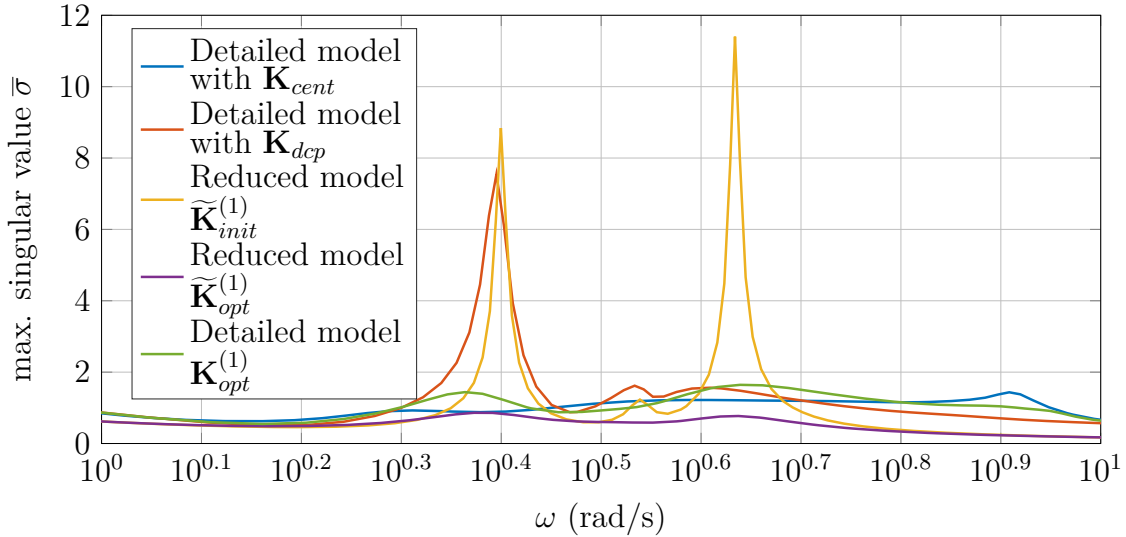


Figure 8.19: Largest singular values of the reduced and detailed models of the IEEE 68 bus system achieved with the various parameterizations.

posed approach, the \mathcal{H}_∞ norm of the system was reduced by 95% in four iterations. Thereby, the resonant peaks are almost eliminated. The decoupled parameterization,

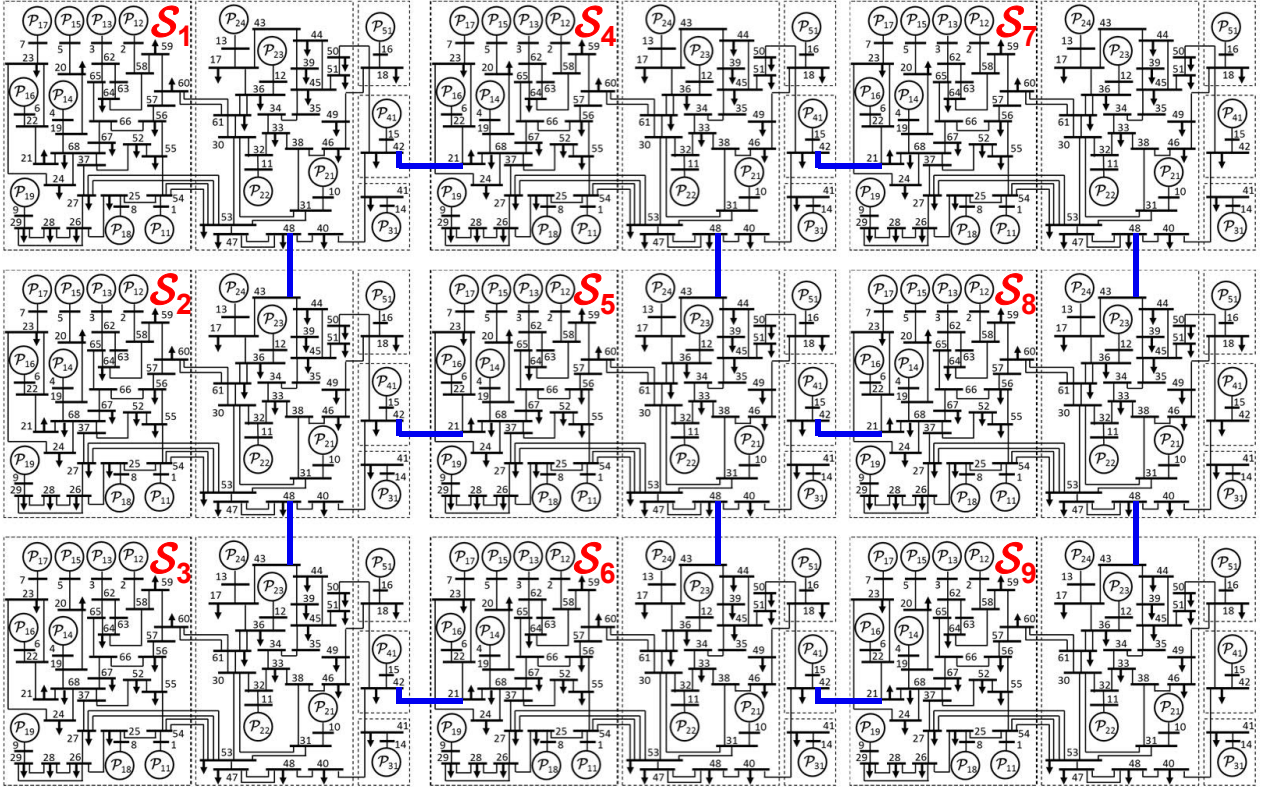


Figure 8.20: Large synthetic power system obtained by coupling nine IEEE 68 bus systems. The system consists of 144 power plants, 2520 dynamic states and 1440 controller parameters.

i.e. when each SO tunes its respective controller parameters separately, is also shown Fig. 8.21. Even though the \mathcal{H}_∞ norm of the system is significantly improved compared to the initial parameterization, a large peak still remains.

The time-domain response of the system to simultaneous load steps in 10 buses with the initial, decoupled, and optimized parameterization after four iterations, is shown in Fig. 8.22. With the decoupled parameterization, large oscillations still prevail at the end of the time horizon. On the other hand, the oscillations are significantly better damped with the proposed approach. This shows that the presented approach is capable of optimizing such large and complex systems and can lead to very good results.

This results were achieved using a Windows computer with an Intel[®] i7-4810MQ CPU running at 2.8 GHz. The model reduction step requires approx 30s on average for one subsystem. The optimization of the reduced system requires approx. 1 minute, whereas the model matching step requires less than 5 minutes for each subsystem due to the larger number of optimization parameters. Consequently, assuming that the model reduction and model matching steps for each subsystem are executed in parallel, approx. 7 minutes are needed for one iteration of the algorithm. Thus, even such large systems can be optimized in less than 30 minutes, depending on the number

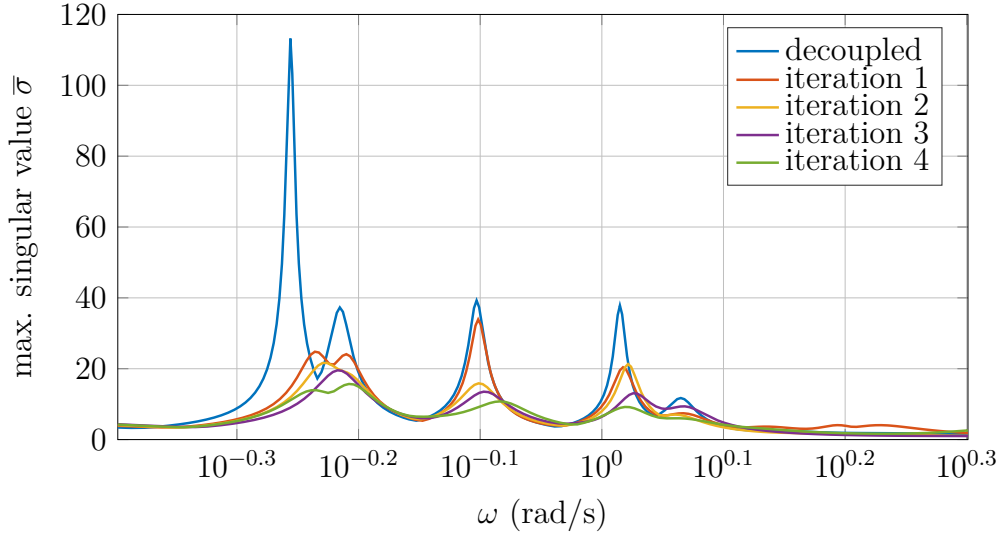


Figure 8.21: Largest singular values of the large system in Fig. 8.20 with the initial parameterization, decoupled parameterization, when each SO optimizes its parameters separately, and after the model matching step in each iteration of the optimization. The highest peak of the plot with initial parameterization, corresponding to the value 360 at approximately 1 rad/s, is cut-off to improve visibility of other plots.

of iterations until a satisfactory system norm is achieved. Note that further subsystems can be coupled without increasing the computation time significantly, as the model reduction and model matching step are done in parallel.

8.5 Summary

Tuning of controller parameters in power systems increases system resiliency when power system dynamics are constantly changing, e.g. due to an increasing share of renewable generation. This is particularly challenging for two reasons: (a) the power systems can have a very large size, and (b) large power systems often belong to a multitude of subsystem operators which are not willing to exchange detailed information about their subsystems. We proposed an algorithm for hierarchical structured \mathcal{H}_∞ controller synthesis in power systems which addresses both of these challenges and demonstrated its effectiveness on two simulation examples. Thereby, we derived conditions when the hierarchical approach will lead to an improved parametrization of the coupled system and introduced an algorithm which ensures that the \mathcal{H}_∞ norm of the coupled system is improved. In the first simulation example, we demonstrated how increased percentage of renewable generation leads to changing dynamics in the system, showing the need for online reparameterization of controllers. Additionally, we showed in the example that weakly-dampened oscillatory modes in the overall system cannot be eliminated if all subsystems optimize their parameters separately. The

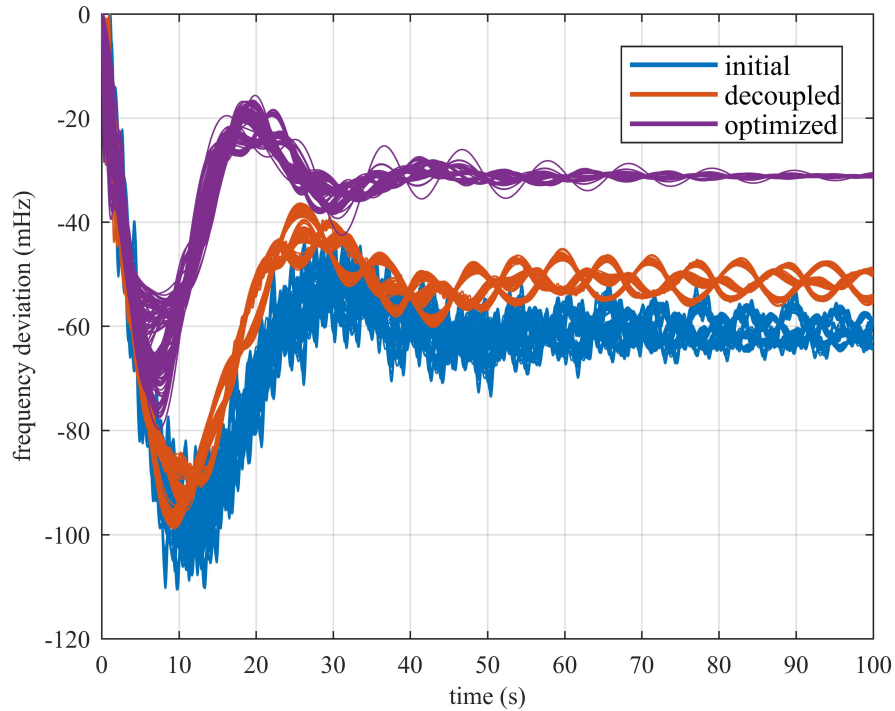


Figure 8.22: Frequency response of the synthetic power system to 100 MW load steps in 10 buses with the initial, decoupled, and optimized parameterization. Due to the large amount of dynamic prosumers, each parameterization is represented with one color.

proposed hierarchical approach eliminates the weakly damped modes in the first numerical example, and it achieves approximately the same results as with centralized tuning. In the second example, we showed the scalability and efficacy of the approach on an even larger power system, where centralized tuning cannot be applied, thereby practically eliminating oscillations from the system.

9 Conclusions and outlook

Increasing the share of renewable generation in power systems leads to increased volatility and uncertainty in their operation. Depending on weather conditions, the power generation of renewables will vary temporally, as well as geographically in the power grid. Furthermore, if the weather conditions are not suitable, conventional generation, such as thermal power plants, will need to be used. This leads to changing dynamics in power systems, i.e. time-varying oscillatory modes appear and they need to be damped. However, existing automation systems for power systems are designed for fixed, known, dynamics. Control systems of components are typically parameterized only once during installation, which is a time-consuming task. When time-varying dynamics are constantly present in the system, the risk of a blackout increases. Changing the existing control system entirely to increase stability is often not possible, as it has gained the trust of operators during decades of practical operation, and due to the high costs for the replacement.

In this thesis, we propose to solve this challenge by adapting the parameters of the existing control system to the changing conditions. For this purpose, two base methods are introduced which minimize the \mathcal{H}_∞ norm of the system by tuning controller parameters. The first method is based on the Bounded-Real Lemma, whereas the second method uses frequency sampling. Both methods provide stability certificates and are applicable to arbitrary power systems and on brown-field applications. The system \mathcal{H}_∞ norm is chosen as the tuning goal as it improves robustness of the system against uncertainties, in addition to improving oscillation damping.

The proposed methods are verified in multiple numerical examples. In each example, the \mathcal{H}_∞ norm of the system was significantly reduced, thereby also improving the time-domain step response. Furthermore, the approach was experimentally validated on a testbed microgrid in Wildpoldsried, Germany. The testbed system consists of six inverters connected to a load bank. Due to asymmetries in the power grid, oscillations were present in the system. With the proposed approach, they were successfully eliminated, showing the applicability of the approach on existing systems and control structures.

A comparison of the proposed approaches with existing approaches with respect to performance and to the computational complexity was outlined. Thereby, the proposed approach showed better results in the time-domain in the considered numerical example, compared to methods which introduce an additional wide-area control layer in the system. Furthermore, the proposed frequency-sampling based method, achieved significantly reduced computation times and better scalability, compared to existing

approaches and commercial software.

Furthermore, a hierarchical approach for the controller tuning was introduced, which allows for data privacy and safety. It considers practical constraints arising from the operation of large power systems, in which there is no entity which has access to all parameters of the power system. Moreover, such power systems usually have thousands of states, making centralized optimization numerically intractable. The proposed approach successfully solves these issues by modularization, introducing model reduction, which hides parameters of the detailed system inside the reduced model. Conditions are derived for the success of the approach and an algorithm for the tuning process is developed. Finally, the approach is validated on two large numerical examples.

Overall, the results in this thesis provide the basis for the adaptation of controller parameters in power systems, showing approaches which give good results and are scalable to large systems. They lay the basis for a series of future developments.

9.1 Outlook

These results addressed in this thesis offer the opportunity for further research. We first describe logical extensions of the presented results before indicating more distant research directions.

The considered modeling approach does not include dynamics of the power grid, i.e. of the power lines, transformers etc. While this is a commonly used approximation, recent results indicate that these dynamics can potentially impact the system stability if no conventional generation is present in the system. The proposed approach can be extended to include the grid dynamics. However, an approach is needed such that the system can still be appropriately linearized. For this purpose, the so-called dynamic phasors approach offers a possible research direction.

This thesis did not consider in depth a robust procedure of switching the controller parameters. This procedure should consider constraints such as communication outages and inexact time synchronization between the consumers. From this procedure, new requirements for the parameter tuning algorithm could emerge.

To guarantee a stable operation even in extreme conditions, such as islanding or cascading outages, more constraints can be included into the optimization problem. This can be done by including additional constraints for stability of the decoupled systems. However, it leads to a potentially large number of constraints, making the optimization problem challenging to solve in a small time frame. The same problem is encountered in the multi-scenario approach. Future research could focus on efficiently solving the tuning problem for many scenarios. A possible way to do it is to optimize a subset of “worst-case” scenarios, such that if these scenarios are optimized to have satisfying performance, other scenarios have it as well.

An interesting further research direction considers the stability-certificate of the fre-

quency sampling method for \mathcal{H}_∞ optimization, i.e. Theorem 3. If the \mathcal{H}_∞ constraint can guarantee that a system will remain stable, given an initial stabilizing parameterization, the question arises if the same constraint can be used for system stabilization. This could be done by virtually shifting the imaginary axis into the unstable region of the complex plane, such that all system poles lie on the left side of the virtual imaginary axis. Then, the axis can be shifted to the left during optimization. In this way, a fast method for the stabilization of linear systems could be developed.

Further research should be made to find a stability guarantee for the hierarchical tuning approach. In the current algorithms, instability can be detected after the model matching step and appropriate adjustments can be made to avoid instability. However, a direct constraint for stability, which guarantees that the solution of model matching will result in a stable coupled system, would significantly speed up the acceptance of the approach. However, the constraint would need to have a distributed formulation. For this purpose, the input-to-state-stability seems to offer a promising lead.

A Oscillation damping in linear systems

In this thesis, we use \mathcal{H}_∞ optimization to improve the system robustness, as well as improve the oscillation damping in power systems. However, these two terms are, at a first glance, not directly correlated. For this purpose, we briefly summarize in this appendix modal analysis of linear systems and show the connection between the \mathcal{H}_∞ norm and oscillation damping in linear systems.

A.1 Modal analysis of linear systems

We consider the linear system

$$\dot{\mathbf{x}} = A\mathbf{x}, \quad (\text{A.1})$$

where $A \in \mathbb{R}^{n \times n}$. The goal is to find an analytic expressions for oscillations in (A.1), called natural oscillations. To this end, we perform an eigenvalue decomposition of A

$$A = \Phi\Lambda\Phi^{-1}, \quad (\text{A.2})$$

where Φ is the complex-valued matrix of right eigenvectors of A , and Λ is the complex-valued diagonal matrix of its eigenvalues $\lambda_1, \dots, \lambda_n$. Note that λ_i may be complex, in which case there exists λ_j equal to the complex-conjugate value of λ_i . By inserting the previous equation into (A.1), and by introducing the new state vector $\mathbf{z} = \Phi^{-1}\mathbf{x}$, we obtain

$$\dot{\mathbf{z}} = \Lambda\mathbf{z}. \quad (\text{A.3})$$

Since Λ is a diagonal matrix, we obtained a system of uncoupled equations

$$\dot{z}_i = \lambda_i z_i, \quad i = 1 \dots n, \quad (\text{A.4})$$

which can be directly solved

$$z_i(t) = z_i(0)e^{\lambda_i t}. \quad (\text{A.5})$$

Remarkably, from the coupled system (A.1), we obtained a completely decoupled system in terms of the so-called system eigenmodes \mathbf{z} . It follows that the time response

of \mathbf{x} is given with

$$\mathbf{x} = \Phi \mathbf{z} = \sum_{i=1}^n \Phi_i \mathbf{z}_i(0) e^{\lambda_i t}, \quad (\text{A.6})$$

where Φ_i is the i -th right eigenvector of A , corresponding to λ_i . Since $\mathbf{z} = \Phi^{-1} \mathbf{x} = \Psi \mathbf{x}$, where Ψ is the matrix of left eigenvectors of A , we can now write

$$\mathbf{x} = \sum_{i=1}^n \Phi_i \Psi_i \mathbf{x}(0) e^{\lambda_i t}, \quad (\text{A.7})$$

where Ψ_i is the i -th row of Ψ . Thus the initial condition response of the system is given by the linear combination of n system eigenmodes, corresponding to the n eigenvalues of the state matrix. Thereby, real eigenvalues correspond to non-oscillatory modes, whereas complex eigenvalues correspond to oscillatory modes of the system. It is possible to reformulate terms with complex-conjugate eigenvalue pairs $\sigma \pm j\omega$ to obtain the form $e^{\sigma t} \sin(\omega t + \theta)$. It represents a dampened sinusoid with the damping factor σ . The frequency of the oscillation is ω , and the damping ratio for the eigenmode is defined as

$$\xi = \frac{-\sigma}{\sqrt{\sigma^2 + \omega^2}} \cdot 100\%. \quad (\text{A.8})$$

With this definition, the amplitude of the oscillation decreases to $1/e$ of the initial value in $1/(2\pi\xi)$ oscillations.

Each system eigenmode, corresponding to an eigenvalue, has an associated damping ratio which depends on the real and imaginary part of the eigenvalue. In power system analysis, the damping ratio is most often used as a metric for oscillation damping. For example, a 5% damping ratio is often used as the recommended minimal damping factor of oscillations in power systems [104]. This means that all system eigenvalues must lie inside a cone on the left-hand side of the complex plane, illustrated in Fig. A.1.

In summary, the damping of oscillations in linear systems only depends on the location of system poles. If a minimal damping ratio ξ is desired in the system, then all system poles need to lie in the region shown in Fig. A.1.

A.2 Relation between the \mathcal{H}_∞ norm and oscillation damping

The \mathcal{H}_∞ norm of the linear system $G(s) = C(sI - A)^{-1}B + D$, denoted with $\|G(s)\|_\infty$, is defined as the maximal \mathcal{L}_2 amplification of an input \mathbf{w} in any output direction \mathbf{y} , i.e.

$$\|G(s)\|_\infty = \max_{0 < \|\mathbf{w}\|_2 < \infty} \frac{\|\mathbf{y}\|_2}{\|\mathbf{w}\|_2}. \quad (\text{A.9})$$

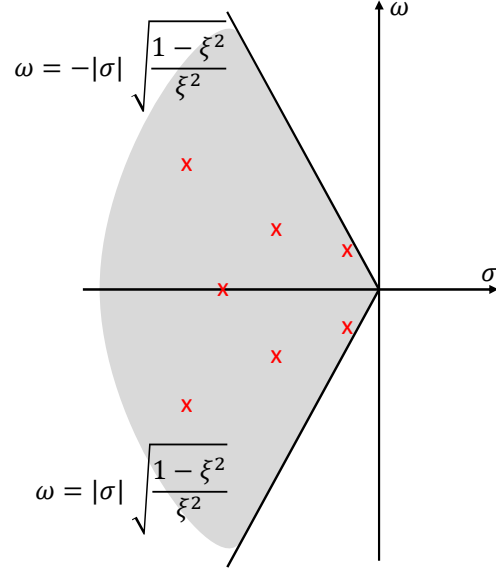


Figure A.1: Illustration of the region in the complex plane where all system poles, marked with a red “x”, have a minimal damping-ratio ξ .

In the frequency domain, the \mathcal{H}_∞ norm is calculated as

$$\|G(s)\|_\infty := \max_{s \in \mathbb{C}_{>0}} \bar{\sigma}(G(s)), \quad (\text{A.10})$$

where $\bar{\sigma}(G(s))$ denotes the maximal singular value of $G(s)$. As the \mathcal{L}_2 norm of a signal is proportional to its energy, the minimization of $\|G(s)\|_\infty$ decreases the energy-amplification of disturbances in the system at the observed outputs. Additionally, it improves the stability margin of the system [119], meaning that the system can tolerate larger disturbances while still remaining stable (commonly known as the small gain theorem).

The relation between oscillation damping and the system \mathcal{H}_∞ norm, i.e. the impact of \mathcal{H}_∞ norm minimization on oscillation damping, is not trivially established. Equation (A.7) shows that damping of free oscillations in the system is only dependent on the location of system poles, and not on any system input. The \mathcal{H}_∞ norm, however, characterizes the system input-output behavior. In this Section, we show how these two characteristics of a linear system are still related.

In Subsection 3.2.1, Lemma 2, it is shown that $\bar{\sigma}(G(s))$ approaches $+\infty$ as s approaches any detectable system pole s_{pi} . Since $\bar{\sigma}(G(\mathbf{K}, s))$ is a continuous function of s [22], it follows that for arbitrary $M \in \mathbb{R}$, there exists a non-empty environment of every pole s_{pi} where $\bar{\sigma}(G(s))$ is greater than M , i.e.

$$\forall M \in \mathbb{R}, \exists \varphi \in \mathbb{R}, \text{ s.t. } |s - s_{pi}| \leq \varphi, \forall i \Rightarrow \bar{\sigma}(G(s)) \geq M. \quad (\text{A.11})$$

Additionally, if M_1 and M_2 in \mathbb{R} are chosen such that $M_1 > M_2$, it follows that there exist φ_1 and φ_2 , respectively, such that $\varphi_1 < \varphi_2$. Thus, if $\|G(s)\|_\infty \leq M_1$, it follows

that the nearest pole of the system is at least the distance φ_1 from the imaginary axis. Furthermore, if $\|G(s)\|_\infty$ is minimized to M_2 , e.g. by controller tuning, this distance is increased to φ_2 . Hence, minimization of $\|G(s)\|_\infty$ guarantees that all system poles have a minimal distance from the imaginary axis. This means that the resulting system eigenmodes of the poles that were pushed away are automatically better dampened and have a larger damping factor ξ . Thereby, the improvement of ξ is more successful if badly dampened oscillations have a relatively low frequency, as the damping ratio limit is closer to the imaginary axis in the low-frequency range. In power systems, frequency oscillations are in the range of 0.1 - 10 Hz, so \mathcal{H}_∞ optimization can be used effectively for power oscillation damping. If the system poles are far from the imaginary axis, \mathcal{H}_∞ optimization can worsen the oscillation damping in the system. This, however, was not observed for any considered power system, where large \mathcal{H}_∞ norms of the systems were obtained due to the proximity of poles to the imaginary axis.

B Modeling of coupled AC-DC power systems

The power system model introduced in Section 2.1 considers alternating current (AC) power systems with dynamic and static prosumers. This section extends the modeling to consider coupled AC-DC (alternating current-direct current) systems as well. A numerical example with an AC/DC system is considered in Section 4.2.

Figure B.1 shows the structure of a coupled AC-DC power system. The AC and DC grid are coupled via N_c converters, which convert AC power to DC power, and vice versa. In the following, we describe how coupled AC-DC systems are modeled in this work.

B.1 DC power grid model

The DC power flow equations, which describe the interconnection of converters, for the high-voltage direct current (HVDC) system are given with

$$P_{ci} = \sum_{j=1}^N c_{ij} V_{DCi} (V_{DCi} - V_{DCj}), \quad (\text{B.1})$$

where P_{ci} is the injected active power of the i -th converter into the DC grid, and c_{ij} are elements of the conductance matrix of the DC grid. Without loss of generality, we assume all buses without load or generation are eliminated from the system using Kron reduction [25].

B.2 AC-DC converter models

Since we are interested in system oscillations below 10 Hz, fast inner control loops of HVDC converters are not modeled and are represented by a first order delay system. The measurement time delays are modeled as first-order delays as well, and the phased locked loop (PLL) is approximated with a first-order system with one zero and one pole.

Two converter types are considered, whose structure is also described in [113]. The first type controls the DC voltage of the converter and is presented in Fig. B.2, where P_{cj} and P_{c0j} are the active power flow and the power flow reference for the DC converter, θ_{cj} is the voltage angle on the AC side, ω_{cm} is the estimated AC frequency, V_{DCj} and V_{DC0j} are the controlled DC voltage and DC voltage reference, and k_{cPj} is the converter active power droop gain. We consider the power system stabilizer (PSS)

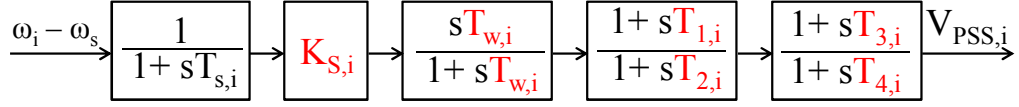


Figure B.3: Dynamic model of the simple power system stabilizer (taken from [51, 77]) used with HVDC converters, where $K_{S,i}$ is the PSS gain, $T_{w,i}$ is the washout time constant, $T_{1,i}-T_{4,i}$ are the lead-lag filters time constants, and $T_{s,i}$ is the sensor time constant. All of the PSS parameters are tunable, except the sensor time constant.

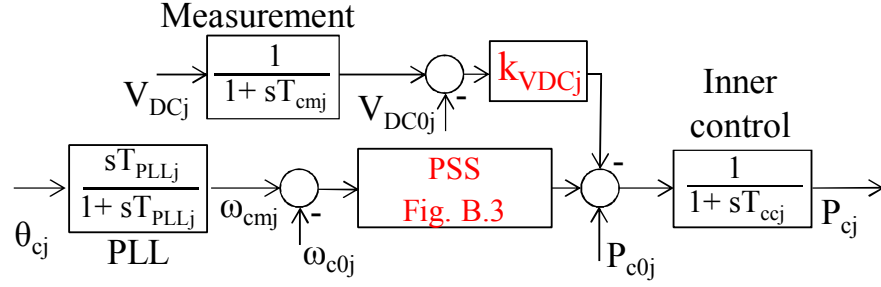


Figure B.4: The power control law of power-controlling converters. The PSS parameters and k_{VDC} are tuned.

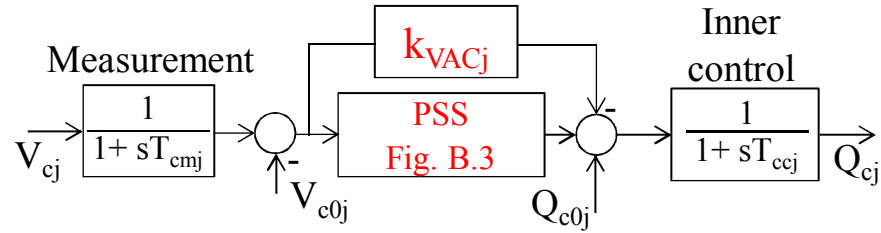


Figure B.5: Reactive power control for both converter types. The PSS parameters and k_{VAC} are tuned.

analysis. Thus, the AC and DC side of converters are coupled through the active power flow P , i.e. $P_{AC} = P_{DC} = P$. In total, each converter has 13 states.

B.3 Coupled AC-DC power system model

By coupling the AC prosumers and AC-DC converters with the AC and DC power grid equations, we obtain an analogous model to (2.4). This model can be then further linearized and the same optimization problem can be formulated as in described in Chapter 2.

C Power system models

This appendix presents the models of all power systems used for the numerical evaluations throughout this work.

C.1 IEEE 39 bus power system

Figures C.1, C.2, and C.9 show the power plant controller models used for modeling of the IEEE 39 bus grid. All models are a part of the system proposed in [77]. We optimize the gain $K_{A,i}$ of the AVR_{*i*}, shown red in Fig. C.1. We also optimize all parameters of PSS_{*i*}, except the physically-determined sensor time constant, marked red in Fig. C.2. The governor and turbine model, shown in Fig. C.9, has one optimization parameter, marked in red. It is the proportional gain of the governor. All presented controller models are standard IEEE models.

C.2 Extended IEEE 39 bus AC/DC power system

This section expands the model of the IEEE 39 bus system to also include a high voltage direct current (HVDC) power line, interfaced through converter stations with the AC system. This model is then used for the numerical evaluation in Section 4.2.

For this purpose, we modify the IEEE 39 bus system by adding a 400 km and 400 kV HVDC line between buses 16 and 27, as depicted in Fig. 4.5. Thereby, converter C_1

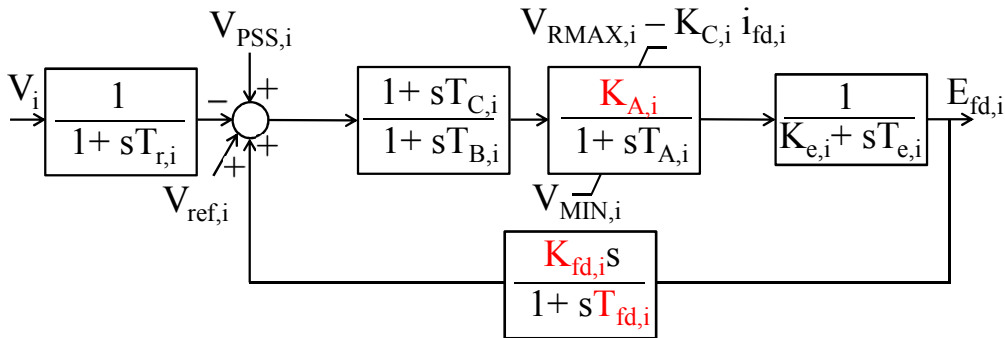


Figure C.1: Dynamic model of AVR_{*i*} [67], where $T_{r,i}$ is the transducer time constant, $T_{C,i}$ and $T_{B,i}$ are dynamic gain reduction time constants, $K_{A,i}$ is the AVR gain, $T_{A,i}$ is the AVR lag time constant, $K_{e,i}$ and $T_{e,i}$ are the exciter parameters, and $K_{fd,i}$ and $T_{fd,i}$ additional damping coefficients of the AVR. We assume that $K_{A,i}$, $K_{fd,i}$, and $T_{fd,i}$, marked red, are tunable.

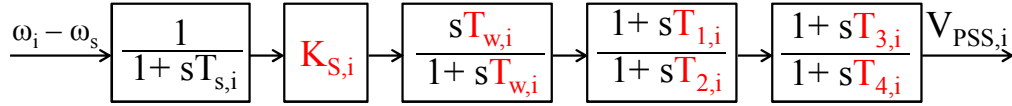


Figure C.2: Dynamic model of the simple power system stabilizer (taken from [51, 77]), where $K_{S,i}$ is the PSS gain, $T_{w,i}$ is the washout time constant, $T_{1,i}$ - $T_{4,i}$ are the lead-lag filters time constants, and $T_{s,i}$ is the sensor time constant. All of the PSS parameters are tunable, except the sensor time constant.

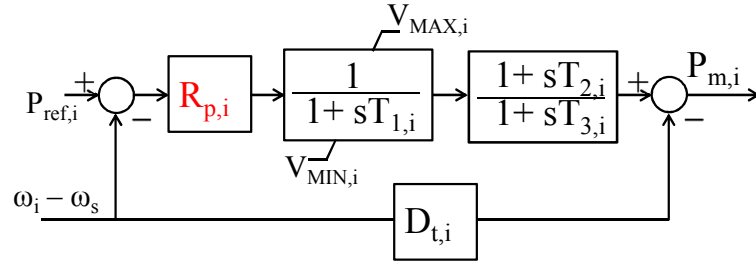


Figure C.3: The TGOV1 standard IEEE turbine and governor model. The frequency droop gain of the governor $R_{p,i}$ is an optimization variable.

controls its DC-voltage and is connected to bus 27, whereas converter C_2 is connected to bus 16 and controls its active power. The HVDC line resistance is set to $0.0114 \Omega/km$ [90], whereas all measurement time constants T_m and control time constants T_{con} of AC/DC converters are set to 10 ms. The PLL time constant is set to 100 ms to avoid sharp initial reactions of converters, which results from the approximation of the PLL and is not present in real systems. All PSS time constants of converters are the same as in the PSS of power plants, all PSS gains of converters are set to 10 p.u., k_P and k_{VAC} of C_1 are set to 0.04 p.u. and 10 p.u., respectively, and k_{VDC} and k_{VAC} of C_2 are set to 20 p.u. and 10 p.u., respectively.

This model is then used for the numerical evaluation in Section 4.2.

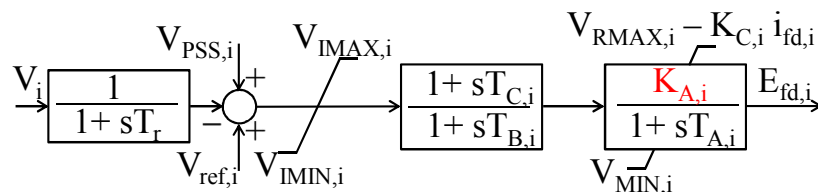


Figure C.4: The standard EXAC4 model of the AVR, where $T_{r,i}$ is the transducer time constant, $T_{C,i}$ and $T_{B,i}$ are dynamic gain reduction time constants, $K_{A,i}$ is the AVR gain, and $T_{A,i}$ is the AVR lag time constant. We assume that $K_{A,i}$, marked red, is tunable.

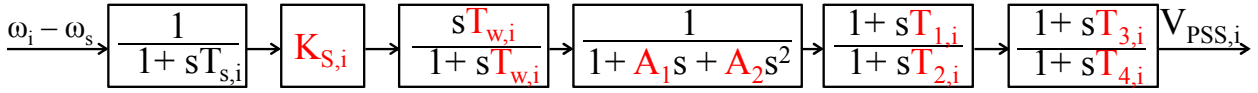


Figure C.5: The standard IEEE PSS 1A model, where $K_{S,i}$ is the PSS gain, $T_{w,i}$ is the washout time constant, $T_{1,i}$ - $T_{4,i}$ are the lead-lag filters time constants, $T_{s,i}$ is the sensor time constant, and A_1 and A_2 are notch filter parameters. All of the PSS parameters are tunable, except the sensor time constant.

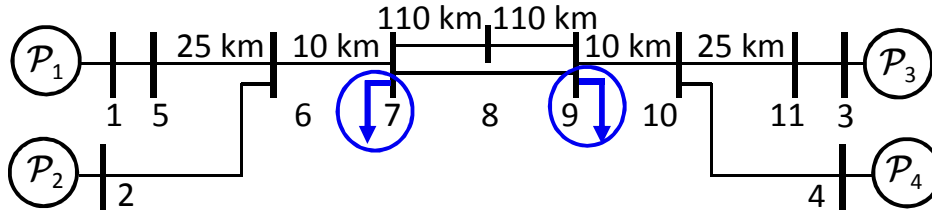


Figure C.6: A two-area system from [51, p. 813, Example 12.6].

C.3 Reduced European power system with 53 power plants

The reduced European grid, used in Subsection 4.3, uses controllers shown in Figs. C.3, C.4, and C.5. Similar to the IEEE 39 bus controller models, the gains of $TGOV_i$ and AVR_i are tuned, as well as all parameters of PSS_i . For this power system, the standard model $TGOV1$ is used for $TGOV_i$, the $EXAC4$ model is used for AVR_i , and the IEEE PSS 1A model is used for PSS_i . All presented controller models are standard IEEE models.

C.4 IEEE 68 bus power system

Parameters of synchronous generators and of the power grid are provided in [105], whereas Figures C.9, C.3, C.1, and C.2 show the power plant controller models used for modeling of the IEEE 68 bus grid. The governor and turbine models, shown in Figs. C.9 and C.3 have one optimization parameter each, marked in red. It is the proportional gain of the governor. Thereby, half of the power plants have the model in Fig. C.3, whereas other power plants have the model in Fig. C.9. We optimize the gain $K_{A,i}$ of the AVR_i , shown red in Fig. C.1. We also optimize all parameters of PSS_i marked red in Fig. C.2, except the physically-determined sensor time constant. All presented controller models are standard IEEE models.

C.5 Four power plant system from [51]

We consider the grid from [51, Example 12.6, page 813] presented in Fig. C.6. The parameters of the transmission grid, as well as the parameters of power plants, can be found in [51]. This power system, with different controllers, is used for two method

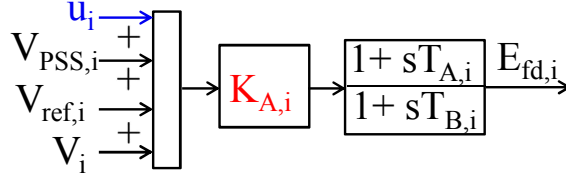


Figure C.7: Dynamic model of a simple AVR_{*i*} used, e.g. in [51]. It consists of a gain $K_{A,i}$ and a transient gain reduction component with the time constants $T_{A,i}$ and $T_{B,i}$. The gain $K_{A,i}$, marked red, is tunable. The input u_i is additionally introduced, marked blue, which is used as a control input for the methods presented in Section 6.1.

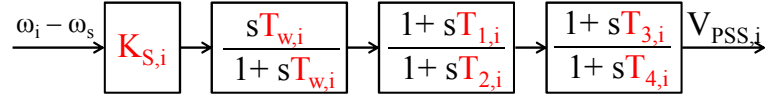


Figure C.8: Dynamic model of the simple power system stabilizer (taken from [51, 89]), where $K_{S,i}$ is the PSS gain, $T_{W,i}$ is the washout time constant, $T_{1,i}$ - $T_{4,i}$ are the lead-lag filters time constants. All of the PSS parameters are tunable.

comparisons in Chapter 6. For the first comparison in Section 6.1, all power plants have a TGOV model shown in Fig. C.3, an AVR model from Fig. C.7, and a PSS shown in Fig. C.8. The parameters of the TGOV model are $T_1 = 0.04s$, $T_2 = 1s$, $T_3 = 2s$, $k_P = 150$, and $D_t = 0$, while the voltage regulator time constants are set to $T_A = 1s$ and $T_B = 10s$, as in [51]. The initial value for the tunable voltage regulator gain is $K_A = 200$, and for all PSSs: $K_S = 50.5$, $T_1 = 0.0037s$, $T_2 = 0.0079s$, $T_3 = 40.9s$, $T_4 = 2.1386s$, and $T_W = 3.9604s$. However, the gain of the TGOV model is not an optimization variable in this case. The AVR model has a wide-area input u_i , used by the additional methods considered in Section 6.1. This input is calculated as an algebraic combination of states from all power plants. This system consists of 48 states and 28 tunable parameters.

For the second, numerical, comparison in Section 6.2, the same TGOV model is used as previously described, but for this comparison, the TGOV gain can be tuned. Additionally, the AVR model from Fig. C.1 is used. This system consists of 56 states and 32 tunable parameters.

As disturbance inputs for the optimization in both cases, we consider the loads in buses 7 and 9, marked blue in Fig. C.6.

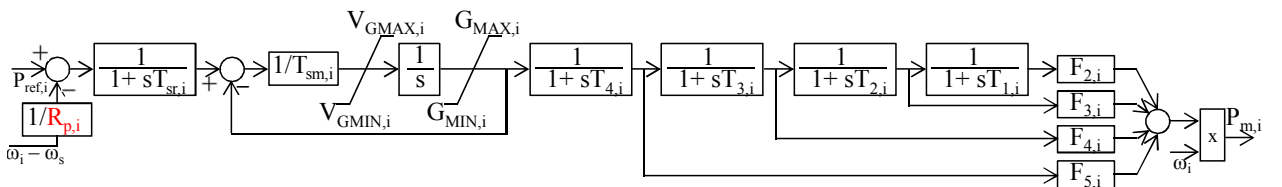


Figure C.9: Dynamic model of the turbine and governor from [69]. The frequency droop gain of the governor $R_{p,i}$ is an optimization variable.

Bibliography

- [1] IREN2 - future oriented electricity grids for integration of renewable energy systems, Jan 2020. <http://www.iren2.de/en/>.
- [2] King island renewable energy integration project, Jan 2020. <http://www.kingislandrenewableenergy.com.au/>.
- [3] Sinamics inverter, Jan 2020. <https://www.siemens.com/global/en/home/products/drives/sinamics.html>.
- [4] S. Al Ali, T. Haase, I. Nassar, and H. Weber. Impact of increasing wind power generation on the north-south inter-area oscillation mode in the European ENTSO-E system. *IFAC Proceedings Volumes*, 47(3):7653–7658, 2014.
- [5] P. Apkarian and D. Noll. Nonsmooth H-infinity synthesis. *IEEE Trans. Automatic Control*, 51(1):71 – 86, 2006.
- [6] P. Apkarian and D. Noll. Structured \mathcal{H}_∞ -control of infinite-dimensional systems. *International Journal of Robust and Nonlinear Control*, 28(9):3212–3238, 2018.
- [7] G. Befeckadu and I. Erlich. Robust decentralized structure-constrained controller design for power systems: an LMI approach. In *Power Systems Computation Conference*, 2005.
- [8] G. Befeckadu and I. Erlich. Robust decentralized controller design for power systems using matrix inequalities approaches. In *Power Eng. Soc. General Meet. IEEE*, 2006.
- [9] S. Bhela, D. Deka, H. Nagarajan, and V. Kekatos. Designing power grid topologies for minimizing network disturbances: An exact MILP formulation. In *Proc. IEEE American Control Conf*, 2019.
- [10] T. Borsche, T. Liu, and D. J. Hill. Effects of rotational inertia on power system damping and frequency transients. *54th Annual Conference on Decision and Control (CDC)*, pages 5940–5946, 2015.
- [11] S. Boyd. Alternating direction method of multipliers, Jan. 2020. https://web.stanford.edu/~boyd/papers/pdf/admm_slides.pdf.
- [12] S. Boyd and C. Barratt. Linear controller design: limits of performance. Technical report, Stanford University Stanford United States, 1991.
- [13] S. Boyd and C. Desoer. Subharmonic functions and performance bounds on linear time-invariant feedback systems. *IMA Journal of Mathematical control and Information*, 2(2):153–170, 1985.
- [14] S. Boyd, M. Hast, and K. Åström. MIMO PID tuning via iterated LMI restric-

- tion. *International Journal of Robust and Nonlinear Control*, 26(8):1718–1731, 2016.
- [15] S. Boyd and L. Vandenberghe. *Convex Optimization*. Cambridge University Press, New York, USA, 2004.
- [16] E. J. Candès, M. B. Wakin, and S. P. Boyd. Enhancing sparsity by reweighted ℓ_1 minimization. *J. Fourier Anal. Appl.*, 14:877–905, 2008.
- [17] N. Chaudhuri, A. Domahidi, R. Majumder, B. Chaudhuri, P. Korba, S. Ray, and K. Uhlen. Wide-area power oscillation damping control in nordic equivalent system. *IET generation, transmission & distribution*, 4(10):1139–1150, 2010.
- [18] S. Chen and O. Malik. Power system stabilizer design using μ synthesis. *IEEE Trans. Energy Conversion*, 10(1):175–181, 1995.
- [19] J. Chow, R. Galarza, P. Accari, and W. Price. Inertial and slow coherency aggregation algorithms for power system dynamic model reduction. *IEEE Trans. Power Systems*, 10(2):680–685, 1995.
- [20] C. Chung, K. Wang, C. Tse, and R. Niu. Power-system stabilizer (pss) design by probabilistic sensitivity indexes (psis). *IEEE Trans. Power Systems*, 17(3):688–693, 2002.
- [21] I. Chychykina, Z. A. Styczynski, C. O. Heyde, and R. Krebs. Power system instability prevention and remedial measures with online dynamic security assessment. In *PowerTech, Eindhoven*. IEEE, 2015.
- [22] B. De Moor and S. Boyd. Analytic properties of singular values and vectors. *KTH Leuven, Belgium Tech. Rep.*, 28:1989, 1989.
- [23] F. Deroo, M. Meinel, M. Ulbrich, and S. Hirche. Distributed control design with local model information and guaranteed stability. *IFAC Proceedings Volumes*, 47(3):4010–4017, 2014.
- [24] Q. Dinh, S. Gumussoy, W. Michiels, and M. Diehl. Combining convex–concave decompositions and linearization approaches for solving BMIs, with application to static output feedback. *IEEE Trans. Automatic Control*, 57(6):1377–1390, 2012.
- [25] F. Dörfler and F. Bullo. Kron reduction of graphs with applications to electrical networks. *IEEE Trans. Circuits and Systems I: Regular Papers*, 60(1):150 – 163, 2013.
- [26] J. C. Doyle, K. Glover, P. P. Khargonekar, and B. A. Francis. State-space solutions to standard \mathcal{H}_2 and \mathcal{H}_∞ control problems. *IEEE Trans. Automatic control*, 34(8):831–847, 1989.
- [27] DynaGridCenter. Dynagridcenter, Jan 2020. <http://forschung-stromnetze.info/projekte/dynamische-stromnetze-sicher-beherrschen/>.
- [28] EirGrid Group. EirGrid Group achieves record level of variable renewable en-

- ergy on irish electricity system, Jan 2020. <http://www.eirgridgroup.com/newsroom/record-renewable-energy-o/>.
- [29] L. El Ghaoui, F. Oustry, and M. AitRami. A cone complementarity linearization algorithm for static output-feedback and related problems. *IEEE Trans. Automatic control*, 42(8):1171–1176, 1997.
- [30] M. Fazel, H. Hindi, and S. P. Boyd. Log-det heuristic for matrix rank minimization with applications to hankel and euclidean distance matrices. In *American Control Conference (ACC)*, volume 3, pages 2156–2162, 2003.
- [31] A. Fuchs, M. Imhof, T. Demiray, and M. Morari. Stabilization of large power systems using VSC-HVDC and model predictive control. *IEEE Trans. Power Delivery*, 29(1):480 – 488, 2014.
- [32] P. Gahinet and P. Apkarian. A linear matrix inequality approach to \mathcal{H}_∞ control. *International journal of robust and nonlinear control*, 4(4):421–448, 1994.
- [33] A. Germond and R. Podmore. Dynamic aggregation of generating unit models. Technical Report 4, 1978.
- [34] R. Godoy, J. Pinto, C. A. Canesin, E. Coelho, and A. Pinto. Differential-evolution-based optimization of the dynamic response for parallel operation of inverters with no controller interconnection. *IEEE Trans. industrial electronics*, 59(7):2859–2866, 2012.
- [35] A. Gomez-Exposito and A. Abur. *Power system state estimation: theory and implementation*. CRC press, 2004.
- [36] E. Grebe, J. Kabouris, S. L. Barba, W. Sattinger, and W. Winter. Low frequency oscillations in the interconnected system of continental Europe. In *IEEE PES General Meeting*, 2010.
- [37] S. Gumussoy, D. Henrion, M. Millstone, and M. L. Overton. Multiobjective robust control with HIFOO 2.0. *Proc. 6th IFAC Symposium on Robust Control Design*, 42(6):144–149, 2009.
- [38] J. Han and R. Skelton. An LMI optimization approach for structured linear controllers. *42nd IEEE International Conference on Decision and Control*, (5):5143 – 5148, 2004.
- [39] O. Hanson, C. Goodwin, and P. Dandeno. Influence of excitation and speed control parameters in stabilizing intersystem oscillations. *IEEE Trans. Power Apparatus and Systems*, 1968.
- [40] A. Hassibi, J. How, and S. Boyd. A path-following method for solving BMI problems in control. In *American Control Conference (ACC)*, volume 2, pages 1385–1389. IEEE, 1999.
- [41] N. Hatziargyriou. *Microgrids: architectures and control*. John Wiley & Sons, 2014.
- [42] Hawaiian Electric. About our fuel mix, Jan 2020. <https://>

www.hawaiianelectric.com/clean-energy-hawaii/our-clean-energy-portfolio/renewable-energy-sources.

- [43] S. Ibaraki and M. Tomizuka. Rank minimization approach for solving BMI problems with random search. In *American Control Conference (ACC)*, volume 3, pages 1870–1875. IEEE, 2001.
- [44] IEEE. IEEE recommended practice for excitation system models for power system stability studies. *IEEE Std 421.5-2005 (Revision of IEEE Std 421.5-1992)*, pages 1–93, April 2006.
- [45] A. Jain, A. Chakraborty, and E. Biyik. Distributed wide-area control of power system oscillations under communication and actuation constraints. *Control Engineering Practice*, 74:132–143, 2018.
- [46] C. Kammer and A. Karimi. Decentralized and distributed transient control for microgrids. *IEEE Trans. Cont. Syst. Tech.*, (99):1–12, 2017.
- [47] I. Kamwa, R. Grondin, and L. Loud. Time-varying contingency screening for dynamic security assessment using intelligent-systems techniques. *IEEE Trans. Power Systems*, 16(3):526–536, 2001.
- [48] S. Kanev, C. Scherer, M. Verhaegen, and B. De Schutter. Robust output-feedback controller design via local BMI optimization. *Automatica*, 40(7):1115–1127, 2004.
- [49] A. Karimi, H. Khatibi, and R. Longchamp. Robust control of polytopic systems by convex optimization. *Automatica*, 43(8):1395–1402, 2007.
- [50] U. Kerin, C. Heyde, R. Krebs, and E. Lerch. Real-time dynamic security assessment of power grids. *The European Physical Journal Special Topics*, 223(12):2503–2516, 2014.
- [51] P. Kundur. *Power System Stability and Control*. McGraw-Hill, 1993.
- [52] P. Kundur, G. Berube, L. Hajagos, and R. Beaulieu. Practical utility experience with and effective use of power system stabilizers. In *Power Engineering Society General Meeting, IEEE*, volume 3, pages 1777–1785. IEEE, 2003.
- [53] K. Küßner, Z. Kasztel, I. Erlich, H.-H. Wilfert, and P. Schegner. Damping control of inter-area oscillations in the European power system using aggregated models. *Electrical Engineering*, 83(5-6):275–285, 2001.
- [54] X. Lei, E. Lerch, and D. Povh. Optimization and coordination of damping controls for improving system dynamic performance. *IEEE Trans. Power Systems*, 16(3):473–480, 2001.
- [55] X. Lei, D. Povh, and O. Ruhle. Industrial approaches for dynamic equivalents of large power systems. In *IEEE Power Engineering Society Winter Meeting*, volume 2, pages 1036–1042. IEEE, 2002.
- [56] F. Leibfritz. An LMI-based algorithm for designing suboptimal static $\mathcal{H}_2/\mathcal{H}_\infty$ output feedback controllers. *SIAM journal on Control and Optimization*,

- 39(6):1711–1735, 2001.
- [57] P. Li. Power system reduction techniques for dynamic analysis, ETH Zurich. Master’s thesis, 2016.
- [58] K. Liao, Z. He, Y. Xu, G. Chen, Z. Dong, and K. Wong. A sliding mode based damping control of DFIG for interarea power oscillations. *IEEE Trans. Sustainable Energy*, 8(1):258 – 267, 2017.
- [59] F. Lin, M. Fardad, and M. R. Jovanović. Design of optimal sparse feedback gains via the alternating direction method of multipliers. *IEEE Trans. Automat. Control*, 58(9):2426–2431, 2013.
- [60] Y. Liu, Q. H. Wu, and X. X. Zhou. Coordinated switching controllers for transient stability of multi-machine power systems. *IEEE Trans. Power Systems*, 31(5):3937 – 3949, 2016.
- [61] J. Lofberg. YALMIP : a toolbox for modeling and optimization in MATLAB. *IEEE Int. Conf. on Robotics and Automation*, pages 284 – 289, 2004.
- [62] W. Lu and B. T. Ooi. Simultaneous inter-area decoupling and local area damping by voltage source HVDC. In *Power Engineering Society Winter Meeting, 2001. IEEE*, volume 3, pages 1079–1084. IEEE, 2001.
- [63] J. Lunze. *Regelungstechnik 2: Mehrgrößensysteme Digitale Regelung*. Springer-Verlag, 2013.
- [64] M. Mahmoudi, J. Dong, K. Tomsovic, and S. Djouadi. Application of distributed control to mitigate disturbance propagations in large power networks. In *North American Power Symposium (NAPS)*. IEEE, 2015.
- [65] B. Marinescu. Residue phase optimization for power oscillations damping control revisited. *Electric Power Systems Research*, 168:200–209, 2019.
- [66] B. Marinescu, B. Mallem, H. Bourles, and L. Rouco. Robust coordinated tuning of parameters of standard power system stabilizers for local and global grid objectives. In *PowerTech, Bucharest*. IEEE, 2009.
- [67] MathWorks. Excitation system, Jan 2020. <https://de.mathworks.com/help/physmod/sps/powersys/ref/excitationsystem.html>.
- [68] Mathworks. Simscape power systems, Jan 2020. <https://www.mathworks.com/products/simpower.html>.
- [69] MathWorks. Steam turbine and governor, Jan 2020. <https://www.mathworks.com/help/physmod/sps/powersys/ref/steamturbineandgovernor.html>.
- [70] Mathworks. systune, Jan 2020. <https://www.mathworks.com/help/control/ref/systune.html>.
- [71] A. Mešanović, U. Münz, J. Bamberger, and R. Findeisen. Controller tuning for the improvement of dynamic security in power systems. In *IEEE PES Innovative*

- Smart Grid Technologies Conf. Europe*. IEEE, 2018.
- [72] A. Mešanović, U. Münz, and R. Findeisen. Coordinated tuning of synchronous generator controllers for power oscillation damping. In *Innovative Smart Grid Technologies Conference Europe*. IEEE, 2017.
- [73] A. Mešanović, U. Münz, and R. Findeisen. Scalable and data privacy conserving controller tuning for large-scale power networks. *submitted, arXiv preprint arXiv:1911.01499*, 2019.
- [74] A. Mešanović, U. Münz, A. Szabo, M. Mangold, J. Bamberger, M. Metzger, C. Heyde, R. Krebs, and R. Findeisen. Guaranteed \mathcal{H}_∞ controller parameter tuning for power systems: Method and experimental evaluation. *submitted*, 2019.
- [75] A. Mešanović, D. Unseld, U. Münz, C. Ebenbauer, and R. Findeisen. Parameter tuning and optimal design of decentralized structured controllers for power oscillation damping in electrical networks. In *Proc. Amer. Cont. Conf. (ACC)*, pages 3828–3833. IEEE, 2018.
- [76] J. V. Milanović. Probabilistic stability analysis: the way forward for stability analysis of sustainable power systems. *Phil. Trans. R. Soc. A*, 375(2100):20160296, 2017.
- [77] A. Moeini, I. Kamwa, P. Brunelle, and G. Sybille. Open data IEEE test systems implemented in simpowersystems for education and research in power grid dynamics and control. In *Power Engineering Conference (UPEC), 2015 50th International Universities*, pages 1–6. IEEE, 2015.
- [78] J. Nocedal and S. Wright. *Numerical optimization*. Springer, 2006.
- [79] Z. A. Obaid, L. Cipcigan, and M. T. Muhssin. Power system oscillations and control: Classifications and PSSs’ design methods: A review. *Renewable and Sustainable Energy Reviews*, 79:839–849, 2017.
- [80] B. Pal and B. Chaudhuri. *Robust control in power systems*. Springer Science & Business Media, 2006.
- [81] Y. Pipelzadeh, B. Chaudhuri, and T. Green. Control coordination within a VSC HVDC link for power oscillation damping: A robust decentralized approach using homotopy. *IEEE Trans. Control Systems Technology*, (21):1270–1279, 2013.
- [82] Y. Pipelzadeh, N. Chaudhuri, B. Chaudhuri, and T. Green. Coordinated control of offshore wind farm and onshore HVDC converter for effective power oscillation damping. *IEEE Trans. Power Systems*, 32(3):1860–1872, 2017.
- [83] B. Poolla, D. Gross, and F. Dörfler. Placement and implementation of grid-forming and grid-following virtual inertia and fast frequency response. *IEEE Trans. Pow. Sys.*, 2019.
- [84] V. Pradhan, A. M. Kulkarni, and S. A. Khaparde. A composite strategy for power oscillation damping control using local and wide area feedback signals. *IEEE Trans. Power Systems*, 31(3):2348–2360, 2016.

-
- [85] R. Preece and J. Milanovic. Tuning of a damping controller for multiterminal VSC-HVDC grids using the probabilistic collocation method. *IEEE Trans. Power Delivery*, 29(1):318–326, 2014.
- [86] R. Preece, J. Milanovic, A. M. Almutairi, and O. Marjanovic. Damping of inter-area oscillations in mixed AC/DC networks using WAMS based supplementary controller. *IEEE Trans. Power Systems*, 28(2):1160–1169, 2013.
- [87] S. Püschel-Løvgreen and P. Mancarella. Frequency response constrained economic dispatch with consideration of generation contingency size. In *Power Systems Computation Conference (PSCC)*. IEEE, 2018.
- [88] A. Rahmoun, A. Armstorfer, H. Biechi, and A. Rosin. Mathematical modeling of a battery energy storage system in grid forming mode. In *Power and Electrical Engineering of Riga Technical University (RTUCON), 58th Intl. Sci. Conf. on*, pages 1–6. IEEE, 2017.
- [89] M. Raoufat, K. Tomsovic, and S. Djouadi. Virtual actuators for wide-area damping control of power systems. *IEEE Trans. Power Systems*, 31(6):4703–4711, 2016.
- [90] Cigre Working Group B4-57 and B4-58. CIGRE B4 DC grid test system, 2013.
- [91] REN21. Renewables 2018 global status report, Jan 2020. <http://www.ren21.net/gsr-2018/>.
- [92] G. Rogers. *Power system oscillations*. Springer Science & Business Media, 2012.
- [93] L. Rouco. Coordinated design of multiple controllers for damping power system oscillations. *International Journal of Electrical Power & Energy Systems*, 23(7):517–530, 2001.
- [94] M. S. Sadabadi and D. Peaucelle. From static output feedback to structured robust static output feedback: A survey. *Annual reviews in control*, 42:11–26, 2016.
- [95] J. Sanchez-Gasca and J. Chow. Power system reduction to simplify the design of damping controllers for interarea oscillations. *IEEE Trans. Power Systems*, 11(3):1342–1349, 1996.
- [96] C. Scherer and S. Weiland. Linear matrix inequalities in control, lecture notes, Jan 2019.
- [97] C. W. Scherer. Structured \mathcal{H}_∞ optimal control for nested interconnections: A state-space solution. *Systems & Control Letters*, pages 1105–1113, 2013.
- [98] J. Schiffer, D. Zonetti, R. Ortega, A. M. Stanković, T. Sezi, and J. Raisch. A survey on modeling of microgrids-from fundamental physics to phasors and voltage sources. *Automatica*, 74:135–150, 2016.
- [99] S. Schuler, M. Gruhler, U. Münz, and F. Allgöwer. Design of structured static output feedback controllers. *IFAC Proceedings Volumes*, 44(1):271–276, 2011.

- [100] S. Schuler, U. Münz, and F. Allgöwer. Decentralized state feedback control for interconnected systems with application to power systems. *Journal of Process Control*, 24(2):379–388, 2014.
- [101] S. Shin, P. Hart, T. Jahns, and V. M. Zavala. A hierarchical optimization architecture for large-scale power networks. *IEEE Transactions on Control of Network Systems*, 2019.
- [102] Siemens. Siemens provides sustainable energy for galapagos island, Jan 2020. <https://new.siemens.com/global/en/products/energy/references/galapagos.html>.
- [103] Siemens. Siemens TNA, Jan 2020. <https://new.siemens.com/global/en/products/energy/energy-automation-and-smart-grid/grid-control/transmission-management.html>.
- [104] Siemens PTI. Small signal stability analysis module, Jan 2020. https://w3.usa.siemens.com/smartgrid/us/en/transmission-grid/products/grid-analysis-tools/transmission-system-planning/Documents/PSSE_Small_Signal_Stability_Analysis_SI.pdf.
- [105] A. Singh and B. Pal. IEEE PES task force on benchmark systems for stability controls report on the 68-bus 16-machine 5-area system. *IEEE Power Energy Soc.*, 2013.
- [106] SMA. Hybrid power plant on st. eustasius island, Jan 2020. <https://www.sma.de/en/newsroom/current-news/news-details/news/2876-system-solution-from-sma-provides-caribbean-island-with-100-solar-power-supply.html>.
- [107] T. Smed and G. Andersson. Utilizing HVDC to damp power oscillations. *IEEE Trans. Power Delivery*, 8(2):620 – 627, 1993.
- [108] L. Sturk, C. and Vanfretti, Y. Chompoobutrgool, and H. Sandberg. Coherency-independent structured model reduction of power systems. *IEEE Trans. Power Systems*, 29(5):2418–2426, 2014.
- [109] J. F. Sturm. Using SeDuMi 1.05, a Matlab toolbox for optimization over symmetric cones, Jan 2020.
- [110] J. Taranto, A. do Bomfim, D. Falcao, and N. Martins. Automated design of multiple damping controllers using genetic algorithms. *Proc. IEEE Power Engineering Society. Winter Meeting*, pages 539 – 544, 1999.
- [111] D. Uherka and A. Sergott. On the continuous dependence of the roots of a polynomial on its coefficients. *The American mathematical monthly*, 84(5):368–370, 1977.
- [112] A. Ulbig, T. S. Borsche, and G. Andersson. Impact of low rotational inertia on power system stability and operation. *IFAC World Congress*, 19(1):7290 – 7297, 2014.

-
- [113] A. M. Vural. Contribution of high voltage direct current transmission systems to inter-area oscillation damping: A review. *Renewable and Sustainable Energy Reviews*, 57:892–915, 2016.
- [114] X. Wu and M. Jovanović. Sparsity-promoting optimal control of systems with symmetries, consensus and synchronization networks. *Systems & Control Letters*, 103, 2017.
- [115] X. Wu, F. Dörfler, and M. R. Jovanović. Input-output analysis and decentralized optimal control of inter-area oscillations in power systems. *IEEE Trans. Pow. Sys.*, 31(3):2434–2444, 2016.
- [116] A. Yaghooti, M. Buygi, and M. Shانهchi. Designing coordinated power system stabilizers: A reference model based controller design. *IEEE Trans. Power Systems*, 31(4):2914 – 2924, 2016.
- [117] K. Yu, Q. Ai, S. Wang, J. Ni, and T. Lv. Analysis and optimization of droop controller for microgrid system based on small-signal dynamic model. *IEEE Trans. Smart Grid*, 7(2):695–705, 2016.
- [118] R. Zárate-Miñano, T. Van Cutsem, F. Milano, and A. J. Conejo. Securing transient stability using time-domain simulations within an optimal power flow. *IEEE Trans. Power Systems*, 25(1):243–253, 2010.
- [119] K. Zhou and J. Doyle. *Essentials of robust control*. Prentice hall Upper Saddle River, NJ, 1998.
- [120] C. Zhu, M. Khammash, V. Vittal, and W. Qiu. Robust power system stabilizer design using \mathcal{H}_∞ loop shaping approach. *IEEE Trans. Power Systems*, 18(2):810 – 818, 2003.

